UNIVERSITÉ BLAISE PASCAL **Année 2012**

N° D.U. 2220

ECOLE DOCTORALE

Sciences de la Vie, Santé, Agronomie, Environnement

N° 573

THÈSE de DOCTORAT

en

« Nutrition et Science des Aliments, Biophysique & Imagerie par Résonance Magnétique Nucléaire »

par

Mustapha BOUHRARA

Caractérisation locale des déformations et des transferts de matière dans le muscle sous contraintes thermiques par imagerie RMN

Thèse dirigée par : Dr. Jean-Marie BONNY et Dr. Sylvie CLERJON

Soutenue le 25 janvier 2012 devant la commission d'examen composée de :

Pr. Serge AKOKA	CNRS-Université, Nantes	Examinateur
Dr. Jean-Marie BONNY	INRA, Clermont-Ferrand	Directeur de thèse
Dr. Sylvie CLERJON	INRA, Clermont-Ferrand	Directeur de thèse
Pr. Philippe MICHAUD	Polytech, Clermont-Ferrand	Examinateur
Dr. Dimitrios SAKELLARIOU	CEA, Saclay	Rapporteur
Pr. Gilles TRYSTRAM	AgroParisTech, Paris	Rapporteur

« Les savants des temps passés et des nations révolues n'ont cessé de composer des livres. Ils l'ont fait pour léguer leur savoir à ceux qui les suivent. Ainsi demeurera vive la quête de la vérité. »

Al-Khwarizmi

Remerciements

Ce moment d'écriture des remerciements est pour moi le plus émouvant mais aussi le plus angoissant. Emouvant car cela signifie que la fin de cette thèse est arrivée, et angoissant par crainte de ne pas remercier comme il se doit chaque personne qui d'une part a pu contribuer à la réalisation de ce travail, et d'autre part a supporté mes humeurs parfois exaspérantes.

Au terme de ce doctorat qui a été réalisé au sein de l'UR 370 à l'INRA de Theix dans l'équipe Structures Tissulaires et Interactions Moléculaires (STIM), je tiens à exprimer ma gratitude au Dr. Jean-Pierre RENOU qui m'a proposé d'intégrer son unité afin de réaliser ce travail de thèse.

Mais avant tout, je tiens à exprimer vivement toute ma reconnaissance et toute ma gratitude à mes deux codirecteurs de thèse Dr. Jean-Marie BONNY et Dr. Sylvie CLERJON mais aussi à mon co-encadrant Dr. Jean-Louis DAMEZ pour leur encadrement précieux et leur orientation permanente. J'ai eu la grande chance de travailler avec vous, et c'est à vous que je dois ce progrès à la fois scientifique et humain et quoi que je puisse dire, je ne pourrai jamais vous remercier à la hauteur de votre générosité, de votre compréhension et de votre implication dans ce projet. Je vous aime et je vous serai toujours reconnaissant.

Il est certain que la réussite de ce projet est due en partie aux directives et aux conseils des membres de mon comité de thèse à savoir Dr. Guy DELLAVALLE, Dr. Ralph SINKUS et Dr. Alain KONDJOYAN auxquels je dois des vifs remerciements.

Je remercie les rapporteurs de cette thèse Dr. Dimitrios SAKELLARIOU et Pr. Gilles TRYSTRAM pour la rapidité avec laquelle ils ont lu mon manuscrit et l'intérêt qu'ils ont porté à mon travail. Merci également aux autres membres du jury qui ont accepté de juger ce travail : Pr. Serge AKOKA et Pr. Philippe MICHAUD.

Une partie importante du travail présenté dans ce manuscrit et dans certains de mes articles scientifiques est le fruit d'une large collaboration avec les membres de l'équipe C2T, notamment Mr. Stéphane PORTANGUEN pour la partie dédiée à la conception instrumentale de notre dispositif de chauffage, Mr. Cyril CHEVARIN et Dr. Alain KONDJOYAN pour la partie modélisation de la température mais aussi pour l'interprétation des phénomènes biologiques observés. Ceci est la preuve que le travail en collaboration ne peut qu'être bénéfique et un plus, dans mon cas fondamental, et c'est pour cette raison que je leur exprime mes sincères remerciements.

Je remercie également Dr. Benoist LEHALLIER mon ami et camarade, et avec qui j'ai partagé notre bureau, de m'avoir supporté durant ces longues trois années de thèse mais

surtout pour sa contribution dans la partie concernant le recalage d'image RMN pour l'établissement des champs de déformation. Pareillement, je tiens à remercier Mr. Abdellatif BENMOUSSA pour son aide précieuse sur le plan technique tout au long de mes expérimentations et pour les nombreuses discussions constructives que nous avons pu mener. Enfin, un grand merci aux membres de la plateforme RMSB et de l'unité QuaPA pour leur disponibilité et leur encouragement.

Au-delà du plan scientifique, la réussite d'une thèse est due aussi aux démarches administratives et logistiques, c'est pour cette raison que je me dois de remercier tout les membres du staff administratif de mon unité d'accueil, je pense notamment à Rachel TARDY, Eliane BACHELARD et Françoise LASSALAS.

Que chaque personne ayant contribué de près ou de loin à ce travail trouve ici mes vifs remerciements et ma sincère gratitude.

Avant de finir, je remercie ma mère Khadija, mon père Larbi, mon frère Mohamed, ma sœur Fatima et ma future femme Nesma d'être là pour moi à chaque instant de mon existence. Je pense qu'aucune langue ne dispose de mots ou d'expressions bien établis pour leur rendre hommage et les remercier de faire de moi ce que je suis. Je vous adore et j'espère être à la hauteur de vos attentes.

I. Résumé

La cuisson est un procédé universel de transformation de la matière première carnée en aliment. Le chauffage de la matrice musculaire conditionne diverses qualités organoleptiques, technologiques, sanitaires et nutritionnelles des viandes cuites. La cuisson étant appliquée de plus en plus fréquemment en conditions industrielles standardisées, il est pertinent de modéliser certains mécanismes clés dans le déterminisme de ces qualités afin d'optimiser le procédé.

Pour cela, une démarche expérimentale originale a été mise en place fondée sur une analyse quantitative, locale, dynamique et *in situ* de la viande pendant la cuisson. Cette démarche ne fait pas d'hypothèse réductionniste en étudiant un échantillon intact à l'échelle de l'aliment consommé, ni d'hypothèse simplificatrice en prenant en compte les variations spatiales de la température dans l'échantillon. Elle s'appuie sur des développements originaux en imagerie par résonance magnétique nucléaire à haut champ et en traitement d'images pour cartographier la déformation et la quantité d'eau. Des modèles robustes liant température, déformation et quantité d'eau ont été obtenus pour des muscles de teneur variable en tissu conjonctif. Les résultats montrent principalement une augmentation de la déformation avec la température en plusieurs phases dont les caractéristiques dépendent de la composition du muscle, et une diminution de la quantité d'eau avec la température. Tous ces résultats sont discutés et interprétés au regard du comportement à la température des différents composants du muscle.

Ce travail montre d'abord que l'imagerie dynamique, quantitative et multiparamétrique permet de décrypter des mécanismes intervenant lors de la cuisson des viandes sans établir des hypothèses réductrices lors de l'interprétation de ces phénomènes. Elle a conduit de plus, à des développements méthodologiques applicables à d'autres champs et ouvre la voie à d'autres investigations dans le domaine de l'optimisation qualitative des produits carnés transformés.

Mots-clés : Viande, Cuisson, Imagerie RMN, *in situ*, modélisation

Abstract

Cooking is a general process which transforms the meat raw material into food. The heating of muscle matrix influences different organoleptic, industrial, health and nutritional qualities of cooked meat. Cooking being applied more and more frequently in standardized and industrial conditions, it makes sense to model some key mechanisms which determine the latter qualities in order to optimize the process.

For this purpose, an original experimental approach has been developed based on a quantitative, local, dynamic and *in situ* analysis of the meat during cooking. This approach is not based on any reductionist hypothesis by studying an intact sample at the scale of the consumed food, nor by the simplifying assumption of taking into account the spatial variations of temperature in the sample. It is based on original developments in nuclear magnetic resonance imaging at high-field and on image processing in order to map deformation and the water content. Robust models linking temperature, deformation and water content were obtained for muscles differing from their content in connective tissue. The results mainly show a deformation increase with the temperature in several phases whose characteristics depend on the muscle composition, and a decrease in the water content with temperature. All these results are discussed and interpreted thanks to the temperature behavior of the various muscle components.

This work first shows that quantitative, multi-parametric and dynamic imaging can decipher the mechanisms involved during meat cooking, without formulating simplifying assumptions in the interpretation of these phenomena. Furthermore, it has led to methodological developments applicable to other fields and paves the way for further investigations in the field of quality optimization of processed meat products.

Keywords: Meat, Heating process, NMR imaging, *in situ*, modeling

II. Table des matières

III. Liste des figures, tables, abréviations et publications

1. Figures

1.1 Revue de littérature

1.2 Travail personnel

agreement between simulated and experimentally measured temperatures, near the surface and close to the centre of the sample.

Figure 1.5: Representative experimental and simulated time course of the temperature difference between thermocouples Th_1 and Th_3 shown in Figure 1.2, placed 14.2 mm apart at the start of the experiment.

Figure 1.6: Temperatures mapped from our simulation, in the central section of the sample, for 4 average temperatures (35 °C, 50 °C, 60 °C and 70 °C) and the corresponding NMR images. Transfer coefficients are here considered as the same in meat and juice.

Figure 1.7: NMR images of the deformation in the central section of the sample. The grey scale windowing has been adjusted to compensate for degraded SNR. The values displayed are means of simulated temperatures in this central section.

Figure 1.8: Curves showing the time course of the surface area of the central section of a representative muscle, the set temperature (heating water) and the simulated average temperature of the muscle.

Figure 2.1: (A) Orientation and size of the profile for the sample tank. (B) Effect of BG duration on the cancellation of the heating water signal assessed by measuring the profile of the signal from the whole tank. The duration of the BG varies only in the specified direction, BG being applied in the other two directions for 7 ms at 45 $mT.m^{-1}$. The windowing of color levels was adjusted at each temperature to compensate for the continuous SNR loss.

Figure 2.2: MR images obtained at 20 °C and 75 °C showing internal fiduciary markers and the positions of the pairs of landmarks (red points). Landmarks (number of Landmarks = 23, 21 and 26 respectively for sections 1, 3 and 6) were positioned manually on the images and used to optimize the 2D non-linear deformation model.

Figure 2.3: Time courses of T_1 and T_2 relaxation times and of PD with muscle temperature.

Figure 2.4: Distribution of the magnitude of the circulating water velocity in the tank at 20 °C and 75 °C. Circles define the regions of near stagnation of the heating water.

Figure 2.5: For eight average temperatures in the sample, (A) Temperature maps obtained by numerical simulation and (B) the corresponding NMR T_2^*-weighted images. The windowing

Figure 4.4: (Left) B_1^+ maps derived from the same acquisitions of a homogeneous phantom with $K = C_1 = C_2 = 2$ using (A) DAM-SP and (B) DAM. (C) Gold standard B_1^+ map. (Right) Respective Bland and Altman plots.

Figure 4.5: (A) Factor of merit Γ as a function of γB_1^+ for three values of K (B) Maps of noise propagated onto B_1^+ maps for the same values of K.

Figure 4.6: (Left) B_1^+ maps obtained by DAM-SP with different strategies for reducing OBM-dependent inaccuracies (A) $K = 3$, $C_1 = 3, C_2 = 1.5$ (B) SLR pair with rejection ripple = 0.01% (C) Gaussian pair. (Right) Respective Bland and Altman plots.

Figure 5.1: schematic representation of deformation and water content mapping during heating by dynamic MRI.

Figure 5.2: Sample with high IMCT content (slice 3/5). (A) T_2^*-weighted MR images (DIs). The windowing of gray levels was adjusted for each image to compensate for continuous SNR loss. (B) Corresponding temperature maps obtained by numerical simulation for four average temperatures in the sample. (C) Corresponding representations of deformation as a function of direction and magnitude calculated by nonlinear optimal registration from two consecutive DI_s. (D) Corresponding representations of the magnitude of deformation calculated by nonlinear optimal registration from two consecutive DI_s. (E) Corresponding B_1 maps. (F) Corresponding proton density maps.

Figure 5.3: Sample with low IMCT content (slice 3/5). (A) T_2^*-weighted MR images (DIs). The windowing of gray levels was adjusted for each image to compensate for continuous SNR loss. (B) Corresponding temperature maps obtained by numerical simulation for four average temperatures in the sample. (C) Corresponding representations of deformation as a function of direction and magnitude calculated by nonlinear optimal registration from two consecutive DI_s. (D) Corresponding representations of the magnitude of deformation calculated by nonlinear optimal registration from two consecutive DI_s. (E) Corresponding B_1 maps. (F) Corresponding proton density maps.

Figure 5.4: cumulative deformation (mm) versus temperature (°C) for high (A) and low (B) IMCT content samples. Error bars represent the standard deviation. The red star marks the inflexion point.

Figure 5.5: proton density versus average temperature (°C) for high (A) and low (B) IMCT content samples. Error bars represent the standard deviation.

Figure 5.6: Proton density versus cumulative deformation (mm) for high (A) and low (B) IMCT content samples. These results are obtained on several ROIs taking on 5 slices of each sample on the last two acquisitions at high temperature.

Figure 5.7: Proton density versus cumulative deformation (mm) for merged data. These results are obtained on several ROIs taking on 5 slices of each sample on the last two acquisitions at high temperature.

2. Tables

2.1 Revue de littérature

Tableau 1: Revue de littérature sur les effets des traitements thermiques sur la variation de la structure de la viande et sa relation avec les pertes à la cuisson. Conclusions de la littérature sur les effets de la maturation et de la pré-congélation de la viande sur les pertes à la cuisson. (D'après (Oillic 2011)).

2.2 Travail personnel

Table 2.1: Parameters quantifying the registration error averaged over all pairs of landmarks. Results are represented for four non-linear models with increasing degrees of freedom and for three different slices.

3. Abréviations

2D	bidimensionnel
B_1	champ radio fréquence
°C	degré Celsius
DAM	double angle method
DAM-SP	double angle method with selective pulses
FID	Free-induction decay

GE	gradient-echo
GESFID	gradient-echo sampling of FID
GESFIDE	gradient-echo sampling of FID and echo
INRA	institut national de la recherche agronomique
IRM	imagerie par résonance magnétique
min	minute
RF	radio fréquence
RMN	resonance magnétique nucléaire
T	tesla
T_1	temps de relaxation longitudinale
T_2	temps de relaxation transversale
s	seconde
SE	spin-echo
SNR	signal to noise ratio

4. Publications et communications

4.1 Articles dans des périodiques à comité de lecture

1 Bouhrara M, Clerjon C, Damez JL, Chevarin C, Portanguen S, Kondjoyan A, Bonny JM. Dynamic MRI and thermal simulation to interpret deformation and water transfer in meat during heating. *Journal of Agricultural and Food Chemistry* 2011; 59(4):1229-1235.

2 Bouhrara M, Lehallier B, Clerjon S, Damez JL, Bonny JM. Mapping of muscle deformation during heating: *in situ* dynamic MRI and non-linear registration. *Magnetic Resonance Imaging* 2012; 30(3):422-430.

3 Bouhrara M, Clerjon S, Damez JL, Bonny JM. High-resolution susceptibility-weighted MRI for fast structural imaging. *Magnetic Resonance Materials in Physics, Biology and Medicine*; in preparation.

4 Bouhrara M, Bonny JM. B_1 mapping with selective pulses. *Magnetic Resonance in Medicine* 2012; Online (DOI: 10.1002/mrm.24146).

5 Bouhrara M, Clerjon S, Damez JL, Kondjoyan A, Bonny JM. *In situ* imaging highlights local structural changes during heating: The case of meat. *Journal of Agricultural and Food Chemistry* 2012; 60(18):4678-4687.

4.2 Communications dans des congrès

1 Bouhrara M, Damez JL, Clerjon S, Benmoussa A, Portanguen S, Chevarin C, Kondjoyan A, Bonny JM. MRI assessment of deformation and water loss during meat heating. The 55th International Congress of Meat Science and Technology 2009, Copenhagen/Denmark. *Résumé, Poster et Oral.*

2 Bouhrara M, Damez JL, Clerjon S, Chevarin C, Benmoussa A, Bonny JM. Water expellation during meat heating assessed by MRI. EuroFood Water Conference 2010, Reims/France. *Résumé, Poster et Oral.*

3 Bouhrara M, Damez JL, Clerjon S, Chevarin C, Benmoussa A, Bonny JM. Suivi par IRM de l'expulsion de l'eau du muscle pendant le chauffage. Groupe d'Etude de Résonance Magnétique 2010. Saint-Dié des Vosges/France. *Résumé et Poster.*

4 Bouhrara M, Clerjon S, Damez JL, Benmoussa A, Chevarin C, Bonny JM. *In situ* MR imaging of food during continuous heating. The 17th International Society for Magnetic Resonance Conference 2010. Frienze/Italy. *Résumé et Poster.*

5 Bouhrara M, Clerjon S, Damez JL, Chevarin C, Benmoussa A, Bonny JM. Fast and high resolution dynamic susceptibility weighted MRI of muscle during continuous heating. The 10th International Conference on the Applications of Magnetic Resonance in Food Science 2010, Clermont-Ferrand/France. *Résumé, Poster et Oral.*

6 Bouhrara M, Bonny JM. A fast and accurate method for active B_1 field mapping. Groupe d'Etude de Résonance Magnétique 2011, Sitges/España. *Résumé et Poster.*

IV. Introduction générale

« C'est en cuisant devant le feu son morceau de venaison que l'être primitif cessant d'être une bête féroce est devenu un homme. »
Claude Lévy Strauss

1. Contexte

C'est depuis la maitrise du feu au paléolithique que l'homme a commencé à cuire ses aliments, peut être après avoir goûté aux restes d'un animal piégé dans une futaie après un incendie. Il remarqua sans doute très vite que la chair lui semblait plus facile à mâcher et à ingérer. Des données récentes suggèrent aussi que les hominidés du paléolithique avaient une préférence spontanée pour les aliments cuits (Wobber 2008). Les regroupements humains autour d'un foyer ont ensuite participé à l'ébauche d'une véritable vie sociale. Si bien qu'aujourd'hui la transformation des aliments par des techniques thermiques est une pratique à la fois unique et universelle de l'homme.

Les premières manières de cuire les produits de ses chasses étaient rudimentaires. Les plus primitives étaient la pierrade consistant à cuire les aliments sur une pierre chauffée, le rôti où la viande était embrochée sur une branche ou sur un os dont on a découvert lors de fouilles de nombreux exemplaires aux extrémités carbonisées, l'étouffé où la viande était cuite sous la braise, dans un trou garni de pierres préalablement chauffées ou enveloppée dans une panse ou une vessie. Le bouilli est apparu plus tard dès que l'homme a été capable de fabriquer des récipients.

Toutes ces techniques de cuisson ont parcouru les âges jusqu'à aujourd'hui, au gré de sophistications et d'adaptations aux contraintes et apports des civilisations. L'importance de la cuisson - des viandes en particulier - dans l'évolution de l'homme a fait l'objet d'interprétations contrastées. Généralement, les anthropologues proposent que l'effet principal de la cuisson ait été d'élargir la gamme d'aliments ingérables, contribuant ainsi à une meilleure adaptation de l'homme à des environnements différents. Des hypothèses plus récentes suggèrent que la cuisson ait été un facteur important sur l'évolution en raison de hausse importante due à la cuisson de l'énergie disponible dans les viandes.

De nos jours, c'est très rarement le chasseur qui à la fois tue l'animal, le dépouille, prépare les morceaux de viande et les cuits afin de les consommer. Plusieurs acteurs interviennent dans la chaîne qui conduit de l'animal à la viande prête à être consommée. Outre le distributeur, ces principaux acteurs sont ceux réunis sous les termes d'*industriel* et de *consommateur*. Le consommateur est de nos jours de plus en plus demandeur d'aliments prêts à consommer, et choisit donc d'acheter des viandes précuites et le plus souvent incorporées dans des plats préparés. Il se confronte moins souvent aux critères de choix fondés sur des critères pré-ingestifs comme la couleur, la teneur et répartition du gras, la jutosité apparente ou l'odeur. Il se fonde plus volontiers sur les différentes perceptions mises en jeu lors de la consommation qui le guideront vers la décision future d'un nouvel achat. Les critères d'acceptabilité des produits transformés deviennent alors des critères de texture (tendreté, jutosité) et également de flaveur (odeur et goût). S'il veut les vendre, l'industriel doit donc prendre en compte l'acceptabilité du consommateur pour les aliments qu'il a transformé. De plus, il doit le faire à moindre coût. Pour cela, il doit maitriser et adapter les barèmes de cuisson tout en minimisant les pertes de matière, qui sont principalement des pertes de jus.

Si ce dernier point constitue la cible principale de la thèse, la cuisson des viandes n'a pas pour seul enjeu de conduire à des aliments acceptables. Elle a largement contribué à préserver les hommes des contaminations par des microorganismes pathogènes. En effet, bien que stériles à cœur, les muscles peuvent être contaminés en surface par des bactéries lors des opérations de découpe et de transformation. Dans le cas des viandes hachées, la situation est plus critique puisque le cœur du produit peut aussi être contaminé. La cuisson s'impose donc pour inactiver les bactéries pathogènes présentes, en surface pour les morceaux issus de muscle intact, à cœur pour les viandes hachés. Par exemple, les bactéries *Escherichia coli* entérohémorragiques, connues pour être à l'origine de la "maladie du hamburger" liée à la consommation de steaks hachés non cuits à cœur sont éliminées par une cuisson de 10 minutes à 61 °C (Bertin 2010).

Les bactéries ne sont pas les seuls microorganismes impliqués dans la contamination des viandes, les virus et autres parasites sont aussi présents. Ils peuvent provenir de l'animal vivant ou avoir infecté les produits pendant les transformations (souillures externes). Là encore, la cuisson élimine ces microorganismes. Par exemple, le virus de l'hépatite E est détruit par un chauffage à 71 °C pendant 5 min (Ifip 2009). De même, le parasite responsable de la toxoplasmose est immédiatement détruit dans la viande de porc par un chauffage à 67 °C

(Dubey 1990). Enfin, la cuisson à des températures supérieures à 100 °C, pendant une durée suffisamment longue peut conduire à la stérilisation qui est l'un des moyens modernes de conservation des produits alimentaires.

D'un point de vue nutritionnel, les protéines et les acides aminés font la richesse des aliments d'origine musculaire. Les protéines ingérées sont en général très digestibles et sont donc bien assimilées (~80%). Une amélioration de cette digestibilité augmenterait encore leur assimilation par l'organisme et par conséquent la valeur nutritionnelle de la viande. A ce jour, l'effet bénéfique de la cuisson sur la digestibilité n'est pas démontré. En revanche, et comme nous l'avons vu précédemment, la cuisson des viandes module très significativement tendreté et jutosité, et donc l'aptitude de l'aliment à être déconstruit lors de la mastication, ce qui facilite la biodisponibilité des nutriments. Concernant les lipides, la teneur finale dépend du mode de cuisson des viandes. Or, un apport excessif d'acides gras (notamment saturés et insaturés *trans*) peut avoir des conséquences sur la santé en augmentant de façon très significative les risques de problèmes cardio-vasculaires. Une cuisson par friture augmente la teneur en lipides alors que les autres modes de cuisson la diminue, à la condition de ne pas consommer les jus de cuisson. Enfin, bien que le gain d'énergie dû à la cuisson soit bien connu pour les aliments riches en amidon, cette hypothèse n'a été émise que très récemment pour la viande. A la réserve près de l'utilisation de souris comme modèles, il a été montré que la cuisson augmente considérablement l'énergie obtenue à partir de viande, conduisant à une élévation de la masse corporelle (Carmody 2011). Ces résultats soulignent que les traitements thermiques influencent significativement et positivement le potentiel calorique des viandes.

En parallèle à ces différents effets positifs, la cuisson des viandes s'accompagne d'effets négatifs, et en premier lieu de l'apparition de composés néoformés toxiques. Le chauffage des viandes provoque plusieurs réactions chimiques de dégradation entraînant la disparition de composés initiaux dits thermosensibles et/ou la synthèse de nouveaux composés néoformés comme les benzo[a]pyrènes, les amines hétérocycliques et les hydrocarbures aromatiques polycycliques. Ces deux derniers composés sont des coproduits des réactions à haute température, retrouvés principalement après des cuissons par friture ou sur grill. Bien que ces produits néoformés jouent un rôle positif pour les propriétés organoleptiques des aliments (goût grillé, fumé et/ou caramélisé), de nombreuses études épidémiologiques (Layton 1995, Potter 1999, Norat 2005) montrent une relation entre la consommation de viandes frites ou grillées et le développement de certains cancers.

Subject	Authors	Conclusion
Effect of temperature on myofiber denaturation	Palka & Daun, 1999	• Myofibrillar proteins denature between 50 °C and 90 °C. • Myofibrillar denaturation reduces protein water-binding capacity.
	Tornberg, 2005	• Most heat-sensitive is α-actinin, it denatures at 50 °C. • Most heat-resistant is nebulin, it denatures at T ≥ 80 °C.
Effect of temperature on collagen contraction in relation with myofiber denaturation	Palka & Daun, 1999	• Wavy collagen fibers begin to contract at 58 °C.
	Tornberg, 2005	• When collagen becomes straight, it compresses myofiber.
	Lepetit et al., 2000 Lepetit, 2007	• Fiber starts to shrink before collagen compression.
Relation between protein denaturation and CL*	Palka & Daun, 1999	• Inverse proportionality between sarcomere length and CL.
	Bendall and Restall, 1983	• Majority of CL results from collagen contraction.
	Lepetit et al., 2000	• CL depends both on collagen compression and resistance of myofiber.
Effect of muscle type on CL*	Rhee et al., 2004	• Ranking of CL for 11 beef muscles: *ST*** loses the most juice *BF*** the least.
Effect of myofiber orientation on CL*?	Locker & Daines, 1974	• Important effect due to lower CL measured from the longer samples.
	Laroche, 1982	• Important effect, definition of an anisotropy factor.
	Bouton et al., 1976	• Very limited effect and difficult to separate it from heat transfer effects.
Effect of meat ageing on CL*	Shanks et al., 2002	• CL of ground beef patties decrease strongly during the first 5 days pm, weaker afterwards but effect of ageing significant on CL even at 14 days pm.
Effect of pre-freezing on CL*	Paul & Child, 1937	• Important CL differences for *LD** (at 58 °C) but effect of thawing during cooking on temperature kinetic not taken into account.
	Shanks et al., 2002	• Freezing/thawing before cooking erases ageing-related CL differences.
	Petrovic, Grujic & Petrovic, 1993	• Faster freezing rates leads to lower CL but very weak effect.
	Boles & Swan, 2002a	• Pre-freezing meat has little effect on the final mass of cooked meat.
	Pietrasik & Janz, 2009	• No significant effect on CL.
Effect of time period during which meat is stored frozen on CL*	Boles & Swan, 2002b	• Contrasted effect according to breed of the animal.
	Jakobsson & Bengtsson, 1973	• Relatively insignificant even after long storage periods, 2% increase in CL after 9 months in frozen storage.

*CL = Cooking losses.
**ST = Semitendinosus, BF = Biceps Femoris, LD = Longissimus Dorsi.

Tableau 1: Revue de littérature sur les effets des traitements thermiques sur la variation de la structure de la viande et sa relation avec les pertes à la cuisson. Conclusions de la littérature sur les effets de la maturation et de la pré-congélation de la viande sur les pertes à la cuisson. (D'après (Oillic 2011)).

Au delà de la formation de composés néoformés, le chauffage de la viande induit une perte de masse qui peut atteindre 30% (Oillic 2011), sous forme d'un jus composé à 90% d'eau. Cette perte détermine le rendement technologique de la cuisson, qui est un facteur critique dans l'industrie agroalimentaire. Elle a non seulement un coût pour l'industriel qui vend principalement ses produits au poids, mais elle affecte également les qualités organoleptiques de la viande cuite en dégradant la jutosité, qui diminue elle-même la tendreté perçue. De plus, certains micronutriments présents dans les viandes sont partiellement évacués avec le jus de cuisson, ce qui est massivement le cas pour le fer, le zinc et le sélénium (Kondjoyan 2008), diminuant ainsi la qualité nutritionnelle de l'aliment. Lors des traitements thermiques, la structure et/ou l' « état de liaison » des micronutriments (vitamines E, A et du groupe B, fer, zinc, sélénium) peuvent être modifiés. Les vitamines, sont sensibles à la chaleur et leur teneur peut être réduite par des cuissons longues ou en présence d'eau (braisé, bouilli). La liaison du fer avec les macromolécules peut être rompue par l'élévation de température, libérant ainsi du fer libre. Or le fer libre en excès est pathogène car il favorise la formation de radicaux libres (Culioli 2003) qui endommagent de manière irréversible les principaux constituants des cellules de l'organisme. Aussi, 20 à 50% de la teneur initiale en vitamines B peut disparaitre au cours de l'opération de cuisson (Culioli 2003). Ceci a notamment été observé sur des rôtis de porc dans les services de restauration en collectivité ou à domicile (Lassen 2002). En fait, les pertes de cuisson sont le résultat de phénomènes complexes qui dépendent des conditions de cuisson, des caractéristiques zootechniques (espèce, âge, sexe, type de muscle), de l'état de maturation de la viande et des conditions de stockage et de découpe avant la cuisson (Tableau 1).

2. Objectifs de la thèse

Il n'est pas envisageable d'aborder la maitrise du procédé de cuisson dans la viande en prenant en compte l'ensemble des effets positifs et négatifs. **L'objectif de cette thèse est d'établir des relations quantitatives fiables entre température, déformations et transferts d'eau dans la viande, et d'en expliquer les mécanismes**.

L'évolution de la structure de la viande au cours de procédés thermiques a été abordée par plusieurs études. Elles ont établi que les protéines se dénaturent au cours du chauffage (Martens 1982, Micklander 2002) induisant une destruction des membranes des cellules

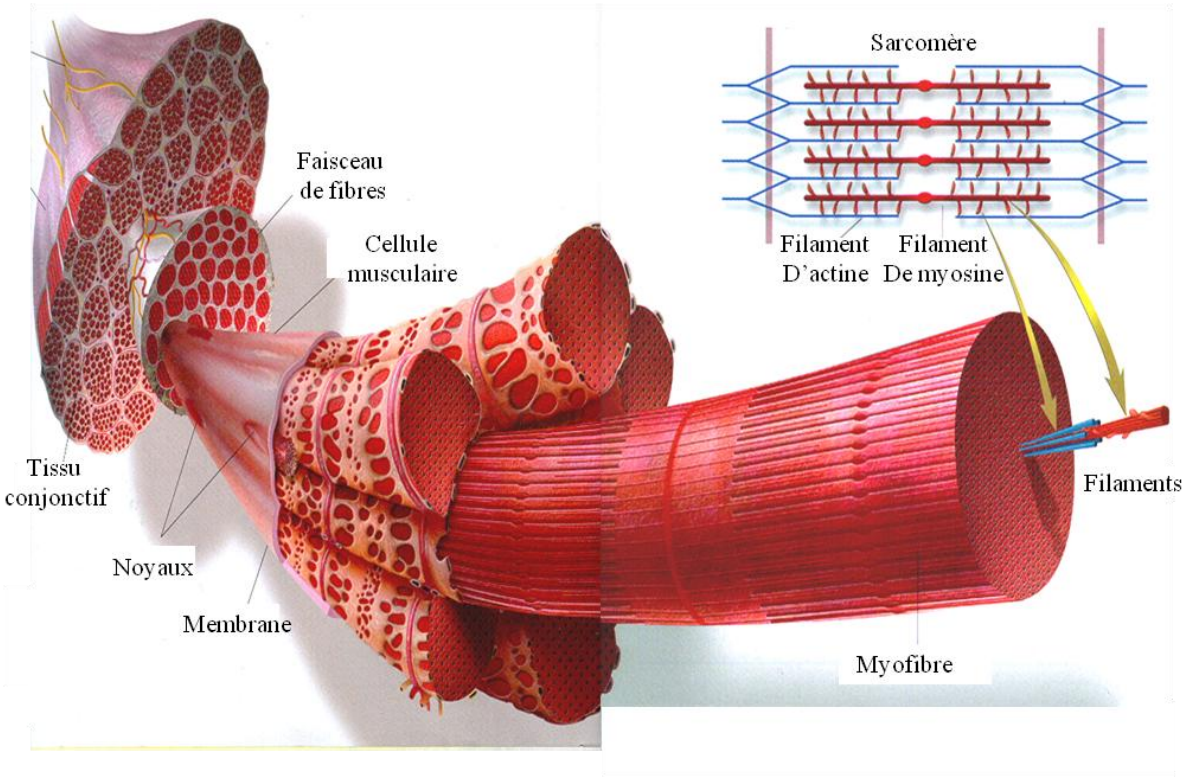

Figure 1 : Schéma de la structure multi-échelle du muscle.

(Hamilton 1967, Tornberg 2005), que les myofibres se contractent à la fois transversalement et longitudinalement (Bendall 1983) et que le collagène se solubilise (Stabursvik 1980, Lepetit 2008). Néanmoins, cette littérature est porteuse de contradictions qui rendent difficile l'interprétation des phénomènes observés. Par exemple, Davey *et al.* (Davey 1974) n'observent aucune contraction transversale du muscle *sternomandibularis* de bœuf durant le chauffage entre 40-50 °C, contrairement à Bendall *et al.* (Bendall 1983) qui constatent une contraction à partir de 40 °C. Il existe aussi un désaccord concernant la température de la contraction longitudinale des fibres musculaires. Il a été rapporté par Hostetler *et al.* (Hostetler 1968) que les contractions longitudinales et transversales débutent ensemble aux alentours de 40 °C, au contraire de Bendall *et al.* (Bendall 1983) qui indique une contraction longitudinale des fibres à partir de 60 °C. Enfin, la température du début de la dénaturation de la myosine (protéine intracellulaire des fibres musculaires) reste un sujet de controverse et n'a jamais été clairement mesurée (Martens 1982, Micklander 2002). Des divergences apparaissent aussi dans les études mesurant l'impact de la température sur les propriétés qualitatives de la viande cuite à l'échelle macroscopique. En effet, Tornberg *et al.* (Tornberg 2005) constate une augmentation de la tendreté de la viande avec la température jusqu'à 60 °C précédant une baisse significative, ce qui contredit les résultats de Christensen *et al.* (Christensen 2000) décrivant une baisse continue de la tendreté avec la température.

La structure hétérogène et complexe de la viande (organisation multi-échelle de fibres enchâssées dans un réseau conjonctif (Figure 1)) rend les expérimentations et interprétations particulièrement difficiles. Ceci oblige à émettre des hypothèses de travail simplificatrices et/ou à mettre en œuvre des approches réductionnistes. Par exemple, la plupart des études citées précédemment considèrent une température homogène dans l'échantillon et isolent un constituant d'intérêt pour étudier son comportement à la température. Par ailleurs, les techniques couramment utilisées sont le plus souvent destructives, comme par exemple la microscopie et l'histologie, et/ou non localisées, comme la spectroscopie RMN (Damez 2008). Elles induisent alors des biais lors de l'analyse de la structure musculaire.

Dès lors, une analyse locale et dynamique sur un échantillon macroscopique représente une nouvelle façon d'étudier la cuisson de la viande, en limitant les hypothèses de travail simplificatrices et sans réductionnisme. Le propos n'est pas d'étudier le tout sans se préoccuper des parties, mais de modéliser le tout à partir des mesures expérimentales et

de l'interpréter à la lumière des connaissances préalablement acquises sur le comportement individuel des parties.

L'imagerie en général est capable de fournir des informations locales, et l'imagerie par résonance magnétique nucléaire (IRM) en particulier sur la structure et certaines propriétés physico-chimiques de l'eau dans les matrices agroalimentaires (Hills 1995, Gotz 2006). Etant non destructive, l'IRM permet de suivre l'évolution de la structure et des propriétés des aliments soumis à des contraintes physiques et/ou chimiques, et (parfois) de comprendre les mécanismes mis en jeu (Bonny 2001, Bertram 2004, Shaarani 2006). Elle a permis par exemple d'effectuer des mesures *in situ* pour suivre l'évolution de la viande lors des traitements technologiques, dont le chauffage (Bertram 2004, Barutcu 2009). Pour toutes ces raisons, **l'IRM est notre technique d'élection**. Pour autant les contraintes de l'IRM dynamique nous ont conduit à formuler trois interrogations, (i) est-il possible de mettre en œuvre des méthodes pour explorer dynamiquement et quantitativement l'évolution de la structure et des transferts de matière dans la viande au cours d'un chauffage ? (ii) quelle stratégie faut-il adopter pour en tirer des modèles fiables ? (iii) Comment interpréter les mécanismes à partir de ces modèles en tenant compte de la variabilité des échantillons musculaires ? C'est autour de ce triple questionnement que nous avons articulé notre réflexion et au travers des cinq publications qui jalonnent ce manuscrit.

En éclairant d'un angle nouveau ce champ de recherche grâce à l'IRM, ce travail intéresse plusieurs publics. Il a été montré (Shackelford 2001) que les consommateurs de viande sont prêts à payer un prix élevé pour ce produit, à la condition d'une qualité organoleptique constante en termes de tendreté et de jutosité. L'établissement de barèmes de cuisson optimisés permettrait de répondre à cette attente. Sur ce sujet, l'intérêt technologique de l'industriel fait écho à l'intérêt organoleptique du consommateur. A la perspective de ventes améliorées par la garantie d'un produit de qualité constante s'ajoute aussi la promesse d'une maîtrise énergétique grâce à une cuisson optimisée : plus de gains, moins de dépenses … Les sorties de cette thèse pour la communauté scientifique ciblent deux fronts bien distincts. Si les développements menés en IRM sont génériques, ils seront utiles à la communauté des spécialistes de cette technique d'imagerie. L'autre front est constitué par les spécialistes des procédés de transformation de la viande (appartenant à des centres techniques, à des instituts de recherche ou à des entreprises de transformation des produits animaux) qui portent généralement un intérêt aux mécanismes qui lient température, déformation et transferts d'eau

pendant la cuisson des viandes. Enfin, ce travail pluridisciplinaire s'inscrit pleinement dans les orientations de l'INRA en contribuant à rationaliser la construction des aliments dans le respect des attentes du consommateur.

V. Revue de la littérature

1. Evolution de la structure et des transferts de matière dans la viande sous contraintes thermiques

La cuisson de la viande déclenche des phénomènes physiques complexes, et la mauvaise conduite de ce procédé peut aboutir à des conséquences délétères en termes de sécurité sanitaire et de qualités organoleptique, nutritionnelle et technologique. Sans être exhaustif, ces changements physico-chimiques sont essentiellement: (i) les transferts d'eau, de matières grasses et de micronutriments, (ii) les transferts de chaleur, (iii) les réactions chimiques et en particulier la réaction de Maillard qui entraine la création de nouveaux composés d'arôme ainsi qu'une modification de la couleur, (iv) l'oxydation des lipides, (v) la dénaturation des protéines et la déformation. Il est également légitime, lorsque l'on parle des profonds changements affectant un aliment, de considérer les modifications de la perception du produit par le consommateur. Les synthèses bibliographiques sur la cuisson des viandes abordant ces questions dans leur ensemble sont rares. Elles ne ciblent souvent qu'une partie des mécanismes mis en jeu.

Les mécanismes mis en jeu lors de la cuisson étant extrêmement nombreux, cette revue de la littérature se focalise sur les travaux relatifs aux transferts de chaleur, à la dénaturation des protéines, à la contraction et aux transferts d'eau qui sont les quatre problématiques au cœur de cette thèse.

1.1 Transferts de chaleur

La maîtrise de la cuisson passe d'abord par la connaissance de l'évolution de la température dans le produit au cours du procédé. Cette évolution dépend d'abord des conditions auxquelles est soumis le produit. Elle dépend aussi du produit lui-même puisque la conductivité thermique de la viande varie avec sa composition, et cette dernière avec la température (Rahman 1995). Deux approches expérimentales sont généralement utilisées pour

connaitre la température dans le produit : la mesure expérimentale ou la simulation numérique. Avec les progrès des moyens de calcul qui peuvent intégrer des connaissances *a priori* sur les propriétés thermiques de la viande, la simulation numérique prend le pas sur la mesure expérimentale, qui reste pourtant indispensable lors de la validation des simulations.

Expérimentalement, la température est classiquement mesurée au moyen de thermocouples placés directement dans l'échantillon à des positions d'intérêt (Rinaldi 2012). Cette solution est loin d'être idéale, puisqu'elle perturbe le procédé thermique, implique un contact entre le produit et le capteur source possible de contamination, et donne une mesure en un seul point. D'autres méthodes physiques, initialement développées pour les applications biomédicales, sont utilisables en sciences des aliments et plus particulièrement lors de la cuisson. Il s'agit de l'IRM, des tomographies par rayons X et par impédance électrique, des approches ultrasonores et de la radiométrie hyperfréquence pour les mesures à l'intérieur de l'échantillon et des techniques infrarouges pour les mesures en surface (Gowen 2010). L'IRM en particulier permet de cartographier la température indirectement en mesurant des paramètres thermosensibles, essentiellement le coefficient de diffusion apparent (Delannoy 1991), le temps de relaxation T_1 (Dickinson 1986) et le déplacement chimique (Hall 1985). Cette dernière approche est la plus utilisée car elle est à la fois sensible, rapide et spécifique (les valeurs du coefficient de diffusion apparent et du T_1 ne dépendant pas seulement de la température). Il s'agit cependant d'une méthode relative qui ne mesure que la différence de température par rapport à un état de référence. Cette méthode a été utilisée pour étudier la cuisson des pommes de terre (Kantt 1997, Ye 2003), d'aliments en sauce ou de matrices modèles (Nott 2000, Rakesh 2010). En résumé, la mesure de la température à l'intérieur d'un échantillon est soit invasive avec l'utilisation de thermocouple, soit non invasive avec l'utilisation de technique d'imagerie dont l'IRM, qui demeurent néanmoins encore confinées à des mesures de laboratoire.

Les premières simulations numériques de la distribution de la température dans la viande pendant la cuisson ont été fondées sur des modèles de conduction développés à l'université de Bristol, dédiés initialement aux procédés de réfrigération. Ne prenant en compte ni la déformation, ni les transferts d'eau, cette approche a rapidement montré ses limites (Burfoot 1983). Dans un second temps, la viande sous contrainte thermique a été modélisée comme un produit de conduction thermique constante mais se contractant avec la température (Fowler 1991). Cette prise en compte de la déformation a permis notamment d'estimer plus

précisément la température au centre de l'échantillon (Califano 1997). Les variations de composition des produits ont finalement été considérées, et notamment les coefficients de transfert à la surface des produits qui sont loin d'être constants tant spatialement que temporellement (Burfoot 1988). Les transferts de chaleur et de matière, notamment les phénomènes de convection d'eau et de lipides, ont été pris en compte lors de la cuisson de viande hachée (Shilton 2002). Une telle complexification permet d'aboutir à des modèles très réalistes et ainsi d'utiliser l'outil numérique pour la compréhension et l'optimisation de la cuisson, dans le but ici de maitriser le risque sanitaire lié à la présence des bactéries *Escherichia Coli* entérohémorragiques. En résumé, pour disposer de simulations numériques précises de la température pendant la cuisson, il est nécessaire d'élaborer des modèles de transfert de chaleur qui prennent en compte les variations de composition (transferts de matière, changements de phase et de nature) et de forme de l'aliment (Pan, 2000). Enfin, la mise sur le marché d'outils logiciels de modélisation performants pouvant intégrer ces paramètres, tels que le logiciel COMSOL Multiphysics, a récemment accéléré le développement de la modélisation de la température pour l'étude de la cuisson (Goñi 2010, Rakesh 2010).

1.2 Dénaturations protéiques

Les protéines constituent 20 à 37 % de la composition de la viande (Afssa 2007) et présentent le principal intérêt nutritionnel de ce produit. Les protéines de la viande sont habituellement classées selon qu'elles appartiennent aux myofibrilles (actine, myosine, …), au sarcoplasme (myoglobine, …) ou au tissu conjonctif (collagènes, élastine, …). Lors de la cuisson, l'augmentation de la température dénature ces protéines ce qui affecte la structure de la viande, notamment en modifiant les interactions eau-protéines. Nous relatons ici les principaux mécanismes de dénaturation, indispensables à la compréhension des phénomènes en jeu pendant la cuisson des viandes (Tornberg 2005).

La dénaturation des protéines lors du chauffage suit principalement trois étapes. La perte de la structure hélicoïdale des protéines, suivie d'une phase d'interaction entre les protéines. Cette interaction conduit, pour la plupart des protéines sarcoplasmiques, à la formation d'un gel entre 40 et 60 °C (Hamm 1977). Ce gel est un déterminant important de la texture en bouche de la viande cuite puisqu'il joue un rôle de lubrifiant lors de la mastication (Tornberg 1997). Les températures autour desquelles s'articulent ces trois phénomènes varient selon les études.

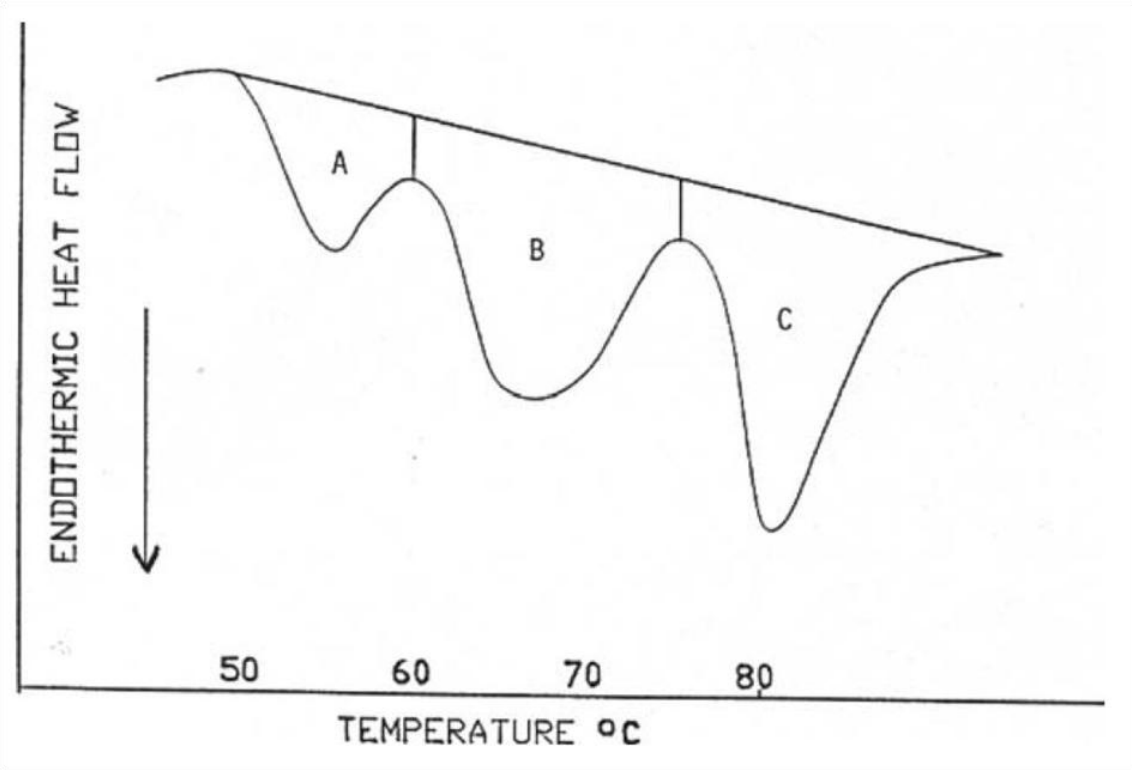

Figure 2 : Courbe type des transitions thermiques dans le muscle : A, myosine, B, protéines sarcoplasmiques et collagène et C, actine (d'après (Findlay 1986)).

La température de dénaturation des protéines a été principalement mesurée par calorimétrie différentielle à balayage. La figure 2 (Findlay 1986) représente la courbe des transitions thermiques obtenues dans le muscle par cette technique. La première transition (A) présente un maximum entre 54 et 58 °C et a été attribuée à la dénaturation de la myosine (Wright 1977). La seconde (B), entre 65 et 67 °C, a été attribuée au collagène (Stabursvik 1980) ainsi qu'aux protéines sarcoplasmiques (Wright 1977). La troisième transition (C) correspond à la dénaturation de l'actine et a été observée entre 80 et 83 °C (Wright 1977). Dans une étude postérieure, Martens (1982) a mis en évidence la dénaturation du collagène entre 53 et 63 °C. Il attribue cette large gamme de température à la mise en jeu de deux phénomènes successifs : la rupture des liaisons hydrogènes, la stabilité thermique de ces liaisons augmentant avec l'âge de l'animal (Shimokomaki 1972), puis la contraction du collagène. La dénaturation des protéines musculaires pendant la cuisson joue un rôle primordial dans la contraction et la perte en eau, deux phénomènes que nous traitons maintenant et qui impactent la qualité finale des produits.

1.3 Déformation

Chacun a pu observer qu'un morceau de viande se contracte à la cuisson en expulsant du jus, ce qui conduit à une viande dure et sèche. Si plusieurs propriétés de texture sont influencées par la cuisson (tendreté, élasticité, «masticabilité », friabilité) (Barbera 2006, Bertram 2004b), le rôle spécifique de certains composants dans la contraction de la viande a été mis en évidence pour les protéines myofibrillaires, le cytosquelette, le tissu conjonctif (Silva 1993, Palka 1999, Astruc 2010). D'après Bendall *et al.* (1983) et Tornberg *et al.* (1997, 2005), la contraction résulte (i) de tensions transversales ou longitudinales à l'axe des fibres musculaires provoquées par les myofibres et les faisceaux de fibres musculaires, (ii) de la formation et de l'agrégation de gels de protéines sarcoplasmiques, et (iii) de la contraction et dénaturation du collagène intervenant à différentes températures. La contraction transversale débute entre 35 °C et 40 °C et suit une augmentation linéaire avec la température. Dans le sens longitudinal, la viande se contracte à partir de 60 °C et de façon plus marquée après 65 °C, en raison de la contraction conjointe du collagène à partir de 64 °C (Mohr 1969) et des fibres musculaires entre 60 °C et 70 °C. Ces trois paliers de déformation ont aussi été rapportés par Bailey *et al.* (1989), où entre 40 °C et 50 °C est observée la dénaturation des protéines myofibrillaires (principalement la myosine), entre 60 °C et 70 °C la dénaturation du collagène (ce qui confirme les résultats de Mohr *et al.* 1969), et enfin entre 70 °C et 90 °C

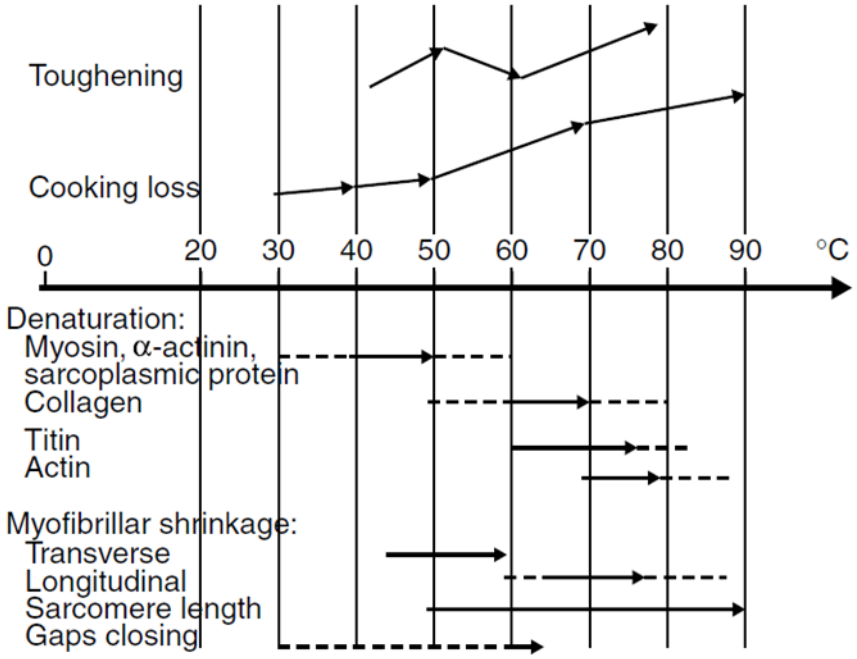

Figure 3 : Changements dans la viande pendant le chauffage (d'après (Bejerholm 2004)).

la contraction et déshydratation de l'actomyosine (Figure 3).

Ces résultats mettent en évidence de nombreuses températures de transition qui occasionnent des déformations pendant la cuisson des viandes. Ils ont été obtenus par approche réductionniste, c'est-à-dire sur des extraits de protéines, de fibres isolées, voir de faisceaux de fibres. Pour une même protéine cible, il n'y a pas de consensus sur les températures de contraction, ce qui est certainement dû aux différences de méthodes d'extraction, de préparation des échantillons et/ou d'analyse (plus ou moins invasives). Si elles facilitent l'interprétation des mécanismes, de telles études ne préjugent pas du comportement d'un échantillon macroscopique, qui est l'échelle réelle des aliments traités par les procédés thermiques.

1.4 Transferts d'eau

L'eau est le composant principal de la viande. La teneur en eau est un déterminant particulièrement important de la qualité finale des produits et en particulier de leur jutosité (Hamm 1960). La rétention de l'eau lors de la cuisson a été principalement reliée à la dénaturation des protéines (~20% du poids des muscles) (Bouton 1972, Laakkonen 1973) : cette dénaturation entraine une perte en eau qui n'est plus « retenue » par les protéines musculaires. Hearne (1978) a complexifié l'approche en rapprochant les pertes en eau à la cuisson aux propriétés mécaniques du produit ainsi qu'à sa microstructure. Il a ainsi montré que l'augmentation de la perte en eau avec la température correspond à une diminution du diamètre des fibres musculaires et de la longueur des sarcomères, ces phénomènes étant finalement associés à une diminution des forces de cisaillement et donc de la dureté de la viande. Plus récemment, la dénaturation des protéines musculaires à la chaleur et la modification qu'elle entraine sur les propriétés de l'eau dans le produit cuit ont été reliées à la texture (Bertola 94, Wattanachant 2005, Tornberg 2005). Lors de la cuisson de la viande, les procédés thermiques ont des conséquences directes sur la tendreté finale du produit qui globalement augmente avec le chauffage (Rao 1986, Tornberg 2005), et sur une évolution de la couleur due principalement à l'oxydation de la myoglobine (Garcîa-Segovia 2007).

Le jus expulsé pendant la cuisson des viandes est un liquide composé de près de 90% d'eau, c'est pourquoi on parle communément d' « eau » (Oillic 2011). La matière sèche restante

contenue dans les jus est composée de lipides et de sel minéraux (Gerber 2009). Les premières études sur les transferts d'eau dans la viande pendant la cuisson ont été menées en faisant l'hypothèse de forces mécaniques conduisant à une expulsion d'eau à la manière d'une éponge pressée (Murphy 2000). Les forces exercées ont été attribuées à la contraction du collagène en raison de corrélations significatives mesurées entre teneur en collagène et quantité d'eau expulsée. Cette hypothèse a été rapidement remise en cause en évoquant que l'effet d'une contrainte mécanique dépend de l'interaction de l'eau avec son environnement (interaction et compartimentation). Dans la viande, les mesures RMN à l'échelle macroscopique montrent que l'eau présente grossièrement trois « états » de mobilité (Hazelwood 1974, English 1991). Si la correspondance entre ces trois fractions et un compartiment anatomique précis est sujet à controverse dans un milieu aussi complexe - en composition et en organisation - que le muscle, il est probable que les cinétiques d'expulsion de l'eau dépendent de la mobilité de l'eau et des proportions respectives de ces trois fractions (Bertram 2002, Brown 2000).

Certains transferts d'eau ont pu être reliés aux contraintes mécaniques pour expliquer certains mécanismes (Fowler 1991). Une première expulsion de l'eau a lieu lors de la phase de contraction latérale des fibres, ce qui forme des « canaux » où l'eau peut circuler. La phase suivante de contraction du collagène (Bendall 1983, Micklander 2002) conduit à une expulsion de l'eau en dehors de la viande. C'est ce dernier mécanisme qui conduit d'ailleurs à recommander une cuisson des viandes à basse température, afin d'éviter cette phase finale de contraction pour conserver un maximum d'eau dans le produit.

2. L'imagerie par résonance magnétique nucléaire

2.1 Généralités

En première approximation, l'IRM peut être vue comme une extension de la spectroscopie RMN où le signal en chaque voxel de l'image (élément de volume dans l'espace) rend compte des propriétés des spins contenus dans ce volume. Comme en spectroscopie, le principe est d'abord d'appliquer des impulsions radiofréquences (à une fréquence proche de la fréquence de résonance des spins) et de gradient de champ magnétique pour détecter des *cohérences* particulières. Il s'agit de créer les conditions pour que les moments magnétiques portés par les

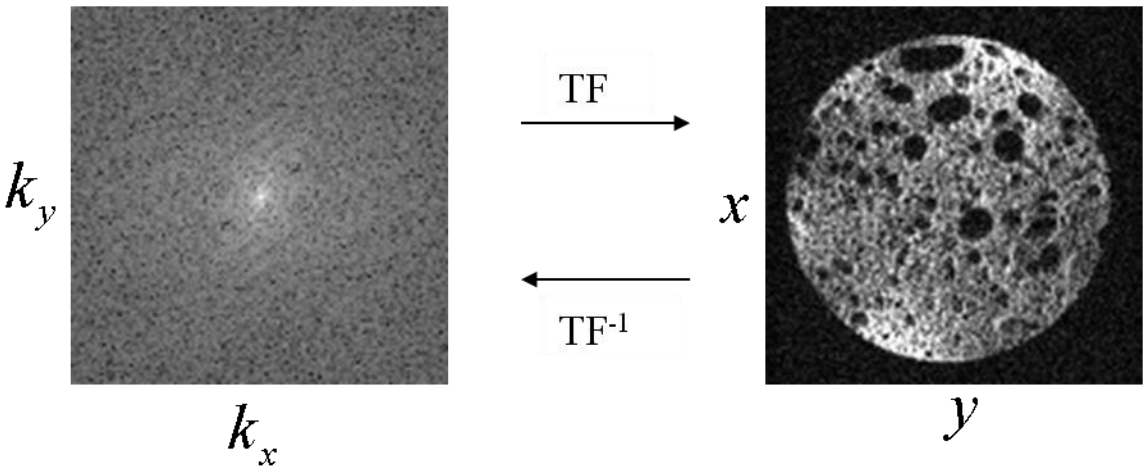

Figure 4 : Module de l'espace-k (à gauche) correspondant à l'image (à droite) obtenue par microscopie RMN montrant une pate à pain en fermentation (d'après (Bonny 2004)).

spins soient cohérents en phase à l'échelle microscopique pour induire un signal détectable. A ces contraintes s'ajoute la nécessité en imagerie d'effectuer un codage spatial afin de connaitre *a posteriori* la localisation du signal. Il a été montré que l'application de gradients revenait à se déplacer dans un espace réciproque, appelé espace-k, résultant de la transformée de Fourier inverse de l'image (Figure 4) (Twieg 1983). Les différentes stratégies de codage spatial reviennent toutes à remplir l'espace-k avec le signal RMN, en une ou plusieurs fois (donc plus ou mois rapidement), et selon des trajectoires diverses (cartésiennes, spiralées, stochastiques …). Ce codage spatial a l'avantage d'être effectué en faisant varier l'amplitude des gradients, donc sans faire varier la position des émetteurs/détecteurs comme en tomographie. Par ailleurs, l'accès à différents noyaux et la manipulation des cohérences permet d'accéder à différents contrastes (mobilités translationnelle et rotationnelle, densité de spin,…). Au delà de l'information contenue dans une seule image, l'IRM multidimensionnelle permet de quantifier certains paramètres physico-chimiques (Bonny 2005) ou de caractériser des processus dynamiques, comme dans ce travail de thèse ou encore en imagerie fonctionnelle (Ogawa 1992). Il faut noter que, pour beaucoup d'applications en IRM, on fait appel à des aimants dont l'intensité du champ magnétique est toujours plus élevée afin d'augmenter le rapport signal sur bruit, ce qui conduit notamment à de meilleures résolutions spatiale et/ou temporelle.

2.2 L'IRM en agroalimentaire

L'IRM est une technique d'imagerie à la fois quantitative et multi-contraste. Elle est bien adaptée à l'étude des aliments qui sont pour la plupart - et c'est le cas de la viande - riches en eau et dans une phase « gel » (semi-solide). Son caractère non destructif autorise en particulier les études dynamiques *in situ* sur des aliments soumis à des contraintes physiques et/ou chimiques, d'où son intérêt dans le domaine du génie des procédés agro-alimentaires. D'une façon générale, l'IRM a été utilisée pour l'étude de la structure et des interactions entre les constituants de matrices agroalimentaires très variées (McCarthy 1996, Gladden 1996), comme des fruits (Clark 1997, Abbott 1999, Kerr 1997, Galed 2004, Musse 2009), des légumes (Clark 1997, Hall 1998, Abbott 1999, Koizumi 2006), des fromages (Rosenberg 1991, Mahdjoub 2003, Altan 2011), des produits chocolatés (Guiheneuf 1997a), des pâtes (Kojima 2001), des grains de riz (Kasai 2007), des viandes (Guiheneuf 1997b, Bonny 2001, Bertram 2004), des poissons (Bock 2002, Van der Linden 2004) et des biscuits (Yan 1996), ainsi que pour la conception de nouveaux aliments modèles (Hills 1995, Amin 2007). Outre

l'analyse de la structure, l'IRM représente un outil puissant dans la quantification de la densité des noyaux d'intérêt, essentiellement ^{1}H et ^{23}Na (Nott 1999, Laurent 2000, Veliyulin 2007, Antequera 2007, Kasai 2007, Veliyulin 2009, Musse 2009). Il en est de même pour le suivi des aliments pendant le stockage, la transformation, la conservation ou encore du chauffage (Evans 1998, Nott 1999b, Nott 2000, Renou 2003, Vestergaard 2005, Cabrer 2006, Shaarani 2006, Hansen 2008, Wagner 2008a, Wagner 2008b, Altan 2011).

L'étude de la distribution de l'eau dans la viande sous contraintes thermiques a été abordée par spectroscopie RMN du ^{1}H (Fjelkner-Modig 1986, Borisova 1992, Tornberg 1993, Micklander 2002, Bertram 2004). Ces études fondées sur une décomposition multiexponentielle des courbes de relaxation T_2 notent une décroissance significative de la population majoritaire durant le chauffage (Tornberg 2005). Cette diminution est attribuée à la dénaturation de certaines protéines majoritaires qui modifierait les interactions eau-macromolécule, et simplement à la contraction des fibres et du tissu conjonctif, qui provoque l'expulsion de l'eau à l'extérieur de l'échantillon. Néanmoins, les résultats de ces études restent difficiles à interpréter en l'absence d'informations sur la localisation spatiale de ces populations d'eau. A notre connaissance, une seule étude a été réalisée par IRM afin d'évaluer quantitativement l'impact du chauffage sur la viande en mesurant les paramètres intrinsèques locaux (T_1, T_2 et densité de protons) de l'échantillon. Les résultats de cette étude décrivent une perte d'eau associée à une diminution de sa mobilité avec une différence spatiale entre le centre et la surface de l'échantillon (Shaarani 2006).

VI. Travail personnel

Cette thèse aborde la question suivante : « Peut-on prédire l'effet de la température sur la déformation et les transferts d'eau dans la viande pendant la cuisson ? ». Pour y répondre, notre démarche expérimentale vise à obtenir simultanément trois paramètres pendant une cuisson, afin de quantifier déformation et transferts d'eau en fonction de la température et d'interpréter leurs dépendances. Pour cela, l'idée est d'utiliser l'imagerie afin d'obtenir ces informations localement et donc de prendre en compte les hétérogénéités dans l'échantillon. Enfin, disposer d'une mesure multiparamétrique en chaque point (plus exactement en chaque *voxel*) de l'image est une façon de multiplier les mesures dans un même échantillon, et donc de porter un regard statistique sur l'information disponible.

Pour mener à bien ce projet, notre technique d'élection est l'IRM en raison notamment de son caractère non destructif. De plus, l'IRM est capable d'apporter une information structurelle pour quantifier la déformation du muscle et une autre relative à la densité de protons pour mesurer les transferts d'eau.

Notre stratégie est dans un premier temps **de montrer la faisabilité du suivi *in situ* d'une cuisson par IRM**. Il s'agit essentiellement (i) de développer un dispositif pour faire cuire l'échantillon de viande en environnement magnétique dans des conditions de température standardisées (ii) d'obtenir des images RMN de qualité suffisante pendant tout le régime de cuisson, (iii) de valider notre approche numérique de cartographie de la température dans l'échantillon.

Pour **mesurer déformation et quantité d'eau par IRM pendant la cuisson**, de nombreux autres développements méthodologiques sont nécessaires. Il s'agit d'abord de maitriser les conditions de mesure afin de disposer d'images permettant de suivre la déformation du muscle avec les résolutions spatiale et temporelle suffisantes, et *in fine* de reconstruire les champs de déformation. Il s'agit ensuite de cartographier la quantité d'eau et s'affranchir ainsi du biais introduit par les variations du champ émetteur et récepteur de l'antenne RF. Ce champ devra donc être mesuré dans les meilleures conditions possibles.

Ce n'est qu'une fois la démarche expérimentale optimisée que nous aborderons **les relations entre température, déformation et transferts d'eau**, et ce sur deux types de muscles.

Nous avons choisi de présenter les résultats de cette thèse sous la forme des cinq articles qui ont été rédigés et soumis à publication dans des revues internationales à comité de lecture. Chaque article est précédé d'une présentation qui résume les objectifs et les résultats principaux, et revient en particulier sur l'articulation entre les différents articles.

1. Article 1 : Suivi *in situ* de l'évolution structurale du muscle au cours du chauffage par IRM

Nous avons montré dans la revue bibliographique en quoi les modifications structurales de la viande pendant la cuisson déterminent les qualités du produit final. Cette revue a par ailleurs mis en évidence des conclusions contradictoires, dues sans doute à des hypothèses simplificatrices (homogénéité de température dans l'échantillon) ou des limites méthodologiques. La possibilité nouvelle de suivre localement et *in situ* ces modifications structurales constitue un progrès considérable pour coupler déformation et température à une échelle mésoscopique.

Les travaux présentés dans ce premier article montrent la faisabilité du suivi par IRM de la viande sujette à une cuisson lente entre 20 et 75 °C. Pour cela, un dispositif de cuisson compatible avec l'environnement RMN a été conçu et construit. Il utilise un liquide pour chauffer l'échantillon, gage d'une meilleure homogénéité des échanges thermiques. Pour des raisons essentiellement pratiques, l'eau a été choisie comme fluide thermoporteur, ce qui a imposé d'introduire des motifs de saturation dans les séquences d'IRM afin de corriger les artefacts dus à l'eau circulante. De plus, le suivi d'une déformation nécessite de mettre en évidence des marqueurs liés à la structure de l'échantillon, et donc d'avoir des images suffisamment contrastées à toutes les températures. Une séquence sensible aux différences locales de susceptibilité magnétique a donc été choisie puisqu'elle met en évidence le réseau conjonctif intramusculaire.

En outre, la température a été cartographiée par simulation numérique pendant toute la durée du procédé, afin de relier cette information à la déformation obtenue par IRM. Un modèle numérique des transferts thermiques dans l'échantillon a donc été mis au point et validé en collaboration avec une autre équipe de l'unité, experte en modélisation.

Ce premier travail a permis d'aboutir à des images RMN qui mettent en évidence l'évolution de la structure musculaire en fonction de la température, tout au long de la cuisson. Ces images montrent aussi la perte d'eau depuis le muscle vers l'extérieur, en passant par les espaces créés entre les faisceaux de fibres musculaires.

L’ensemble de ces développements et résultats a rapidement donné lieu à la rédaction d’un article pour acter la faisabilité du suivi *in situ* par IRM des modifications structurales de la viande pendant la cuisson.

Cet article a été publié début 2011 dans *Journal of Agricultural and Food Chemistry* (Bouhrara 2011a).

Dynamic MRI and thermal simulation to interpret deformation and water transfer in meat during heating

Mustapha Bouhrara, Sylvie Clerjon, Jean-Louis Damez, Cyril Chevarin, Stéphane Portanguen, Alain Kondjoyan and Jean-Marie Bonny*

UR370 Qualité des Produits Animaux, INRA, F-63122 Saint-Genès-Champanelle

Phone: +33-4- 73-62-41-52.

Fax: +33-4-73-62-40-89

E-mail: jean-marie.bonny@clermont.inra.fr

1.1 ABSTRACT

Understanding and controlling structural and physical changes in meat during cooking is of prime importance. Nuclear magnetic resonance imaging (MRI) is a non-invasive, non-destructive tool that can be used to characterize certain properties and structures both locally and dynamically. Here we show the possibilities offered by MRI for the *in situ* dynamic imaging of the connective network during the cooking of meat to monitor deformations between 20 °C and 75 °C. A novel device was used to heat the sample in a MR imager. An MRI sequence was developed to contrast the connective tissue and the muscle fibers during heating. The temperature distribution in the sample was numerically simulated to link structural modifications and water transfer to temperature values. The contraction of myofibrillar and collagen networks was observed at 42 °C and water began to migrate towards the interfascicular space at 40 °C. These observations are consistent with literature results obtained using destructive and/or non-localized methods. This new approach allows the simultaneous monitoring of local deformation and water transfer, changes in muscle structure and thermal history.

KEYWORDS: heating, deformation, water transfer, meat, MRI, thermal simulation

1.2 INTRODUCTION

Knowledge of the structural changes that occur during food processing, e.g. cooking, is of prime importance for the control of sensory, nutritional and technological qualities of end products. The cooking of meat results in a loss of 20-40% of its mass, due to expulsion of juice (containing water, lipids and micronutrients) from the meat (1, 2). For the consumer, loss of juice can be detrimental to sensory qualities. For example, it has been demonstrated that juice loss is inversely correlated with the juiciness of the cooked product (3). It also adversely affects nutritional quality through the loss of fatty acids and micronutrients (vitamins, minerals and amino acids) that are essential for human health (4). In addition to quality issues, industrial operators have to be very attentive to production costs, which are directly linked to cooking yield, and so to juice loss.

The structural changes that occur in meat during cooking are caused by modifications to both cell proteins and connective tissue proteins. Observations made by several authors (5-8) consistently emphasize that meat toughness – evaluated by shear stress measurements – evolves during cooking in three well-identified phases: (i) from about 40 °C to 50 °C toughness increases, (ii) from about 50 °C to 60 °C, toughness decreases, and (iii) from about 60 °C to 80 °C, toughness increases again. However, the explanation for these variations in toughness resulting from structural changes at different scales is controversial. The first phase has been attributed to the thermal contraction of the perimysial connective tissue (7, 8), while beyond 60 °C, increased toughness was ascribed to the denaturing of myofibrillar proteins. A different explanation (5) is that the low temperature modifications during the first phase result from the denaturing of cell proteins.

On our view the elucidation of these mechanisms is made difficult primarily by two experimental limitations: (i) inability to observe changes in muscle structure (especially deformations) and internal water transfer simultaneously and locally during cooking and (ii) approximations in the thermal analysis: temperature is often considered to remain the same throughout the sample, which would be true only at steady-state, and never true for variable temperature regimes, the more so for larger sample sizes. The false assumption of even temperature leads us to attribute differences in contraction due to a temperature gradient to structural heterogeneities instead. However, the experimental alternative of waiting for thermal equilibrium to be reached leads us to neglect the irreversible structural modifications that occur during the transition to temperature homogeneity.

Several biophysical methods can be used to characterize meat structure (9). Some of these methods are applicable to the monitoring of cooking and have demonstrated the denaturation and precipitation of myosin (2, 10, 11), the denaturation and contraction of collagen (12) and the denaturation of other sarcoplasmic and myofibrillar proteins (13) in the course of heating. The mechanisms governing water loss have been studied mainly on raw meat (14-17), and less often on meat during heating (18-20).

Multi-exponential analysis of water T_2 relaxation decay curves obtained by low-field NMR showed a loss of the major water population during heating (5). This was due to the thermal denaturation of proteins, in particular actin and myosin, which modifies their structure and ultimately diminishes the amplitude of the most mobile component. This decrease is mainly attributable first to the transverse contraction of fibres and bundles, and then to the contraction of the connective tissue, which causes expulsion of water towards the sample surface. These results are difficult to interpret in the absence of information on the spatial localization of these populations. The only reported MRI study (18) conducted during heating in meat measured some intrinsic NMR parameters locally (T_1, T_2 and proton density). It showed a loss of water associated with a decreased rotational mobility, and spatial differences between the core and outer layers of the sample.

The aim of our work was first to develop an *in situ* method to map temperature and deformation of meat simultaneously in the course of a variable temperature regime. Our second objective was to interpret these deformation and water transfer over a broad temperature range (20-75 °C), based on the structural modifications reported in the literature.

To this end, MRI was coupled with numerical simulations of heat transfer to map local temperature. In this paper, we present (i) the experimental laboratory set-up used to heat the sample in the magnetic environment, (ii) the techniques used for the simulation of heat transfer, (iii) the specific MRI developments carried out and (iv) a short analysis of the first results obtained.

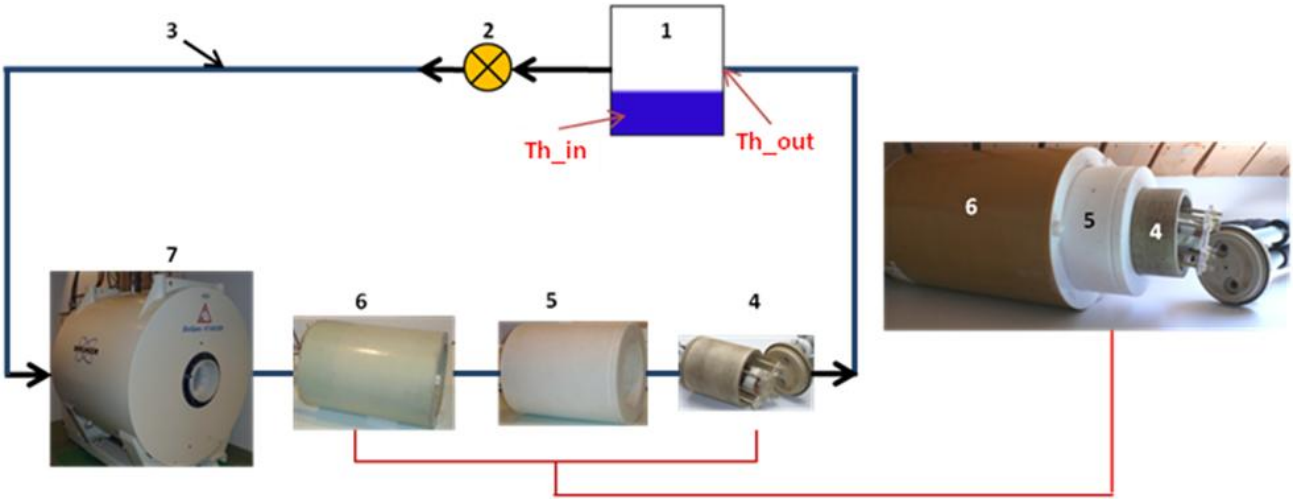

Figure 1: Overview and photo of subassemblies.

For the overview: (1) Holding tank and heating element for circulating water, (2) Pump, (3) Silicone tubing, diameter 10 mm, (4) Non-magnetic sample holder cell, (5) Teflon thermal insulation, (6) ^{1}H NMR coil and (7) High-field NMR imager.

For the photo: (4) Non-magnetic sample holder cell, (5) Teflon thermal insulation, (6) ^{1}H NMR coil.

1.3 MATERIALS AND METHODS

1.3.1 Samples

The muscle type used was the *biceps femoris* (BF) from Charolais heifers (4 years old), in which the connective tissue is rich in elastin. Samples were cut in the form of cylinders 5 cm in diameter by 6 cm long with the muscle fibres oriented axially. The dimensions of the sample were chosen to obtain an adequate picture of the perimysial structure of the muscle and still fit the dimensions of the MR imager. The meat cylinders were then placed in plastic bags in a vacuum to prevent direct contact with the circulating heating water.

1.3.2 Heating device

A novel device was designed to acquire NMR images from a meat sample being heated over the temperature range 20-75 °C. The set-up was designed to meet the following specifications: (i) provide exchange conditions at the sample surface that were as homogeneous as possible, (ii) not introduce any materials that could disturb the static magnetic field in the sample, (iii) insulate the device thermally from the radiofrequency (RF) coil to protect it from damage or loss of performance and (iv) provide a heating regime compatible with the MRI acquisition rate.

Heating via a fluid was preferred as it would ensure more homogeneous exchange conditions at the sample surface. Among different candidate heat exchange fluids, water was chosen for its simplicity of use, in particular when draining out and cleaning the circuit.

The system comprised a watertight, non-magnetic sample holder cell made of polyetheretherketone (PEEK) (4, Fig.1), placed inside a sleeve made of Teflon (5, Fig.1), also a non-magnetic material, which provided thermal insulation between the cell and the RF coil. The assembly was placed at the centre of the RF coil (6, Fig.1), which was in turn positioned inside the MR imager (7, Fig.1).

The sample was heated in its cell by water sent round a circuit (3, Fig.1) by a pump (flow rate = 13 l/min) (2, Fig.1). The circulating water was heated in a holding tank (1, Fig.1) by a temperature-regulated resistance heater. The regulation system was programmed so that the temperature of the water rose evenly from 20 °C to 75 °C at a climb rate of 0.88 °C/min, imposed by the time resolution of the MRI methods used.

The adiabaticity of the heating system, which was ensured by the choice of materials and the water flow-rate, was checked by placing two thermocouples in the circuit at the inlet to (Th_in) and outlet from the holding tank (Th_out). The temperatures at the two measurement points remained the same throughout the temperature program.

1.3.3 Spatiotemporal simulation of the temperature

In each experimental run the circulating water heated, by forced convection, the surface of the vacuum-sealed plastic bag containing the meat sample, which in turn was heated by conduction from its surface through to its core. The heated sample gradually shrank, juice expelled from the sample was collected between the meat surface and the inner wall of the bag. As the decrease in volume of the sample was equal to the quantity of juice expelled, the total volume of the bag remained the same throughout the heat treatment. Preliminary calculations showed that (i) heat transfer due to the migration of juice from the core of the sample to its surface was negligible in comparison with heat exchange by conduction and (ii) heat transfer by free convection within the expelled juice was also negligible. The heat exchange in the juice and the meat were thus considered for present purposes as purely conductive. The heat exchange flux at the inner surface of the bag was described by Newton's law. The transfer coefficient was determined from independent experiments taking into account the rate of circulation of the heating fluid, literature data (21) and measurements made to determine the thermal resistivity of the bag. The value of the coefficient retained was 430 $Wm^{-2}K^{-1}$ over the circumference of the meat cylinder and 31 $Wm^{-2}K^{-1}$ at the two ends in contact with the polycarbonate. Three-dimensional simulations were carried out assuming the thermophysical properties of the meat were: thermal conductivity λ= 0.45 W $m^{-1}K^{-1}$, density ρ = 1060 kgm^{-3} and specific heat capacity C_p = 3200 $Jkg^{-1}K^{-1}$.

Thermal conductivity of meat is known to vary with fat content, water concentration and temperature (22). Increasing temperature tends to increases the thermal conductivity while it is decreased by an increasing fat content. When lean meat is cooked between 40 °C-75 °C, the range of variation of thermal conductivity λ, is limited to 0.45-0.52 $Wm^{-1}K^{-1}$. Increasing fat content from 2.5% to 5.6% leads to the same range of values in cooked meat (22). Effect of λ variations on our simulated temperatures was less than 1.0 °C. However to ensure more accurate results, thermal conductivity was measured by us on samples cooked at different temperatures using a transient method close to Fitch method but adapted to solid samples (23). It was assumed that the thermal capacity of the meat was constant and equal to 3200

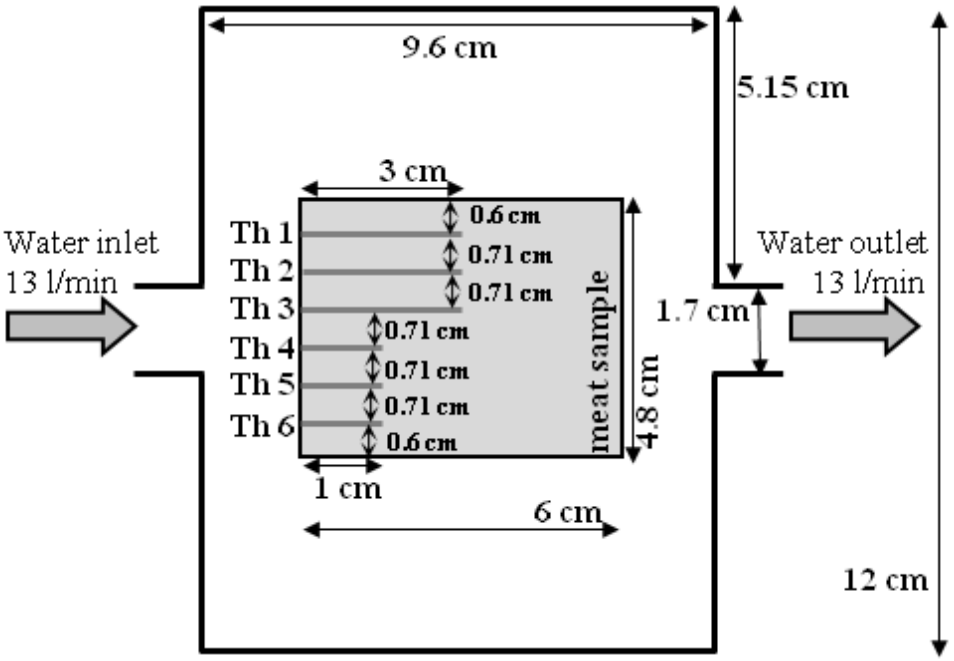

Figure 2: Practical arrangement of the thermocouples (top view).

J kg K^{-1} (24). These measurements showed that thermal conductivity remained about constant during cooking, at a value close to 0.45 $Wm^{-1}K^{-1}$. This corroborates previous results on the acuity of this value when used to model beef temperatures during cooking without surface crusting (25).

Calculated results showed that the exchanges at the cylinder ends did not influence the values of temperature in the central section of the cylinder. In this part of the sample, more precise simulations were then carried out in two dimensions, assigning different thermophysical properties to the juice and to the meat, and performing the calculation stepwise to be able to differentiate the regions occupied respectively by the meat after shrinkage and by the expelled juice. The thermophysical properties of the juice were those of water; i.e. λ = 0.60 W m^{-1} K^{-1}, ρ = 998 kg m^{-3} and C_p = 4180 J kg^{-1} K^{-1} at 20 °C, and λ = 0.67 $Wm^{-1}K^{-1}$, ρ = 971 kg m^{-3} and C_p = 4190 J $kg^{-1}K^{-1}$ at 80 °C. The juice-meat interface was determined by manual segmentation from NMR images (cf. Estimation of overall deformation part), the successive steps of this process being defined so that the decrease in surface area between two successive steps was limited to 5%. The numerical simulations were carried out by finite elements using the Comsol Multiphysics® 3.4 software.

These simulations were validated experimentally by placing temperature probes in the set-up and in the same type muscle sample and carrying out cooking cycles outside the imager but in similar conditions. The locations of these probes in the sample are shown in Figure 2.

1.3.4 High-field MRI

Image acquisition was carried out using a Biospec horizontal 4.7 tesla MRI system (Bruker GmbH, Ettlingen, Germany), of rated diameter 26 cm, equipped with a BGA-26 rapid gradient system (maximum amplitude 50 $mT.m^{-1}$, rise time 260 µs). The main fiber axis in the sample was placed approximately parallel to the main direction of the static magnetic field B_0 of the magnet.

The susceptibility-weighted images (TE = 15 ms, TR = 2000 ms) were acquired continuously in an axial plane using a steady-state free precession (SSFP or FLASH) sequence with a single echo. By exploiting the difference in magnetic susceptibility between (i) elastin and the lipids of the connective network and (ii) the muscle fibres (26), the images highlighted the elastin- and lipid-rich connective tissue (hyposignal). The points of this network were used as internal fiduciary markers to capture the deformation of the muscle during heating. This

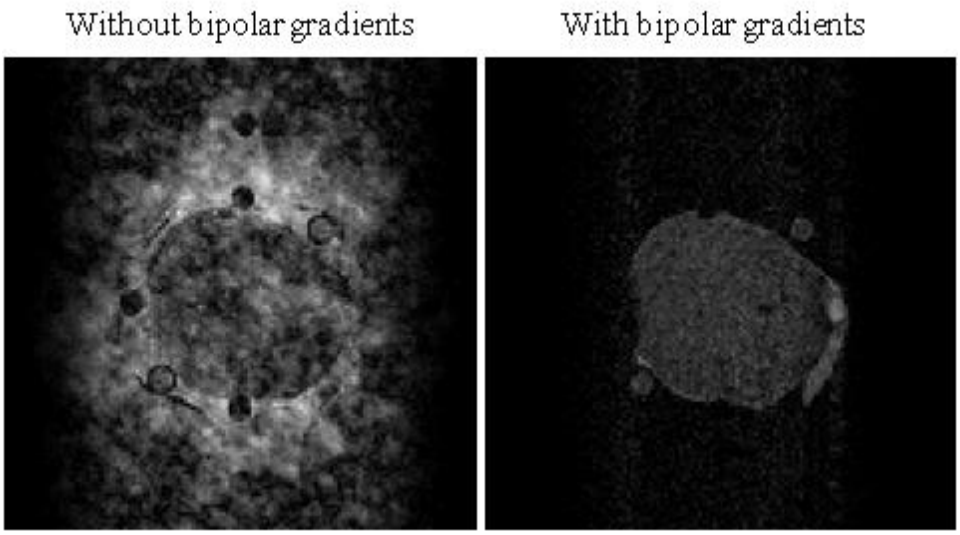

Figure 3: NMR images, obtained with an enlarged FOV (128 × 128 mm²) circumscribing the entire sample holder device, without and with the bipolar saturation gradient. The bipolar saturation gradients almost extinguish the mobile proton signal.

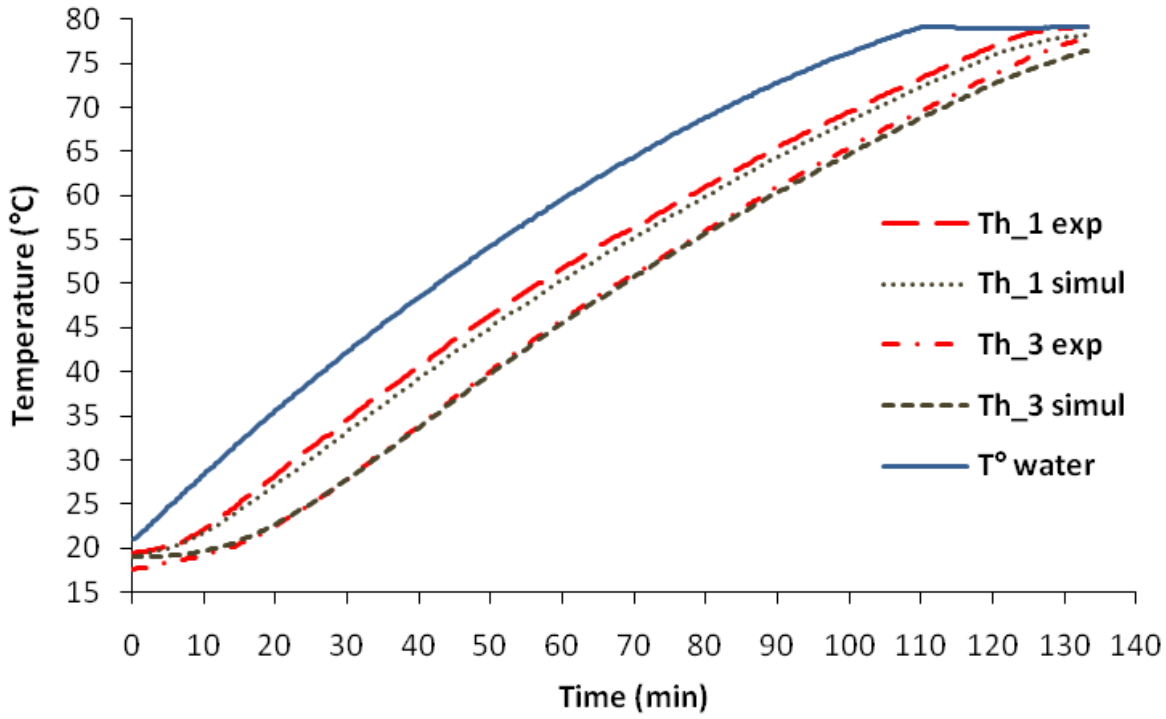

Figure 4: Simulated and representative experimental temperature time course of thermocouples Th_1 and Th_3 shown in figure 2. This figure demonstrates the good agreement between simulated and experimentally measured temperatures, near the surface and close to the centre of the sample.

sequence was run with bipolar gradients (time between gradients Δ = 5.52 ms, gradient duration δ = 5.2 ms) to cancel the signal of the mobile protons in the heating water. The extinction of this signal eliminated the movement artifacts that degrade the image. Figure 3 shows how bipolar saturation gradients extinguish these artifacts. The field of view (FOV) could then be reduced to a square region circumscribed on the sample, thereby improving the time resolution for a given spatial resolution.

A complete experiment consisted in a series of 20 acquisitions each of 14 sections. All the sections were obtained with a FOV of 64 × 64 mm², a matrix of 128 × 128 pixels and a thickness of 2 mm. The volume of the resulting voxel was therefore 0.5 × 0.5 × 2 mm^3. The time resolution was 4 min 16 s. An acquisition was made at each temperature step (every 10 °C) and during each temperature rise from one temperature step to the next. Experiments have been repeated on four BF samples coming from two different animals.

The transmit and receive RF coil used was a linear birdcage. The adjustment of the resonance frequency and impedance at that frequency of the RF coil under load (i.e. tuning/matching) was carried out only at the start of the experiment at 20 °C. These parameters were not reset in the course of the experiment.

1.3.5 Estimation of overall deformation

The muscle was segmented manually on the images of the central section obtained at different temperatures, using the Matlab® R2008b software. In this way it was possible to measure the surface area as a function of temperature, and so follow the time course of the overall muscle deformation. This overall measurement complemented the monitoring of the internal markers from the connective tissue, which describe the local deformation.

1.4 RESULTS AND DISCUSSION

1.4.1 Spatiotemporal simulation of temperature

The measurements made in the circulating water showed that the temperature of the water was homogeneous in the measurement cell where the sample was treated. Figure 4 compares the simulated and measured temperature time courses, near the sample's surface (Th_1) and near the sample's centre (Th_3) while the cooking temperature was ramped from 20 °C to 80 °C followed by a brief plateau at a constant temperature of 80 °C. The temperature ramp was

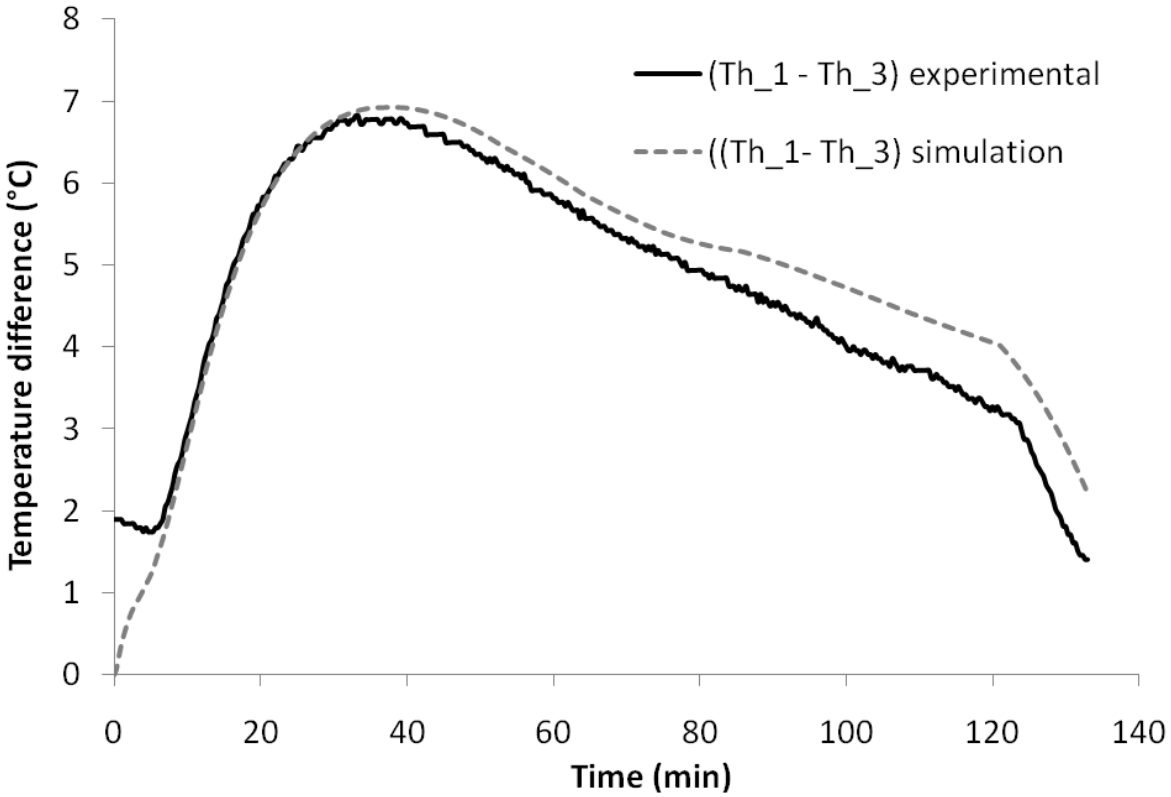

Figure 5: Representative experimental and simulated time course of the temperature difference between thermocouples Th_1 and Th_3 shown in Figure 2, placed 14.2 mm apart at the start of the experiment.

introduced as a boundary condition for the heat calculation. The results showed a very close agreement between the simulated and experimental data. The differences recorded at t = 0 were due to small difference in initial temperature inside the sample. These initial differences evened out in the first minutes of heating and were then slight; on average 0.5 °C for the thermocouple located at the sample core and 1.1 °C for the one located nearer the surface. This discrepancy was not constant and tended to increase in the course of the experiment as the sample shrank. It was 0.2 °C and 0.8 °C respectively at the centre and near the surface of the sample after 33 minutes of treatment, and then increased to reach 1.2 °C at the end of the treatment. These discrepancies can be explained (i) by errors in the initial positioning of the thermocouple, which were greater at the surface than at the centre of the sample, and (ii) by a shift of the probe relative to the meat surface due to the shrinking of the sample. The shift of the thermocouple, which is brought closer to the sample surface, is not taken into account in the model.

Figure 5 shows the simulated and experimental time course of the temperature difference between the above two measurement points, which were ~14 mm apart at the start of the experiment. The temperature gradient increased during the first 37 minutes of treatment, reaching a peak at about 7 °C, and then decreased. This change in the temperature gradient was due to thermal inertia and the slowing of the heating ramp. After 37 minutes of treatment the experimental gradient decreased regularly as the temperature in the sample gradually evened out and the two thermocouples were brought closer together by the shrinking of the meat cylinder. A sudden drop in the gradient was observed at the end of the experiment when the circulating water reached its plateau at 80 °C. The simulated gradient fitted the experimental gradient time course perfectly for the first 37 minutes of treatment and tended to overestimate it slightly thereafter. This was due to the thermocouples drawing together as the sample shrank, which was not taken into account in the model.

The numerical simulation yielded a map of the temperature at each time of the experiment, with a maximum error of between 0.5 °C and 1 °C. Each part of the moving structure could thus be associated with a precise time-temperature regime. The approach by temperature simulation is thus much more rigorous than considering the temperature to be uniform throughout the treatment and equal to the temperature at the sample core. An averaging approach of this type entails ignoring local temperature discrepancies of up to 7 °C. The approach by simulation thus allows a better discrimination between differences in

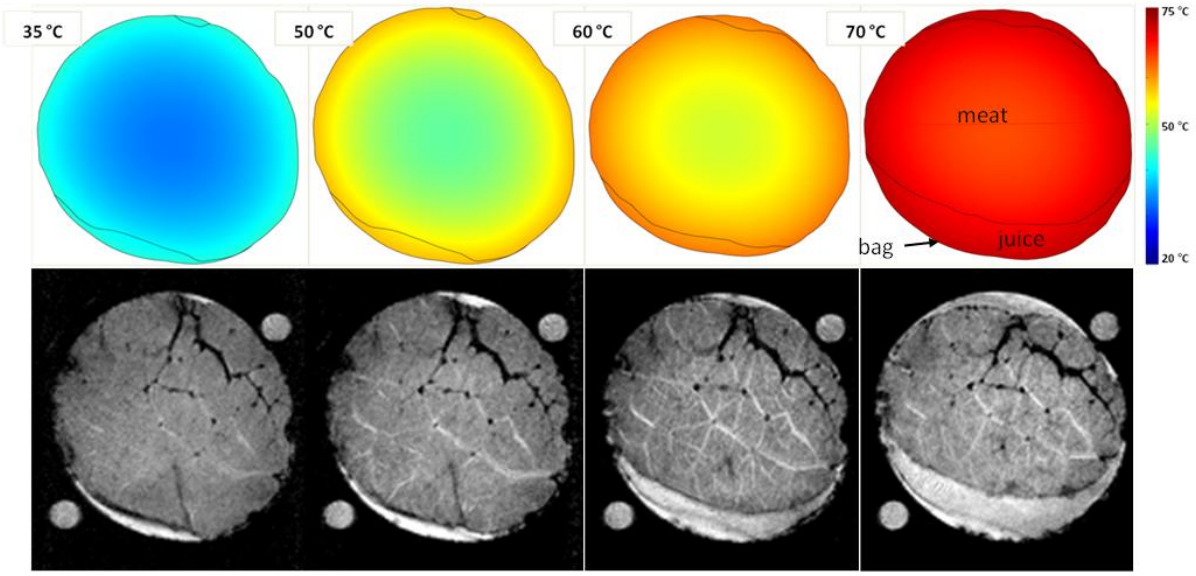

Figure 6: Temperatures mapped from our simulation, in the central section of the sample, for 4 average temperatures (35°C, 50°C, 60°C and 70°C) and the corresponding NMR images. Transfer coefficients are here considered as the same in meat and juice.

deformation and water transport linked to the structure and differences due to locally uneven temperatures.

Temperatures mapped from our simulation, in the central section of the sample, for four average temperatures (35 °C, 50 °C, 60 °C and 70 °C) and the corresponding NMR images are shown in Figure 6. In accordance with the heating process, we can see temperature gradient from the sample centre to boundaries. NMR images underscore meat deformation and induced water transfers. Figure 6 shows the correspondence between temperature maps and NMR images; interpretation of meat deformation and induced water transfer in regards to local temperature is done in Monitoring of deformations and mass transfer part.

A recent paper presents a similar computational modeling for mapping heating patterns in a food analog (27). Like in this study, it would have been possible to achieve a similar MR thermometry method to map temperature difference, but we have demonstrated here that our invasive and direct approach is enough for validation.

1.4.2 Imaging connective tissue during heating

During heating, the mean signal-to-noise ratio (SNRm) averaged over the different slices fell from 21 at 20 °C to 10 at 75 °C, i.e. a loss of about 55%. This degradation of the SNRm was tolerable for the exploitation of the NMR images.

This SNRm degradation can be explained by the combined changes in two categories of parameters, respectively extrinsic (instrument drifts) and intrinsic (changes in NMR properties of the sample):

- The tuning/matching setting of the coil-sample system drifted during heating because of changes in the geometry and dielectric properties of the sample. The impedance of the system at the resonance frequency (Larmor frequency for ^{1}H excitation) was not correct, causing a degradation of SNRm of about 15%.
- The changes in the intrinsic parameters of the sample (T_1, T_2, proton density PD and chemical shift δ) with temperature showed an increase in T_1, a decrease in T_2 and PD, and a change in δ. The increase in T_1 observed was due to the decrease in the correlation time τ_c of the dipole-dipole interactions due to the temperature (28). The decrease in T_2 can be explained by a stronger interaction between water and macromolecules due to the decrease in PD caused by the expulsion of juice from the sample. The change in δ of 0.014 ppm/°C is consistent with

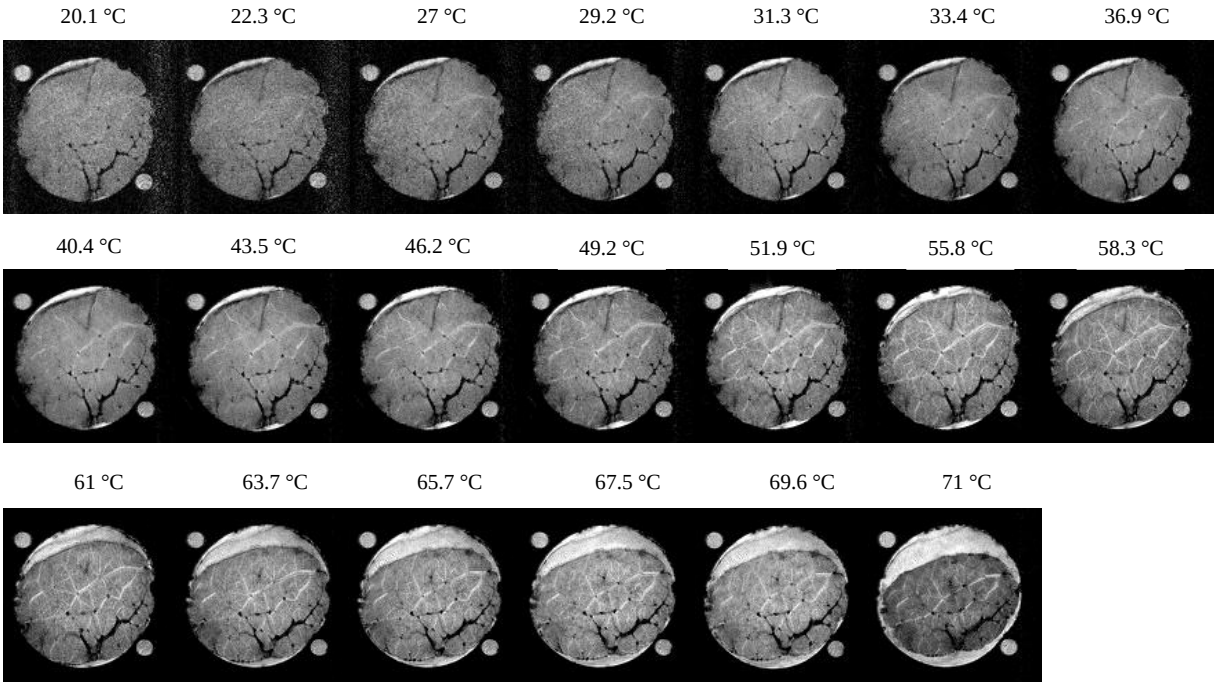

Figure 7: NMR images of the deformation in the central section of the sample. The grey scale windowing has been adjusted to compensate for degraded SNR. The values displayed are means of simulated temperatures in this central section.

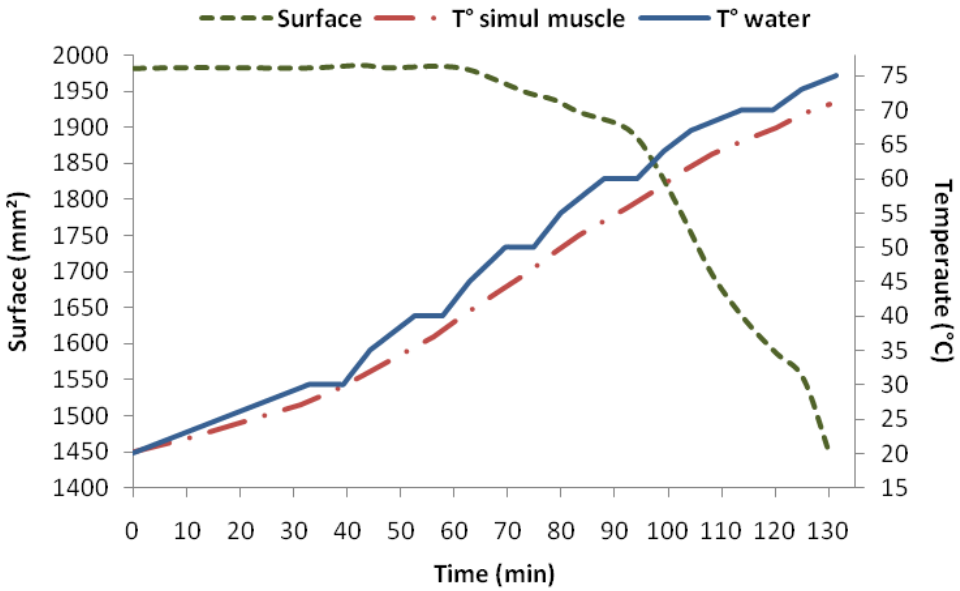

Figure 8: Curves showing the time course of the surface area of the central section of a representative muscle, the set temperature (heating water) and the simulated average temperature of the muscle.

the literature (29). The dependence of δ on temperature has been ascribed to the effects of breaking, stretching and/or bending of hydrogen bonds (29) with temperature.

The noise growth that degrades the SNRm was due to the thermal agitation of the charges in the RF coil and in the volume it covered. In the case of a volume coil (such as one with a birdcage geometry), it collects all the noise from its volume (30, 31). In our case, the noise came from the whole cell and outweighed that of the coil. The variance of thermal noise intensity is proportional to the temperature.

Finally, those intrinsic losses of SNRm linked to the changes in the NMR parameters of the sample and its thermal noise represented about 40%.

1.4.3 Monitoring of deformations and mass transfer

Figure 7 shows the images of deformation obtained at the centre of the sample for simulated average temperatures in the range 20.1–71 °C. The curves in Figure 8 represent the time course of the surface area of the central section of the muscle measured from NMR images, the average temperature of the muscle in this section obtained by simulation and the temperature of the circulating water.

The curve of the deformation time course (Fig.8) shows two points of inflection: the first, at 64 min of heating, corresponds to the beginning of the deformation of the sample at the average temperature of the muscle of 42 °C (set temperature 48 °C); the second, at 93 min, marks an acceleration of the deformation at an average temperature of the muscle of 56 °C (set temperature 60 °C). The surface area of the central section of the muscle thus shrank by 27% between 20 °C and 75 °C.

The deformation images (Fig.7) reveal a network of exuded water between the bundles of fibres derived from the migration of intracellular water. This water is characterized by a higher value of T_2 (free water) shown by a hypersignal on the susceptibility-weighted image. This exudation started from the average muscle temperature of 40 °C (set temperature 45 °C). Like the connective network, these channels can serve as internal markers to describe deformation fields.

The average deformations and expulsions of water observed in this study in the whole of the sample are consistent with the results reported in the literature, in particular: (i) the onset of deformation observed at 42 °C, which corresponds to initial denaturing of myosin (10, 11, 14)

deformation at 55 °C due to the contraction and denaturing of collagen, which causes the expulsion of meat juice (12- 14, 33, 34).

The channels of migrated water between the fibre bundles (Fig.7) started to appear at 40 °C, corresponding to the temperature of the start of myosin denaturation (35). This causes a loss of water from myofibres, which migrates and collects in the intermyofibrillar space (14, 36). The transport of water appeared more clearly from 52 °C, probably owing to the contraction of the connective network, which caused an expulsion of water first into the interfascicular space and then out of the meat. The contraction of the meat was anisotropic, and resulted in a cylinder of elliptic cross section.

The effects of temperature on global deformation and on water transfer described here have been reproducibly observed on four different sample of the same muscle type (BF). Thanks to the spatial information provided by our imaging methodology, to intra-muscle structural variability (e.g. size of fascicles) and to differences of temperature regime inside the sample, a single experiment provides itself extensive information for modeling relationship between temperature and deformation. However, both inter-animal variation and muscle type are likely to have important effects, which deserve further studies on different muscle types, coming from different animals, but which are out of the objectives of this paper.

We intend to develop processing methods to obtain local deformation fields using internal markers for association with simulated temperature mapping. This will help us gain a better understanding of the roles played by the different parts of the structure that appear in the image on deformation and fluid transfer. Further work in progress will also seek to improve the time resolution using rapid image encoding methods, and measure the quantity of water and its mobility locally by reconstructing parametric maps of the ^{1}H nucleus. This new knowledge will allow a better understanding of changes in sensorial and nutritional qualities of meat during cooking.

1.5 CITED REFERENCES IN ARTICLE 1

1. Bircan, C., & Barringer, S. A. Determination of protein denaturation of muscle foods using the dielectric properties. Journal of Food Science 2002, 67(1), 202-205.

2. Bertram, H. C., Engelsen, S. B., Busk, H., Karlsson, A. H., & Andersen, H. J. Water properties during cooking of pork studied by low-field NMR relaxation: effects of curing and the RN--gene. Meat Science 2004, 66, 437-446.

3. Chambaz, A., Scheeder, M. R. L., Kreuzer, M., & Dufey, P.-A. Meat quality of Angus, Simmental, Charolais and Limousin steers compared at the same intramuscular fat content. Meat Science 2003, 63, 491-500.

4. Biesalski, H. K. Meat as a component of a healthy diet - are there any risks or benefits if meat is avoided in the diet? Meat Science 2005, 70, 509-524.

5. Tornberg, E. Effects of heat on meat proteins - Implications on structure and quality of meat products. Meat Science 2005, 70, 493-508.

6. Combes, S., Lepetit, J., Darche, B., & Lebas, F. Effect of cooking temperature and cooking time on Warner-Bratzler tenderness measurement and collagen content in rabbit meat. Meat Science 2004, 66, 91-96.

7. Christensen, M., Purslow, P. P., & Larsen, L. M The effect of cooking temperature on mechanical properties of whole meat, single muscle fibres and perimysial connective tissue. Meat Science 2000, 55, 301-307.

8. Bouton, P. E., & Harris, P. V. Changes in the Tenderness of Meat Cooked at 50-65-Degrees-C. Journal of Food Science 1981, 46(2), 475-478.

9. Damez, J. L., & Clerjon, S. Meat quality assessment using biophysical methods related to meat structure. Meat Science 2008, 80, 132-149.

10. Martens, H., Stabursvik, E., & Martens, M. Texture and colour changes in meat during cooking related to thermal denaturation of muscle proteins. Journal of Texture Studies 1982, 13, 291-309.

11. Micklander, E., Peshlov, B., Purslow, P. P., & Engelsen, S. B. NMR-cooking: monitoring the changes in meat during cooking by low-field H^1 NMR. Trends in Food Science & Technology 2002, 13, 341-346.

12. Stabursvik, E., & Martens, H. Thermal-Denaturation of Proteins in Post-Rigor Muscle-Tissue As Studied by Differential Scanning Calorimetry. Journal of the Science of Food and Agriculture 1980, 31, 1034-1042.

13. Wright, D. J., Leach, I. B., & Wilding, P. Differential Scanning Calorimetric Studies of Muscle and Its Constituent Proteins. Journal of the Science of Food and Agriculture 1977, 28, 557-564.

14. Bertram, H. C., Whittaker, A. K., Andersen, H. J., & Karlsson, A. H. Visualization of drip channels in meat using NMR microimaging. Meat Science 2004, 68, 667-670.

15. Bertram, H. C., Karlsson, A. H., Rasmussen, M., Pedersen, O. D., Donstrup, S., & Andersen, H. J. Origin of multiexponential T_2 relaxation in muscle myowater. Journal of Agricultural and Food Chemistry 2001, 49, 3092-3100.

16. Bertram, H. C., Purslow, P. P., & Andersen, H. J. Relationship between meat structure, water mobility, and distribution: A low-field nuclear magnetic resonance study. Journal of Agricultural and Food Chemistry 2002, 50, 824-829.

17. Renou, J. P., Foucat, L., & Bonny, J. M. Magnetic resonance imaging studies of water interactions in meat. Food Chemistry 2003, 82, 35-39.

18. Shaarani, S. M., Nott, K. P., & Hall, L. D. Combination of NMR and MRI quantitation of structure and structure changes for convection cooking of fresh chicken meat. Meat Science 2006, 72, 398-403.

19. Wahlby, U., & Skjoldebrand, C. NIR-measurements of moisture changes in foods. Journal of Food Engineering 2001, 47, 303-312.

20. Van der Sman, R. G. M. Moisture transport during cooking of meat: An analysis based on Flory-Rehner theory. Meat Science 2007, 76, 730-738.

21. Churchill, S. W., & Bernstein, M. Correlating Equation for Forced-Convection from Gases and Liquids to A Circular-Cylinder in Cross-Flow. Journal of Heat Transfer-Transactions of the Asme 1977, 99(2), 300-306.

22. Rahman, S. Food properties handbook, CRC Press, Boca Raton (Florida, USA) 1995, chapter 5, 301-302.

23. Mohsenin, N.N. Thermal properties of foods and agricultural materials. New York: Gordon and Breach 1980, chapter 3.

24. Tsai, S. J., Unklesbay, N., Unklesbay, K., & Clarke, A. Thermal properties of restructured beef products at different isothermal temperatures. Journal of Food Science 1998, 63, 481-484.

25. Baghe-Khandan, M. S., & Okos, M. R. Effect of cooking on the thermal conductivity of whole and ground lean beef. Journal of Food Science 1981, 46, 1302-1305.

26. Bonny, J. M., Laurent, W., Labas, R., Taylor, R., Berge, P., & Renou, J. P. Magnetic resonance imaging of connective tissue: a non-destructive method for characterising muscle structure. Journal of the Science of Food and Agriculture 2001, 81, 337-341.

27. Rakesh, V., Seo, Y., Datta, A.K., McCarthy K.L., & McCarthy M.J. Heat transfer during microwave combination heating: computational modeling and MRI experiments. AIChE 2010, 56, 2468-2478.

28. Farrar, T. C., & Jablonsky, M. J. NMR Relaxation Study of Na2Pfo3 in Solution - Chemical-Shift Anisotropies, Bond Distances, J-Coupling Constants, and Correlation Times. Journal of Physical Chemistry 1991, 95, 9159-9166.

29. Hindman, J. C. Proton Resonance Shift of Water in the Gas and Liquid States. The Journal of Chemical Physics 1966, 44, 4582-4592.

30. Hoult, D. I., & Lauterbur, P. C. The Sensitivity of the Zeugmatographic Experiment Involving Human Samples. Journal of Magnetic Resonance 1979, 34, 425-433.

31. Darrasse, L., & Ginefri, J. C. Perspectives with cryogenic RF probes in biomedical MRI. Biochimie 2003, 85, 915-937.

32. Bendall, J. R., & Restall, D. J. The cooking of single myofibres, small myofibre bundles and muscle strips from beef M. Psoas and M. Sternomandibularis muscles at varying heating rates and temperatures. Meat Science 1983, 8, 93-117.

33. Lepetit, J. Collagen contribution to meat toughness: Theoretical aspects. Meat Science 2008, 80, 960-967.

34. Palka, K., & Daun, H. Changes in texture, cooking losses, and myofibrillar structure of bovine M-semitendinosus during heating. Meat Science 1999, 51, 237-243.

35. Davey, C. L., & Gilbert, K. V. Temperature-dependent cooking toughness in beef. Journal of the Science of Food and Agriculture 1974, 25, 931-938.

36. Bonny, J. M., & Renou, J. P. Water diffusion features as indicators of muscle structure *ex-vivo*. Magnetic Resonance Imaging 2002, 20, 395-400.

2. Article 2 : Cartographie des champs de déformation du muscle pendant le chauffage : IRM dynamique *in situ* et recalage non-linéaire.

Le travail précédent a validé notre démarche expérimentale pour suivre *in situ* la déformation globale du muscle durant un procédé thermique au moyen d'un dispositif de chauffage adapté et de l'imagerie pondérée en susceptibilité pour révéler la déformation de la structure musculaire.

L'objectif de ce second article est de présenter les méthodes permettant de cartographier les champs de déformation dans le muscle pendant le chauffage à partir d'images RMN.

Les images acquises exploitent la différence de susceptibilité magnétique entre élastine et lipides du réseau conjonctif d'une part et des fibres musculaires d'autre part (Bonny 2001) et mettent donc en évidence le réseau conjonctif riche en élastine et en lipides. Le principe a été de suivre le déplacement de ces marqueurs internes pendant la contraction du muscle, afin d'établir *in fine* les champs de déformation.

Nous avons constaté une décroissance progressive du rapport signal sur bruit des images au cours de l'expérimentation, ce qui s'avère critique pour le calcul des champs de déformation à partir de ces images. Des expériences ont donc été menées pour comprendre les multiples déterminants de la perte du signal au cours du chauffage, en précisant notamment les parts respectives des dérives instrumentales et de l'évolution des propriétés physico-chimiques intrinsèques au muscle pendant la cuisson.

La reconstruction des champs de déformation repose sur le recalage de deux images acquises successivement. Il consiste à trouver la transformation géométrique qui optimise la mise en correspondance de deux images. Parce que les transformations non-linéaires prennent en compte la déformation des objets au contraire des linéaires et que le chauffage provoque la déformation de l'échantillon, des transformations non-linéaires de complexité croissante ont été comparées pour déterminer la transformation la plus appropriée à nos images.

Les résultats montrent qu'il est possible d'appairer le réseau conjonctif de deux images IRM acquises successivement, au cours de la cuisson. Les matrices de transformation servent ensuite à établir les champs de déformation. Les premiers modèles reliant précisément

déformation et température ont été obtenus décrivant deux phases bien distinctes de la déformation et le transfert d'eau qui en découle.

Ce travail a été publié en 2011 dans *Magnetic Resonance Imaging* (Bouhrara 2011b).

Mapping of muscle deformation during heating: *in situ* dynamic MRI and non-linear registration

Mustapha BOUHRARA, Benoist LEHALLIER, Sylvie CLERJON, Jean-Louis DAMEZ and Jean-Marie BONNY*.

UR370 Qualité des Produits Animaux, INRA, F-63122 Saint-Genès-Champanelle

Phone: +33-4- 73-62-41-52.

Fax: +33-4-73-62-40-89

E-mail: jean-marie.bonny@clermont.inra.fr

2.1 ABSTRACT

We present developments in dynamic MRI that allow internal structural muscle markers to be followed during heating. This monitoring is based on quantitative characterization of the experimental conditions and their temperature time course. A non-linear image registration technique was optimized and applied to consecutively acquired images to measure the deformation fields in the muscle. A model coupling local deformation and temperature was obtained, which for the first time takes into account the variations of deformation and temperature in the sample. This modeling opens the way to a better understanding of the mechanisms responsible for mass loss and degradation of the textural properties of muscle during heating.

KEYWORDS: Dynamic MRI, deformation fields, muscle, meat, heating, temperature, non-linear registration.

2.2 INTRODUCTION

Agrofood products, particularly meat, are most often consumed cooked. Predicting the effects cooking has on the sensory, nutritional and technological qualities of the consumed product is of major importance for both the consumer and the meat industry. To date, there is no reliable model linking the deformation of the muscle with the heating profile applied to it. However, such a model is necessary for the simultaneous control of mass loss and degradation of the textural properties of cooked food. Analysis of the coupling between deformation and temperature is affected by (i) the deformation measurement methods, which are mostly nonlocal and (or) destructive (1), and (ii) the assumption of a homogeneous temperature inside the sample (2). To build more precise models, i.e. that take account of the variations of deformation and temperature in the sample, it is clearly advisable to measure deformation and temperature simultaneously and at the same location.

Imaging in general and MRI in particular, will highlight structural meat markers at a mesoscopic scale (3-6). In recent work (7) we showed the feasibility of *in situ* MRI of muscle during a thermal process by cancelling signal of circulating heating water using a bipolar gradient in the three directions. This cancelation allows reducing field of view (FOV) and then improving spatial resolution. We also showed that T_2^*-weighted MR images sustained a sufficient contrast between internal markers of the connective network and muscle fibers throughout the temperature range (20–75 °C). These recent results have paved the way for the two main objectives of the present manuscript. The first is to estimate deformation fields by monitoring of the displacement of these fiducial markers inside images of muscle during heating. The second is to interpret the mechanisms underlying muscle contraction on the basis of the relationship between temperature and deformation.

This paper is organized as follows. The first subsection presents our experimental procedure. The next sub-sections describe in detail the approach for optimizing image acquisition protocol. It was based on different experiments for measuring the factors which significantly influence image quality and which were likely to evolve during heating. The next part deals with the estimation of deformation fields from a dynamic set of MR images, and especially how the registration procedures, required for deformation field reconstruction, have been validated. Finally, an experimental model linking temperature and deformation is introduced and discussed.

2.3 MATERIALS AND METHODS

2.3.1 Samples and hardware

The samples come from *biceps femoris* bovine muscle, the connective network of which is elastin-rich. They were cut in the form of cylinders 5 cm in diameter by 6 cm in length with the muscle fibers oriented axially. The meat cylinders were then placed in plastic bags in a vacuum to prevent direct contact with the circulating heating water. Each sample was heated over the temperature range 20-75 °C using circulating water (42 l/min) in a magnetic environment-compatible device. This device comprised a watertight sample holder cell made of polyetheretherketone which was placed inside a sleeve made of Teflon for ensuring thermal insulation between the cell and the RF coil. The regulation system was programmed so that the temperature of the water rose constantly at a climb rate of 0.74 °C/min. The experiment is described in more detail in (7).

Image acquisition was carried out using a Biospec horizontal 4.7 T MRI system (Bruker GmbH, Ettlingen, Germany), of diameter 26 cm, equipped with a BGA-26 rapid gradient system (maximum amplitude 50 $mT.m^{-1}$, rise time 260 μs). The transmit-receive RF coil was a linear birdcage. The main fiber axis in the sample was placed approximately parallel to the main direction of the static magnetic field B_0 of the magnet. All MR acquisitions were performed in the transverse plane which intercepted the muscle fiber axis perpendicularly. The heating water run-off was roughly directed by the pump parallel to these muscle fascicles.

2.3.2 Measurement of muscle NMR properties during heating

The temperature rise induced changes in intrinsic NMR sample parameters. T_1, T_2 relaxation times and proton density (PD) were mapped according to the temperature from three images successively acquired using a single spin-echo sequence (8) (i.e. two images at different TR for T_1: TR_1 / TR_2 = 1000 / 5000 ms at the fixed TE = 7.2 ms and two images at different TE for T_2 and PD: TE_1 / TE_2 =7.2 / 37.2 ms and at the fixed TR = 5000 ms). Shimming, tuning and flip angle calibration procedures were carried out at each temperature step in order to minimize estimation errors due to instrumental shifts due to temperature changes. All the images were obtained with a FOV of 128 × 128 mm^2, a matrix of 32 × 32 voxels and thickness 10 mm (volume of a resulting voxel 4 × 4 × 10 mm^3). Parametric maps were reconstructed from the ratio of image pairs assuming a mono-exponential behavior of both T_1

and T_2 relaxation curves. The chemical shift was measured by PRESS localized spectroscopy in a single voxel, centered in the sample and of volume 4 × 4 × 6 mm^3. These measurements were taken at a constant step temperatures 10 °C apart.

2.3.3 Assessment of instrumental shifts during heating

In addition to the time course of the physical properties of the sample, the increase in the temperature caused a linear drift of the frequency tuning and impedance matching of the RF coil, which were optimized at the beginning of the experiment at 20 °C. This degradation was induced by a continuous variation of the coupling between the RF coil and the sample, due to (i) the deformation of the sample starting from ~ 42 °C (7, 9) and (ii) the variations in the dielectric properties of the muscle from 60 °C (i.e. dielectric permittivity and dielectric loss factor, 10). To measure the degradation of the signal-to-noise ratio (SNR) due to this drift during a typical heating ramp of 0.74 °C/min, SNRs of SSFP images were measured at 75 °C without and after re-tuning/matching of the loaded coil.

2.3.4 Flow mapping of circulating heating water

Velocity measurement of the heating water at the interfaces of the sample was necessary to calculate the heat exchange coefficient between water and sample. This coefficient is an essential boundary condition to numerically simulate the spatio-temporal distribution of temperature in the muscle (7). Also, the characterization of water run-off speed, and in particular the gradient in the tank, is useful for controlling the conditions of the experiment and helping to interpret the residual motion artifacts appearing in the images.

A phase-contrast flow imaging method (11) was thus used to map the water run-offs in the tank. It consisted of acquiring a reference image and three other velocity-encoded images from which the phase difference led to velocity assessment in read, phase and slice spatial-encoding directions (*i.e.* V_{read}, $V_{phase}$and V_{slice} respectively). The velocity magnitude was then computed from the three components using $V = \sqrt{V_{read}^2 + V_{phase}^2 + V_{slice}^2}$. The images (TR / TE = 5000 / 5.8 ms) were acquired in the center of a zone comprising the tank and the sample, with a flow range from −50 cm/s to +50 cm/s, a FOV of 128 × 128 mm^2, a matrix of 64 × 64 voxels and a slice thickness of 4 mm (volume of the resulting voxel 2 × 2 × 4 mm^3).

The temporal resolution (21’20”) of this protocol was too slow to make dynamic measurements during the heating. The speed of water in the tank was thus mapped at the

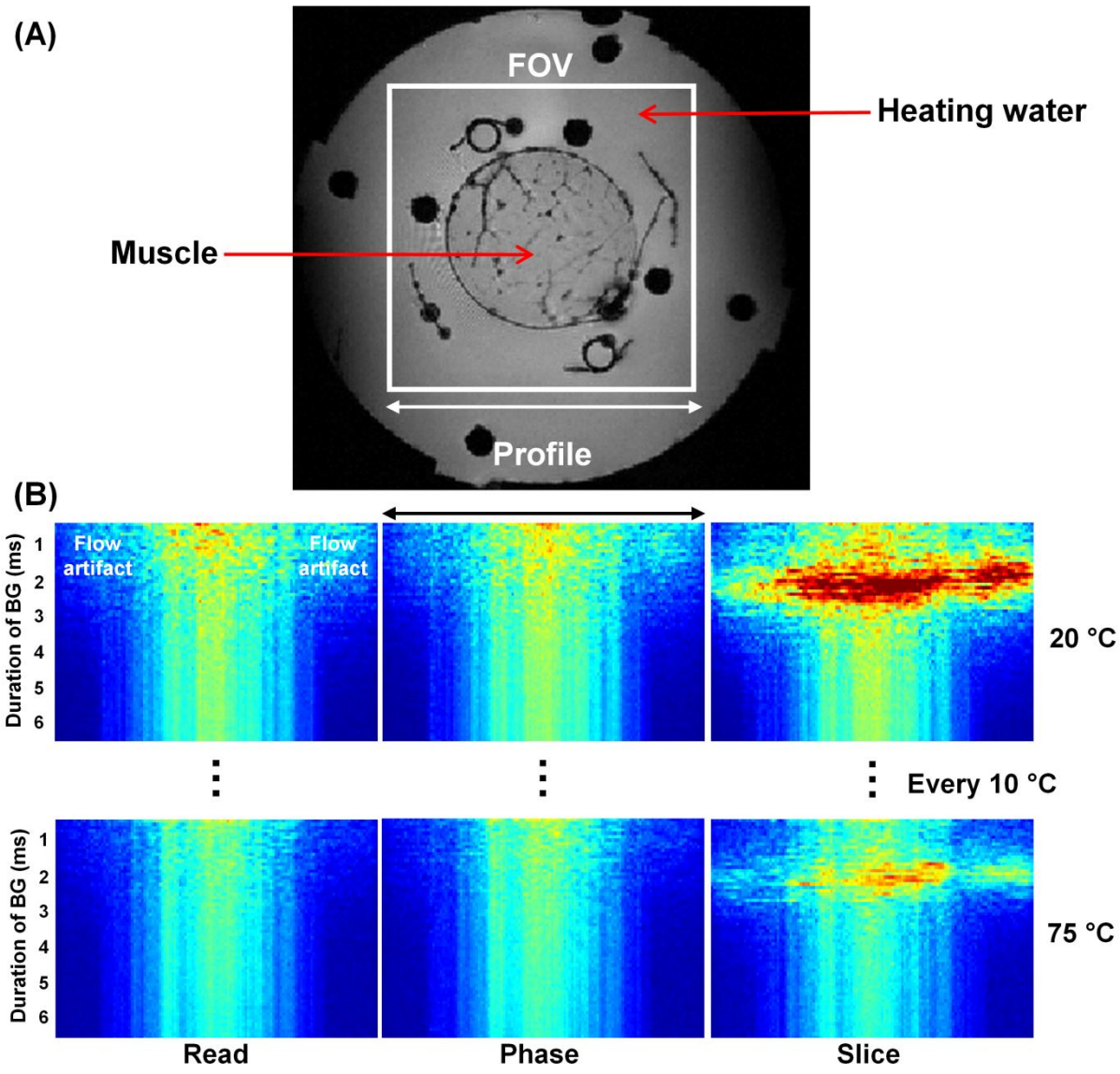

Figure 1: (A) Orientation and size of the profile for the sample tank. (B) Effect of BG duration on the cancellation of the heating water signal assessed by measuring the profile of the signal from the whole tank. The duration of the BG varies only in the specified direction, BG being applied in the other two directions for 7 ms at 45 mT.m^{-1}. The windowing of color levels was adjusted at each temperature to compensate for the continuous SNR loss.

extreme temperatures (*i.e.* 20 °C and 75 °C), by holding the temperature constant during the two acquisitions.

2.3.5 Suppression of the heating water signal

Uninterrupted water circulation during the experiment was essential to control the transfer of heat from the water to the sample. The NMR signal of circulating water thus had to be suppressed to obtain images of the muscle sample highlighting the internal fiducial markers. The solution adopted was to equip the sequences with bipolar gradients (BGs) which allowed the signal of the mobile protons to be attenuated proportionally to their velocity (12).

The high amplitude of the water signal (volume of water ~3 times that of the sample) and its low velocity in certain locations in the tank (cf. section B) required BGs of strong amplitude (i.e. 90% of the maximum amplitude of the gradients) for each acquired slice. In practice and despite the cooling of the gradients by water, the BGs generated an overheating of the gradient coil during multi-slice acquisitions, which threatened to damage the gradient coil and, by thermal conduction, the transmit-receive coil, which is in close contact. Accordingly, we used BGs of sinusoidal shape, which significantly reduced this overheating compared with the trapezoidal shape.

To determine the best direction and the minimal duration of the BGs that would ensure adequate suppression of the signal due to circulating water throughout the experiment, projections of the signal coming from the tank (i.e. from both sample and heating water) were measured for each of the three directions and varying the duration of the BGs (0.5 ms to 7 ms in 0.1 ms steps, amplitude 45 $mT.m^{-1}$) and the temperature (constant temperatures in steps of 10 °C). During a measure in a given direction, the BGs were maintained with 7 ms and 45 $mT.m^{-1}$ in the other two directions. The profiles were obtained with a steady-state free precession (SSFP) sequence with a single echo (TR/TE = 2000/18 ms) without phase encoding (which thus becomes the direction of projection, cf. Fig.1-A), a FOV of 64 × 64 mm^2 sampled on 128 points and a slice thickness of 2 mm (voxel volume of the resulting profile = 0.5 × 64 × 2 mm^3). To validate the effectiveness of the suppression for the whole sample, we measured these projections in ten 2 mm spaced planes transverse to the sample.

2.3.6 Image acquisition

A dynamic imaging experiment consisted in acquiring T_2^*-weighted images using a single echo SSFP sequence with sinusoidal BGs. A set of 20 acquisitions was continuously obtained

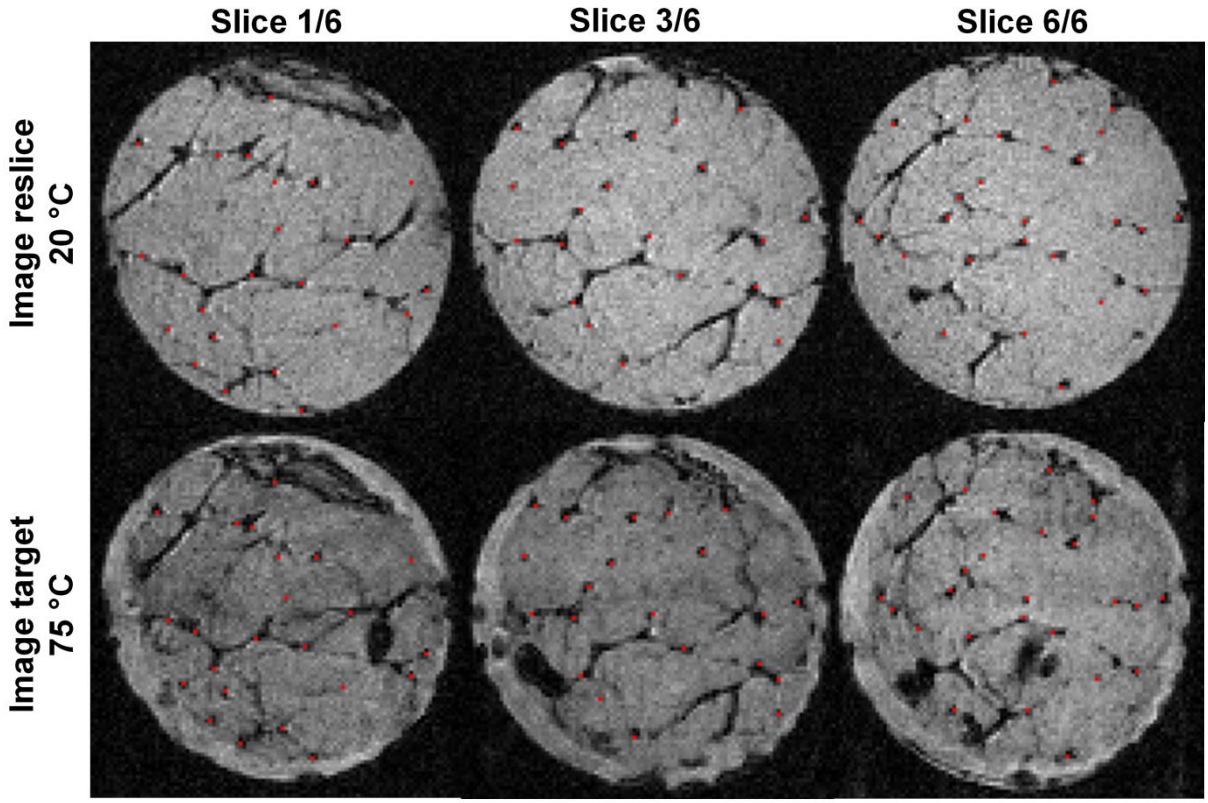

Figure 2: MR images obtained at 20 °C and 75 °C showing internal fiduciary markers and the positions of the pairs of landmarks (red points). Landmarks (number of Landmarks = 23, 21 and 26 respectively for sections 1, 3 and 6) were positioned manually on the images and used to optimize the 2D nonlinear deformation model.

during the temperature rise of heating water between 20 °C and 75 °C. For each acquisition, six transverse non-contiguous sections of the sample (interslice distance 4 mm) were obtained with a FOV of 64 × 64 mm^2, a matrix of 128 × 128 voxels and a thickness of 2 mm; the voxel volume was 0.5 × 0.5 × 2 mm^3 (temporal resolution 4'16", TR = 2000 ms). The deformation fields of the sample could be obtained by spatial registration of two successively acquired images (13). The geometrical transformation that minimizes the difference between these two images is an estimate of the deformation to be applied to switch from the initial image to the final image. During the heating from 20 °C to 75 °C, preliminary experiments showed that the deformation in the longitudinal direction of the sample was negligible (less than 3% in length). By contrast, it was marked in the transverse plane (35% of the surface) and it was anisotropic. The measurement of the deformation fields thus required a non-linear registration, limited to the two dimensions of the images obtained in this transverse plane.

2.3.7 Image registration

An automated image registration (AIR) package (14, 15) was chosen to perform this non-linear image registration because (i) it is available to the research community free of charge (http://bishopw.loni.ucla.edu/air5/), (ii) it allows many degrees of freedom (DOF) for performing non-linear deformations and (iii) it is efficient compared with the other algorithms (16-19). Non-linear deformation models have been compared by increasing the DOF of the polynomial warping. To compare these various models quantitatively, several pairs of landmarks were manually positioned on three different slices (Fig. 2) obtained at 20 °C (reslice image) and 75 °C (target image). These pairs of internal markers were characteristic points of the connective network, visible in hyposignal on MR images. We elected to evaluate the accuracy of registration on the two images acquired at the extreme temperatures rather than on two consecutive acquisitions in order to test the non-linear models on widely different amplitudes of deformation. The registration error (i.e. deformation estimate) was estimated by calculating, after the registration, the Euclidian distance between two homologous landmarks.

Suppressing the elements of no interest increases the accuracy and robustness of image registration (20, 21); thus a slice-by-slice manual segmentation of the muscle was always carried out before registration.

2.3.8 Measurement of deformation fields

Each slice of the image $I(t_{i-1})$, obtained at temperature t_{i-1}, was registered on its corresponding slice of $I(t_i)$. For this purpose, we used the 2D deformation model presenting

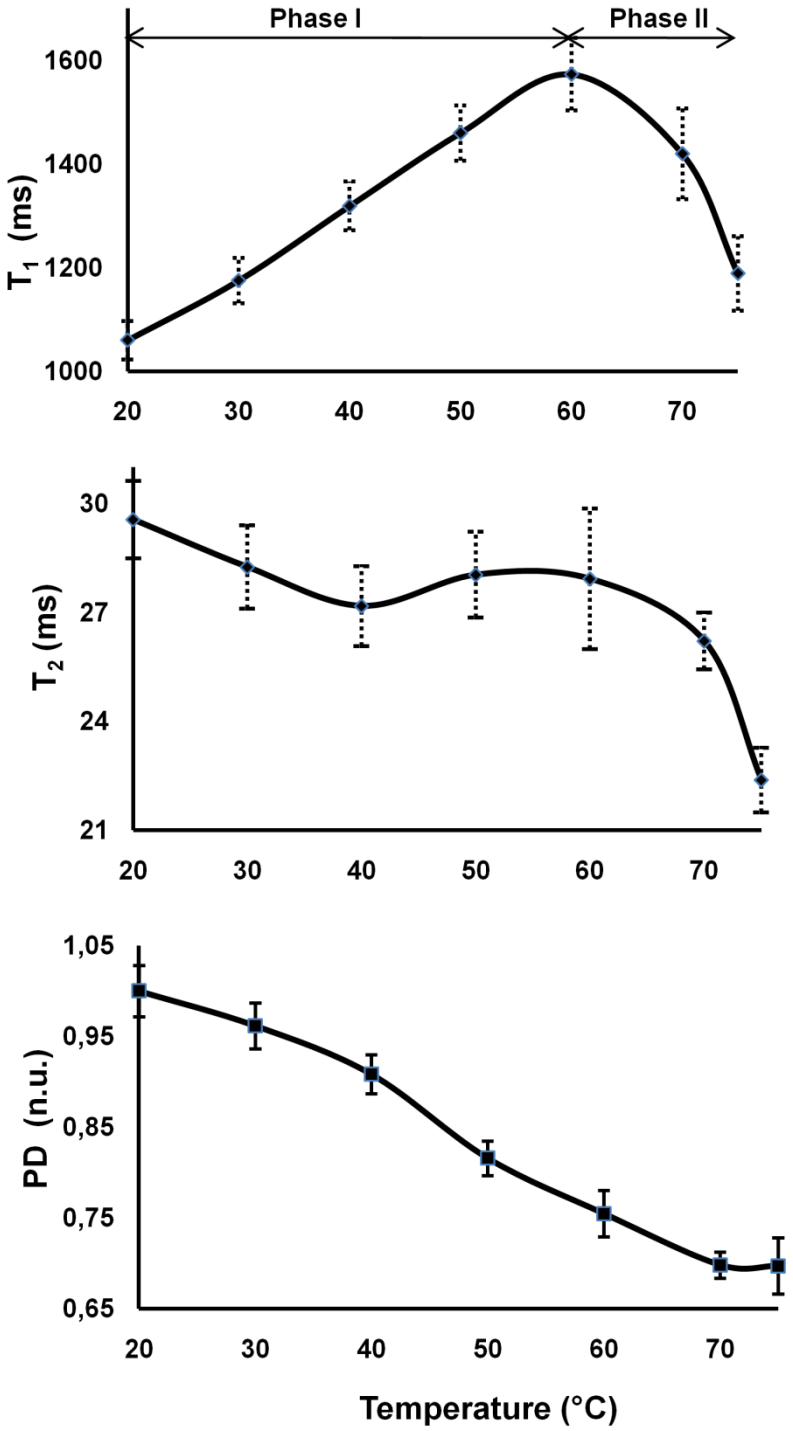

Figure 3: Time courses of T_1 and T_2 relaxation times and of PD with muscle temperature.

the minimum average error of registration (*i.e.* 4th order, see previous subsection). All parameters of the model being known after registration, the deformation field $\mathbf{w}(t_i)$ was inferred by computing the two components of 2D displacement in each voxel position of the image. This procedure was iterated for each successive pairs of the image sequence.

2.3.9 Deformation and temperature modeling

Each voxel of the image obtained at 20 °C was tracked by successively applying the transformation given by $\mathbf{w}(t_i)$. This monitoring thus allows deformation and temperature to be recorded at the same time for each voxel. Lastly the deformation is averaged over all the voxels in the slice for a given temperature.

2.4 RESULTS

2.4.1 Changes of muscle NMR properties during heating

Figure 3 presents the time courses of T_1, T_2 and PD with temperature, each point showing mean and standard deviation computed over all voxels belonging to the muscle. Between 20 °C and 75 °C, the combined action of temperature (i.e. obeying to Boltzmann distribution, PD changes by approximately 0.29 % / °C in our temperature range, (22)) and water transfers in the muscle led to an average decrease of 31% in PD, a decrease from 29 ms to 22 ms in main T_2 and an increase from 1050 ms to 1200 ms in T_1 (crossing a peak of 1600 ms at ~60 °C). The total SNR loss generated by these physicochemical properties variations in muscle was ~ 40%.

2.4.2 Instrumental shifts during heating

The quality factor of the loaded coil was almost unchanged (decrease of 3%) between the beginning and end of heating. However, the resonance frequency of the coil ω_c and its impedance at this frequency $Z(\omega_c)$ varied respectively by 254 kHz and 24%. The proton chemical shift with temperature was -0.0148 ppm / °C, in agreement with the literature value (23). An increase of 55 °C led to a chemical shift of 160 Hz, still low considering the voxel bandwidth used (390 Hz/voxel) and therefore generated small chemical shift artifacts. In addition, the ^1H peak broadened due to the deformation of the sample which degraded the homogeneity of the magnetic field in the sample from the initial shimming conditions. The total SNR loss caused by these extrinsic variations was ~15%. In all, our measurements show

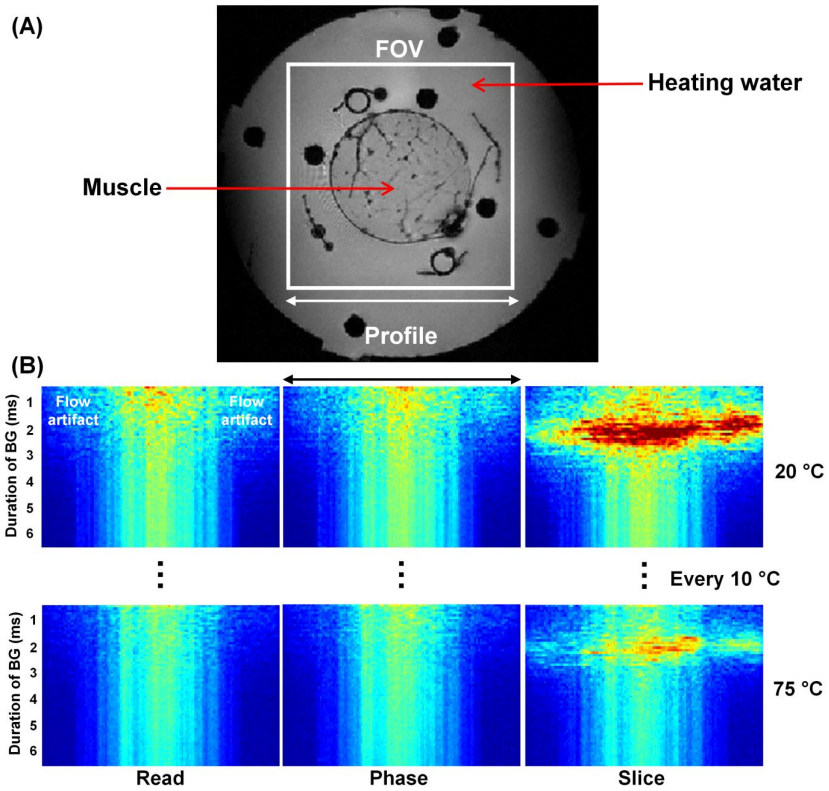

Figure 1: (A) Orientation and size of the profile for the sample tank. (B) Effect of BG duration on the cancellation of the heating water signal assessed by measuring the profile of the signal from the whole tank. The duration of the BG varies only in the specified direction, BG being applied in the other two directions for 7 ms at 45 mT.m^{-1}. The windowing of color levels was adjusted at each temperature to compensate for the continuous SNR loss.

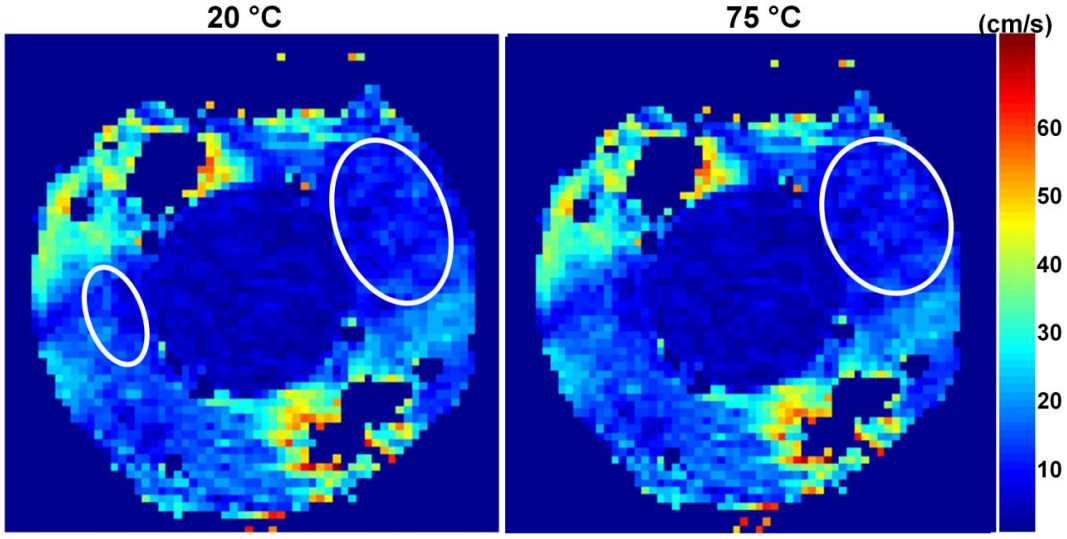

Figure 4: Distribution of the magnitude of the circulating water velocity in the tank at 20 °C and 75 °C. Circles define the regions of near stagnation of the heating water.

that the total loss in SNR was ~55% between 20 °C and 75 °C. The dominant causes of this decline were variations in the physical and chemical parameters of the muscle (~40%), the remaining ~ 15% being due to the changes in the coil/sample matching and the increase in temperature-dependent noise made by the sample.

2.4.3 Mapping of the heating water velocity

Apart from the areas with zero velocity corresponding to the presence of obstacles and air gap to water circulation in the tank, mapping of the velocity magnitude measured by MRI showed (i) that the distribution of the heating water velocity was not homogeneous in the tank (Fig. 4) and (ii) that velocity average decreased by 23% between the beginning and the end of the experiment. The range of velocity measured from this mapping at the borders of the sample lay between 3 cm/s and 45 cm/s. In this range, numerical simulations showed that the thermal transfer varied narrowly. The thermal and spatial distribution could therefore be obtained by numerical simulation with a low dependence on the boundary conditions (7).

2.4.4 Suppression of the heating water signal

Figure 1-B gives the average of projections in 10 non-contiguous slices, for each of the three directions of BG application. The artifacts produced by the circulating water predominated in the slice direction, because this was the principal direction of flow. Nevertheless, the signal of circulating water decreased with the duration of the BG for the three directions. To maximize image SNR, the quantitative analysis of these profiles showed that it was possible to reduce the BG duration to 4 ms, the signal coming from the mobile protons of the circulating water with this duration being equivalent to that obtained with duration of 7 ms, for which the suppression was total. At this minimal duration, the resulting TE was 14 ms. With this TE, the contrast between the connective network and muscle fibers was sufficient (Fig. 2). Figure 4 shows small quasi-stagnant areas (i.e. hypoflows), which produced light artifacts on images because of the reduced effectiveness of BG at low velocities. Fortunately, these artifacts did not distort the image registration process.

The diffusion weighting (*b*-value) of the imaging sequence with the BG was very low due to the short delay between the two sinusoidal lobes. The diffusion-related signal attenuation of muscle due to the BG effect was thus negligible, at both 20 °C (1.3%) and 75 °C (2.1%).

	2nd order	3rd order	4th order	5th order
Error (mm)	**Slice 1/6**			
mean	0.768	0.604	0.340	0.392
sd	0.442	0.323	0.271	0.364
min	0.251	0.186	0.009	0.026
max	1.597	1.015	0.803	1.202
	Slice 3/6			
mean	0.913	0.536	0.405	0.443
sd	0.563	0.503	0.327	0.390
min	0.147	0.048	0.003	0.050
max	1.999	1.781	1.007	1.260
	Slice 6/6			
mean	1.138	0.682	0.601	0.599
sd	0.671	0.524	0.507	0.615
min	0.134	0.036	0.024	0.034
max	2.207	2.115	2.042	2.503

Table 1: Parameters quantifying the registration error averaged over all pairs of landmarks. Results are represented for four non-linear models with increasing degrees of freedom and for three different slices.

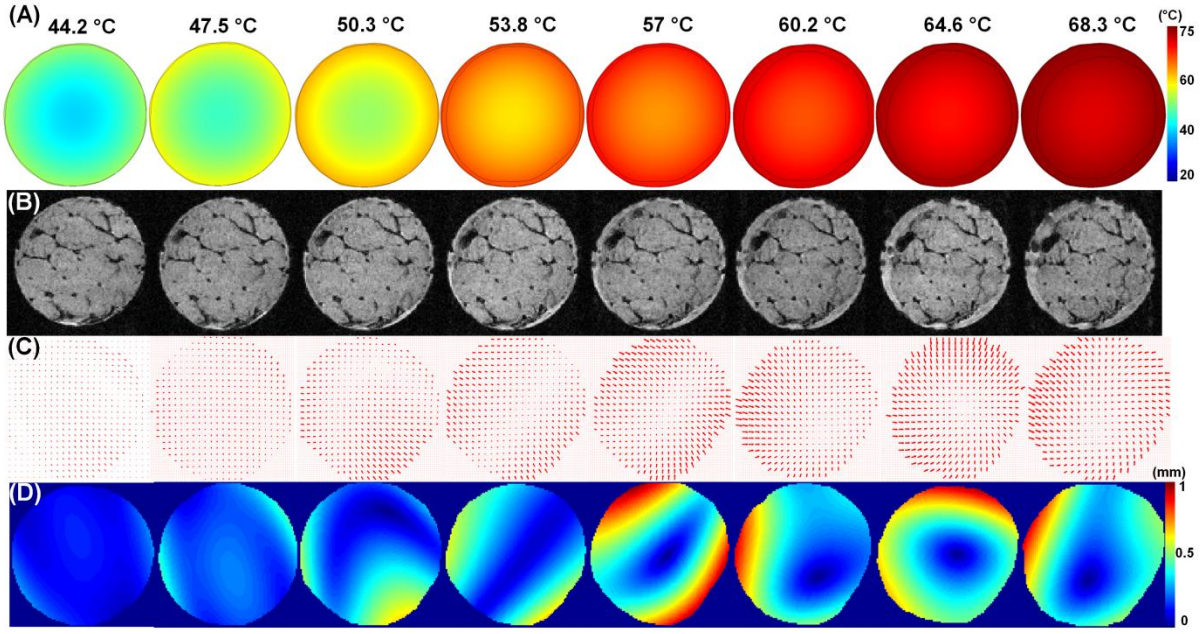

Figure 5: For eight average temperatures in the sample, (A) Temperature maps obtained by numerical simulation and (B) the corresponding NMR T_2-weighted images. The windowing of gray levels was adjusted for each image to compensate for the continuous SNR loss. (C-D) Representations, in direction and magnitude, of deformation field* **w**

2.4.5 Validation of image registration

Table 1 presents, for each of three slices, the statistical parameters quantifying the error of image registration derived from all landmarks. Registration error did not decrease monotonically with the number of degrees of freedom, but was minimal for the fourth order, as indicated consistently by all the measured criteria (mean, SD, min and max) in all slices. The 5^{th} order model led to degradation of the registration and no change was given by orders higher than the 5^{th}. Higher-order models diverged and led to an overestimation of deformations, especially at the sample borders. The use of higher-order polynomials introduced distortions because the number of supporting points was not sufficient.

2.4.6 Deformation fields during heating

Figure 5 shows simulated temperature maps, MR images showing fiducial markers inside the muscle and deformation fields (in direction and magnitude) in the central slice during a typical heating experiment. Only the maps corresponding to average temperatures in the muscle in the range ~44 °C to ~70 °C are represented, the deformation being negligible outside this range.

2.4.7 Deformation and temperature modeling

Local models linking temperature and deformation obtained by our original approach are given in Figure 6 for three slices. The standard deviations indicate the disparity of deformations for each temperature in the muscle.

2.5 DISCUSSION

The consequences of heating on both muscle and experimental conditions are difficult to predict. For this reason, several measurements were conducted prior to the *in situ* experiments devoted to deformation assessement, in order to optimize their imaging conditions. Those concerning the impact of heating on relaxation properties and PD of muscle assumed mono-exponential behavior of decays. It seems reasonable if one refers to a previous NMR relaxation study in meat which revealed during cooking a merging of small T_2-components into a persistent bulk peak (9), the latter corresponding to the one measured by imaging. Despite a slight T_1 underestimation of less than ~ 5% due to an insufficient TR length, the changes of muscle NMR properties during heating highlight two main phases (Fig. 3): during

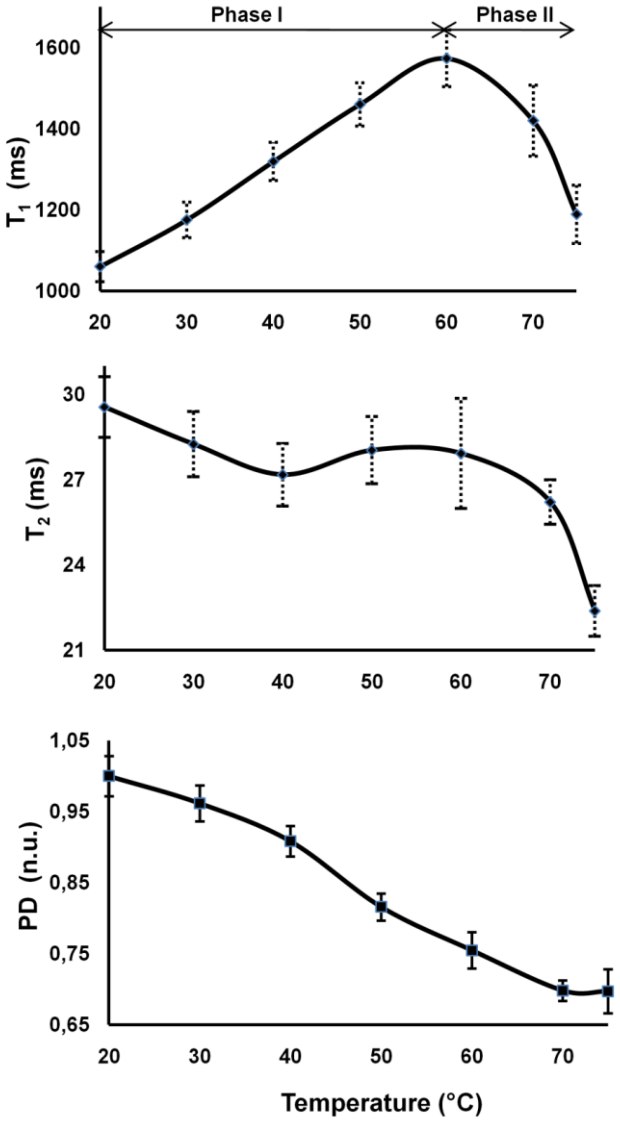

Figure 3: Time courses of T_1 and T_2 relaxation times and of PD with muscle temperature.

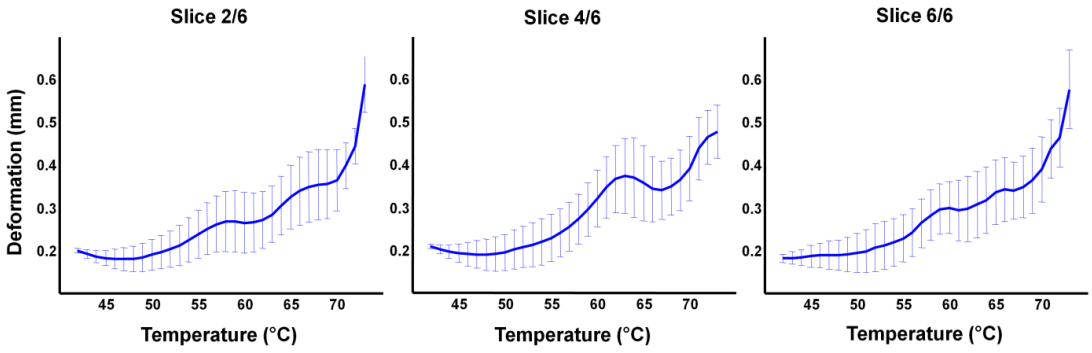

Figure 6: Time course of muscle deformation magnitude with temperature.

phase I (i.e. up to ~60 °C in the sample), T_1 increased because of the decrease of the correlation time τ_c between water molecules with temperature, which increases the rate of dipole-dipole interactions (24). This increase was similar to that observed at 63 MHz in a more restricted temperature range (25). According to Nelson and Tung (26), T_2 varies little with temperature in this phase. During phase II, the water expulsion outside the sample due to the contraction of the muscle with heat produces a marked decrease in the PD. The elevation of the resulting protein concentration induces stronger interactions between these macromolecules and residual water, and thus explains the simultaneous decrease of T_1 and T_2. Quantitatively, the physicochemical properties of muscle therefore evolve with heating, all adversely affecting the SNR.

Instrumental shifts due to heating also affect SNR. Because there was no automatic tuning and matching system, the correction of these degradations had to be done manually during the experiment. We opted to tolerate this loss to maintain a continuous acquisition of T_2^*-weighted images, the tuning and matching of the loaded coil being optimized only at the beginning of the experiments at 20 °C.

At 4.7 T and for an internal diameter of the coil twice the diameter of the tank, thermal noise produced by the tank was dominant compared with that due to the coil (27, 28). Image noise therefore increased with the temperature of the water and of the sample in the tank. Under these conditions, the image noise depended only slightly on the quality factor of the coil. Thus our transmit-receive RF birdcage coil with linear polarization was proven to be an appropriate choice.

The decrease of heating water average velocity measured by flow mapping is counterintuitive, since an increase in the velocity could be expected due to a decrease in water viscosity with temperature. Estimation of Reynolds number shows that the flow in the tank is far beyond the transitional regime between laminar and turbulent regimes. In addition, turbulences are caused by various obstacles present in the tank (e.g. the sample itself and the tank walls).Therefore the flow is turbulent in our whole range of temperatures. Such regime leads to inhomogeneous intravoxel velocity distribution for which the mean intravoxel phase is not proportional to the mean velocity, and then biases velocity estimation using phase-encoded MR maps. To summerize, the found decrease in heating water velocity may be due to the underestimation inherent to the mapping method and changes of flow distribution due to the decrease in water viscosity with temperature. Besides, a decrease in the pump effectiveness

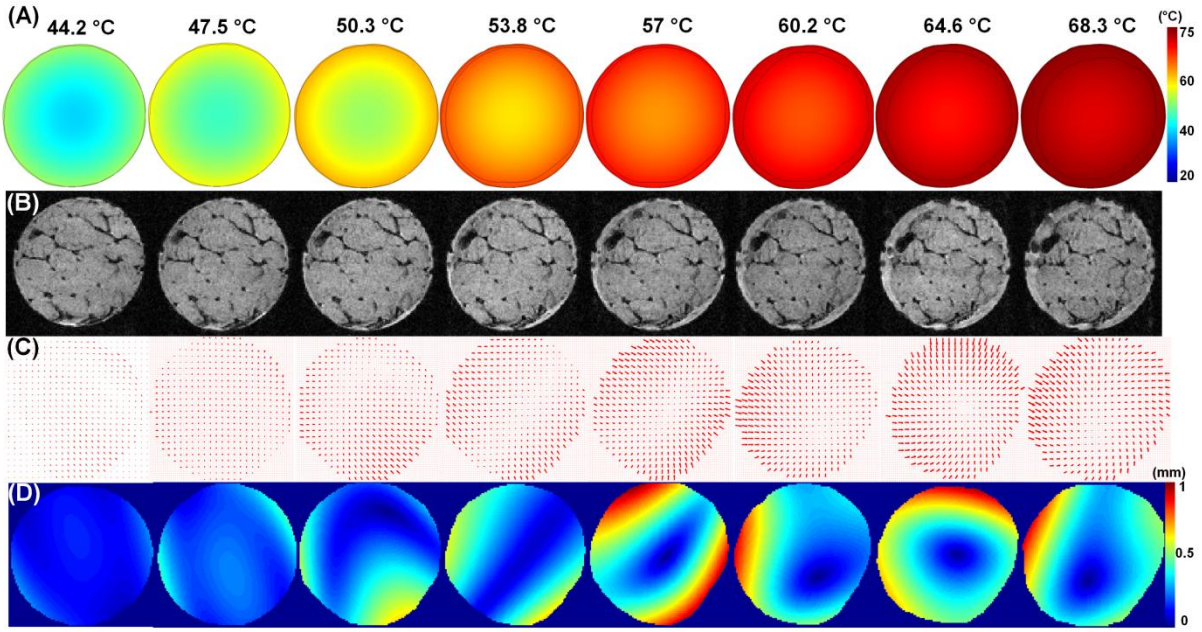

Figure 5: For eight average temperatures in the sample, (A) Temperature maps obtained by numerical simulation and (B) the corresponding NMR T_2^*-weighted images. The windowing of gray levels was adjusted for each image to compensate for the continuous SNR loss. (C-D) Representations, in direction and magnitude, of deformation field **w**.

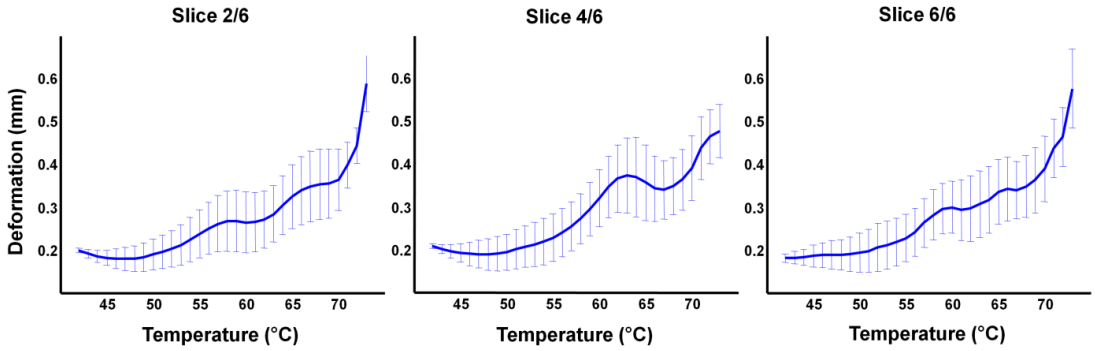

Figure 6: Time course of muscle deformation magnitude with temperature.

with temperature cannot be excluded. Inhomogeneous intravoxel velocity distribution due to turbulent regime also explains why BG attenuates the signal of flowing heating water in the three directions (Fig. 1-B) and why they had to be applied simultaneously along these three directions during acquisition of flow-suppressed T_2^*-weighted images. As a precaution, the measured decrease of 23% in the heating water average velocity should have required increasing the efficiency of the suppression pattern with temperature. This was not necessary because, simultaneously with the deceleration, the hot water signal decreased strongly (from ~55% between 20 °C and 75 °C), owing to the concomitant increases in temperature diffusion coefficient (29, 30) and T_1, and decrease in T_2.

Temperature maps and T_2^*-weighted images respectively show spatial heterogeneity in temperature (Fig. 5-A) and a sufficient image quality to locate internal fiducial markers despite the continuous loss of SNR (Fig. 5-B). Mass transfers are observable which correspond to water exudation in the interfascicular spaces and outside muscle. They are discussed in detail in (7). Deformation fields in the muscle (Fig. 5-C, D) changed with time and were spatially heterogeneous. This result experimentally validates the utility of imaging for temporal and spatial coupling of temperature and deformation. This deformation was greater at the surface than at the center of the sample because of the facilitated heat exchange on the sample surface. There was a process of contraction of the muscle fibers at the center of the sample causing expulsion of liquid towards the outside of the sample (Fig. 5-B). However, we observed that the deformation did not follow the same radial symmetry as the distribution of temperature, emphasizing that other factors determine deformation, in particular structural factors such as the distribution of the connective network.

Models linking temperature and deformation show similar behaviors (Fig. 6). Local information highlights a moderate strain between ~42 °C and ~55 °C. This phase corresponds to myosin denaturing and the beginning of the collagen denaturing (9, 31) which explain the low observed deformation. Juice transfers take place essentially to interfascicular spaces within the muscle (7). The deformation accelerated from ~55 °C due to the temperature effect on both sarcoplasmic proteins, leading to their denaturing and therefore to a reduction of the mechanical resistance of the fibers to compression (32), and collagen inducing contraction of the connective network (33). Water is then expelled to the outside of the sample (7), which explains the strong observed deformation. Plateaus and the new acceleration of the deformations that occur from ~68 °C remain difficult to interpret. They could be explained by

some other temperature-dependent denaturing (10, 34) or by specific mechanisms of internal transfer of juice. This also justifies spatio-temporal monitoring of the water density to interpret the obtained models.

In order to measure the deformation fields, we opted to follow internal markers linked to the muscular structure. Other MRI-based approaches are possible. For example, velocimetry techniques such as that used here to measure the velocity of the circulating water. The latter method is, however, not well-adapted to our context because of its low temporal resolution and the difficulty measuring low velocities. The technique based on tagging could be an option (35), but is better suited to the monitoring of deformations more rapid than those induced by heating in muscle, i.e. those leading to significant displacements during a period corresponding to T_1 of imaged tissues.

2.6 CONCLUSION

Developments in dynamic MRI, the quantitative characterization of experimental conditions and the optimization of non-linear registration enabled us to measure deformation fields in muscle during heating. A first interpretation of the mechanisms involved in muscle contraction with temperature is proposed. It is based on the models developed from local information on deformation and temperature.

The simple repetition of the experiment on several muscles of the same type will increase the robustness of models. The application of the same experimental approach to different muscle types will help elucidate the influence of structure on deformation during thermal processes, and thereby give information on the mass losses and degradation of the textural properties of cooked meat.

2.7 CITED REFERENCES IN ARTICLE 2

1. Damez JL, Clerjon S. Meat quality assessment using biophysical methods related to meat structure. Meat Sci 2008;80:132-149.

2. Micklander E, Peshlov B, Purslow PP, Engelsen SB. NMR-cooking: monitoring the changes in meat during cooking by low-field ^{1}H-NMR. Trends in Food Sci Tech 2002;13:341-346.

3. Bonny JM, Laurent W, Renou JP. Detection of susceptibility effects using simultaneous T_2^* and magnetic field mapping. Magn Reson Imaging 2000;18:1125-1128.

4. Bonny JM, Laurent W, Labas R, Taylor R, Berge P, Renou JP. Magnetic resonance imaging of connective tissue: a non-destructive method for characterising muscle structure. J Sci Food Agric 2000;81:337-341.

5. Kohler S, Hiller KH, Waller C, Bauer WR, Haase A, Jakob PM. Investigation of the microstructure of the isolated rat heart: A comparison between T_2^*- and diffusion-weighted MRI. Magn Reson Med 2003;50:1144-50.

6. Kohler S, Hiller KH, Waller C, Jakob PM, Bauer WR, Haase A. Visualization of myocardial microstructure using high-resolution T_2^* imaging at high magnetic field. Magn Reson Med 2003;49:371-5.

7. Bouhrara M, Clerjon S, Damez JL, Chevarin C, Portanguen S, Kondjoyan A, Bonny JM. Dynamic MRI and Thermal Simulation To Interpret Deformation and Water Transfer in Meat during Heating. J Agric Food Chem 2011;59:1229-35.

8. Lee JN, Riederer SJ. Optimum acquisition times of two spin echoes for MR image synthesis. Magn Reson Med 1986;3:634-638.

9. Bertram HC, Engelsen SB, Busk H, Karlsson AH, Andersen HJ. Water properties during cooking of pork studied by low-field NMR relaxation: effects of curing and the RN--gene. Meat Sci 2004;66:437-446.

10. Bircan C, Barringer SA. Determination of Protein Denaturation of Muscle Foods Using the Dielectric Properties. J Food Sci 2002;67:202-205.

11. Pelc NJ, Bernstein MA, Shimakawa A, Glover GH. Encoding strategies for three-direction phase-contrast MR imaging of flow. J Magn Reson Imaging 1991;1:405-413.

12. Pipe JG, Chenevert TL. A progressive gradient moment nulling design technique. Magn Reson Med 1991;19:175-179.

13. Hellier P, Barillot C, Memin E, Perez P. Hierarchical estimation of a dense deformation field for 3-D robust registration. IEEE Trans Med Imaging 2001;20:388-402.

14. Woods RP, Grafton ST, Holmes CJ, Cherry SR, Mazziotta JC. Automated Image Registration: I. General Methods and Intrasubject, Intramodality Validation. J Comput Assist Tomogr 1998;22:139-152.

15. Woods RP, Grafton ST, Watson JDG, Sicotte NL, Mazziotta JC. Automated Image Registration: II. Intersubject Validation of Linear and Nonlinear Models. J Comput Assist Tomogr 1998;22:153-165.

16. Strother SC, Anderson JR, Xu XL, Liow JS, Bonar DC, Rottenberg DA. Quantitative Comparisons of Image Registration Techniques Based on High-Resolution MRI of the Brain. J Comput Assist Tomogr 1994;18:954-962.

17. West J, Fitzpatrick JM, Wang MY, Dawant BM, Maurer CRJ, Kessler RM, Maciunas RJ, Barillot C, Lemoine D, Collignon A, Maes F, Suetens P, Vandermeulen D, van den Elsen PA, Napel S, Sumanaweera TS, Harkness B, Hemler PF, Hill DLG, Hawkes DJ, Studholme C, Maintz JBA, Viergever MA, Malandain G, Pennec X *et al*. Comparison and Evaluation of Retrospective Intermodality Brain Image Registration Techniques. J Comput Assist Tomogr 1997;21:554-568.

18. Morgan VL, Pickens DR, Hartmann SL, Price RR. Comparison of functional MRI image realignment tools using a computer-generated phantom. Magn Reson Med 2001;46:510-514.

19. Klein A, Andersson J, Ardekani BA, Ashburner J, Avants B, Chiang MC, Christensen GE, Collins DL, Gee J, Hellier P, Song JH, Jenkinson M, Lepage C, Rueckert D, Thompson P, Vercauteren T, Woods RP, Mann JJ, Parsey RV. Evaluation of 14 non-linear deformation algorithms applied to human brain MRI registration. NeuroImage 2009;46:786-802.

20. Blaffert T, Wiemker R. Comparison of different follow-up lung registration methods with and without segmentation. SPIE Medical Imaging 2004;5370:1701-1708.

21. Hajnal JV, Saeed N, Soar EJ, Oatridge A, Young IR, Bydder GM. A Registration and Interpolation Procedure for Subvoxel Matching of Serially Acquired MR Images. J Comput Assist Tomogr 1995;19:289-296.

22. Chen J, Daniel BL, Pauly KB. Investigation of Proton Density for Measuring Tissue Temperature. J Magn Reson Imaging 2006;23:430-434.

23. Hindman JC. Proton Resonance Shift of Water in the Gas and Liquid States. J Chem Phys 1966;44:4582-4592.

24. Bloembergen N, Purcell EM, Pound RV. Relaxation Effects in Nuclear Magnetic Resonance Absorption. Phys Rev 1948;73:679.

25. Cline HE, Hynynen K, Hardy CJ, Watkins RD, Schenck JF, Jolesz FA. MR temperature mapping of focused ultrasound surgery. Magn Reson Med 1994;31:628-636.

26. Nelson TR, Tung SM. Temperature dependence of proton relaxation times in vitro. Magn Reson Imaging 1987;5:189-199.

27. Darrasse L, Ginefri J-C. Perspectives with cryogenic RF probes in biomedical MRI. Biochimie 2003;85:915-937.

28. Hoult DI, Lauterbur PC. The sensitivity of the zeugmatographic experiment involving human samples. J Magn Reson 1979;34:425-433.

29. Le Bihan D, Delannoy J, Levin RL. Temperature mapping with MR imaging of molecular diffusion: application to hyperthermia. Radiology 1989;171:853-857.

30. Delannoy J, Chen CN, Turner R, Levin RL, Le Bihan D. Noninvasive temperature imaging using diffusion MRI. Magn Reson Med 1991;19:333-339.

31. Palka K, Daun H. Changes in texture, cooking losses, and myofibrillar structure of bovine M. semitendinosus during heating. Meat Sci 1999;51:237-243.

32. Wright DJ, Leach IB, Wilding P. Differential scanning calorimetric studies of muscle and its constituent proteins. J Sci Food Agric 1977;28:557-564.

33. Lepetit J. Collagen contribution to meat toughness: Theoretical aspects. Meat Sci 2008;80:960-967.

34. Tornberg E. Effects of heat on meat proteins - Implications on structure and quality of meat products. Meat Sci 2005;70:493-508.

35. Axel L, Dougherty L. MR imaging of motion with spatial modulation of magnetization. Radiology 1989;171:841-845.

3. Article 3 : Imagerie rapide à haute résolution spatiale pour l'analyse de la structure fondée sur un contraste en susceptibilité magnétique

Nous avons démontré la faisabilité du suivi *in situ* par IRM de la déformation du muscle durant un procédé thermique, ainsi que de la cartographie de température par simulation numérique. Pour cartographier les champs de déformation, nous avons ensuite validé une méthodologie fondée sur le recalage non-linéaire d'images RMN successives acquises pendant la cuisson. Un modèle préliminaire reliant déformation et température a été mis en place.

Néanmoins, la robustesse de ce modèle dépend de la résolution spatiale et temporelle des images RMN. L'augmentation de la résolution spatiale met en évidence plus de marqueurs internes (réseau conjonctif fin) dans les images, et améliore donc la précision du recalage et par conséquent la construction des champs de déformation. L'amélioration de la résolution temporelle permet quant à elle de suivre fidèlement les déformations rapides du muscle au cours du chauffage.

D'un autre coté, il est primordial d'avoir une information locale et en continue sur le transfert d'eau dans le muscle afin de comprendre les mécanismes reliant localement, température, déformation et quantité d'eau. Ceci nécessite donc d'acquérir d'autres images pour simultanément quantifier la densité de protons et corriger les hétérogénéités du champ radiofréquence B_1 de l'antenne utilisée. Finalement, dans une même expérience, le processus d'acquisition nécessite une succession de quatre blocs d'images, répétée au cours de l'expérience, ce qui représente un temps d'acquisition conséquent en utilisant des séquences d'IRM classiques.

De nouvelles techniques d'IRM ont donc été développées et testées expérimentalement pour acquérir rapidement des images pondérées en susceptibilité magnétique de résolution spatiale élevée. Ces techniques se fondent sur la combinaison dans l'espace de Fourier - appelé également espace k (l'espace des fréquences spatiales) - d'un train d'échos de gradient, combinée à une stratégie plus classique d'acquisition partielle de l'espace k. Les résultats montrent qu'il est possible d'accélérer les acquisitions d'un facteur ~3.5, en maintenant la résolution spatiale élevée des techniques précédentes. Plus précisément, ceci conduit à un

volume de voxel de 0,25 x 0,25 x 2 mm^3 pour un temps d'acquisition de ~1min30s avec un rapport signal sur bruit suffisant durant l'ensemble du chauffage.

Si ces techniques sont pertinentes pour notre application, elles le sont aussi pour les études structurales fondées sur l'analyse des variations locales de phase et du temps de relaxation transversale apparent T_2^*. Ces dernières visent à déterminer l'organisation tissulaire à l'intérieur du voxel et ont trouvé récemment différentes applications biologiques comme par exemple dans le cerveau ou l'os (Dyun 2007, Wehrli 2007, Mittal 2009, Haacke 2009).

Ce manuscrit est encore en préparation pour être soumis en 2012 à *Magnetic Resonance Materials in Physics, Biology and Medicine*. Ce manuscrit est préparatoire au sens où certains aspects doivent être complétés. Il s'agit en particulier de la reconstruction des données obtenues en mode GESFID pour corriger ou minimiser les artefacts dans les images, notamment à faible résolution spatiale. Une analyse de la répercussion de l'accélération sur les images de phase serait aussi souhaitable car l'analyse structurelle à partir des images pondérées en T_2^* se fonde de plus en plus sur l'analyse spatiale de la phase. Enfin, d'autres modes de répartition des échos dans l'espace k pourraient être testés et discutés, afin d'améliorer la généricité de la méthode.

High-resolution susceptibility-weighted MRI for fast structural imaging

Mustapha BOUHRARA, Sylvie CLERJON, Jean-Louis DAMEZ and Jean-Marie BONNY.

UR370 Qualité des Produits Animaux, INRA, F-63122 Saint-Genès-Champanelle

Phone: +33-4- 73-62-41-52.

Fax: +33-4-73-62-40-89

E-mail: jean-marie.bonny@clermont.inra.fr

3.1 INTRODUCTION

Biological tissues result from the assembly of compounds with different sizes, shapes and magnetic susceptibilities. It results in a complex organization-related behavior of the NMR signal decay which comes from the averaging of the inhomogeneous magnetic field originated from the magnet and all susceptibility material distribution. It paves the way for an indirect structure characterization of biological tissues at a scale inferior to the mesoscopic scale of observation, corresponding to the voxel size, when NMR imaging or localized spectroscopy are used. This general principle was applied for detecting the presence of intra-voxel insertions in various biological tissues with substantially improved resolution, e.g. in brain [1-4], in bone [5] and in muscle [6, 7], or for visualizing contrast agents [8]. This approach requires however being able both to relate distribution of arbitrarily shaped objects with phase and magnitude time-course of T_2^*-weighted signal [9-11] and to acquire high-resolution T_2^*-weighted images at high-field. The reference method is based on the conventional gradient-recalled echo (GE) [12] sequence with a high spatial resolution for suppressing image distortions and restoring signal loss due to magnetic field inhomogeneities [13, 14]. Due to the desired long echo time and high isotropic resolution, acquisition is often a prolonged process and the images suffer from relatively poor signal-to-noise ratio (SNR).

In this study, we propose two complementary strategies based on multiple gradient echo acquisition for reducing the time need for acquiring high-resolution T_2^*-weighted images obtained with a Cartesian filling of *k*-space. This improvement makes sense for applications needing both high spatial and time resolutions. It is applied here for an application which requires highly resolute T_2^*-weighted images for revealing thin layers of intramuscular connective tissue (i.e. elastin and lipids) and for monitoring the rapid changes of muscle structure at specific temperatures.

3.2 MATERIALS AND METHODS

3.2.1 Samples and hardware

The samples come from *biceps femoris* bovine muscle, the elastin-rich connective network being discernable on T_2^*-weighted images. Samples were cut in the form of cylinders 5 cm in diameter by 6 cm long with the muscle fibers oriented axially. Each sample was heated over

the temperature range 20-75 °C using circulating water (42 l/min) in a magnetic-compatible environment device described in detail in [15].

Image acquisition was carried out using a Biospec horizontal 4.7 T MRI system (Bruker GmbH, Ettlingen, Germany), equipped with a BGA-26 rapid gradient system (maximum amplitude 50 $mT.m^{-1}$, rise time 260 µs, diameter 26 cm). The transmit-receive RF coil was a linear birdcage. The main fiber axis in the sample was placed approximately parallel to the main direction of the static magnetic field B_0 of the magnet.

3.2.2 Strategies for accelerating acquisition of T_2^*-weighted image

Even if the spiral readout trajectory allows the *k*-space to be traversed rapidly and efficiently [16, 17], Cartesian sampling is preferable because it is less prone to off-resonance artifacts when using a short readout time. In this context, a generic strategy of acceleration consists in acquiring multiple echoes during the unused time interval because it does not require extra scan time, as in echo-planar (EPI) [18] or rapid acquisition with relaxation enhancement (RARE) imaging [19]. According to the concept of GE sampling of FID and (spin) echo introduced by Ma and Wehrli [20], there are two possible strategies for acquiring multiple GE during a single shot. The first one does not require a refocusing pulse and consists in sampling only the descending portion of FID (GESFID) which provides GEs at increasing gradient-echo time (*tGE*) and then with increasing T_2- and T_2'-weightings, i.e.

$$S(tGE_i) \propto \exp(-tGE_i/T_2).\exp(-tGE_i/T_2'). \qquad [1]$$

Provided SNR is sufficient for acquiring *n* GEs, it accelerates imaging process by *n* and the ordering the phase-encoding gradient can be optimized by putting the desired echo at the center of the *k*-space and then adapting the contrast to the desired T_2^*-weighting [21, 22]. In our case, we favored centric encoding because the T_2^*-weighting of the first GE obtained at14 ms was sufficient for highlighting intramuscular connective tissue. Noted that this tGE_1 was shifted because bipolar gradients were applied after the excitation pulse and simultaneously along the three directions of space for suppressing the artifacts produced by the heating circulating water [23].

The second approach requires a refocusing pulse and consists in sampling the descending portion of FID and both the ascending and descending parts of the spin-echo (GESFIDE). Because of the irreversibility of T_2-dephasing, it still provides GEs with increasing T_2-weightings. However, it allows acquiring three GEs with the same T_2'-weighting using

adequate tGEs. Let introduce the spin-echo time *tSE* corresponding to the basic sequence $\alpha_x - tSE/2 - \beta_y - tSE/2$. The desired T_2'-weighting is determined by tGE_1 (i.e. $\exp(-tGE_1/T_2')$) which samples FID on its dephasing part. The next two GEs sample rephasing and dephasing portions of the spin-echo with the same T_2'-weighting provided $tGE_2 = tSE - tGE_1$ and $tGE_3 = tSE + tGE_1$. As for GESFID, we favored centric encoding because of the higher SNR of the first GE.

For further acceleration, GESFID and GESFIDE strategies were combined with partial Fourier (PF) acquisition [24]. Slightly more than half of the total number of required phase encoded lines of the *k*-space were acquired, which reduces scan time by nearly 2 compared to a full acquisition. According to Finsterbusch *et al*. [25], 5/8 of *k*-space was kept in order to get few extra lines near the center of *k*-space for correcting phase-induced artifacts due to this asymmetric coverage of *k*-space. These artifacts were minimized using an iterative projection onto convex sets algorithm [26] which reconstructs image on the basis of the regularized phase information obtained in the preserved center of the *k*-space.

3.2.3 Experiments

Experiments were designed (i) to compare images obtained with GESFID and GESFIDE modes to those obtained from a single-echo GE, (ii) to analyze the effects of half Fourier acquisition (iii) to show the results of dynamic structural imaging under optimized conditions of resolutions and contrast. All the images were acquired with bipolar gradient pulses applied in the three encoding directions to suppress artifacts coming from the circulating heating water [23].

GESFID and GESFIDE images were successively acquired during heating at 20 °C. For both, the full *k*-space of the three echoes were acquired during the same TR with the following timing of T_2^* time-courses : $tGE_{1,2,3}$ = 13.7, 26.4, 39.2 ms for GESFID and with $tGE_{1,2,3}$ = 13.8, 24.3, 51.5 ms for GESFIDE with *tSE* = 38 ms for the first spatial resolution, $tGE_{1,2,3}$ = 15, 27.5, 40.1 ms for GESFID and with $tGE_{1,2,3}$ = 15.6, 31, 61.6 ms for GESFIDE with *tSE* = 46.4 ms for the second spatial resolution. Under these conditions (which have been explained before), the three GEs of GESFIDE exhibited the same T_2'-weightings. The other image parameters were: Cartesian encoding, TR = 2 s, flip angle (FA) = 80°, FOV = 64 x 64 mm², matrix = *m* x *m* where *m* = 128 for resolution 1 and *m* = 256 for resolution 2 and slice thickness = 2 mm, number of slices = 6, leading to a voxel volume of 0.5 × 0.5 × 2 mm^3 and

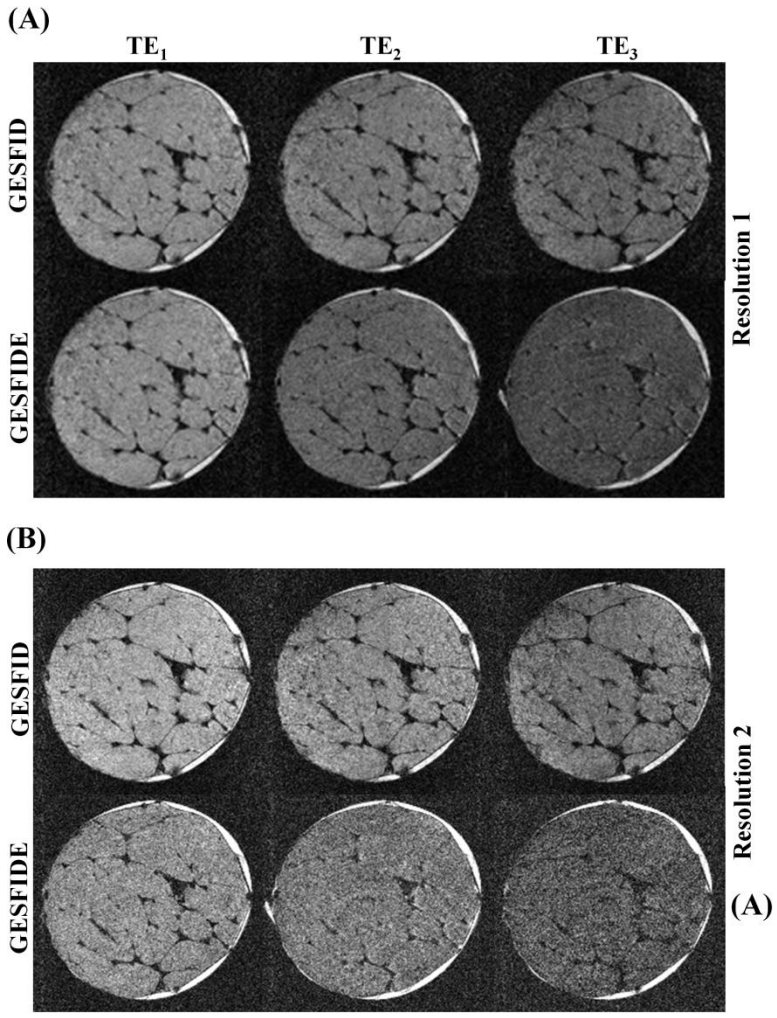

Figure 1: Susceptibility-weighted images of muscle obtained at three different echo times with GESFID and GESFIDE and at two spatial resolutions.

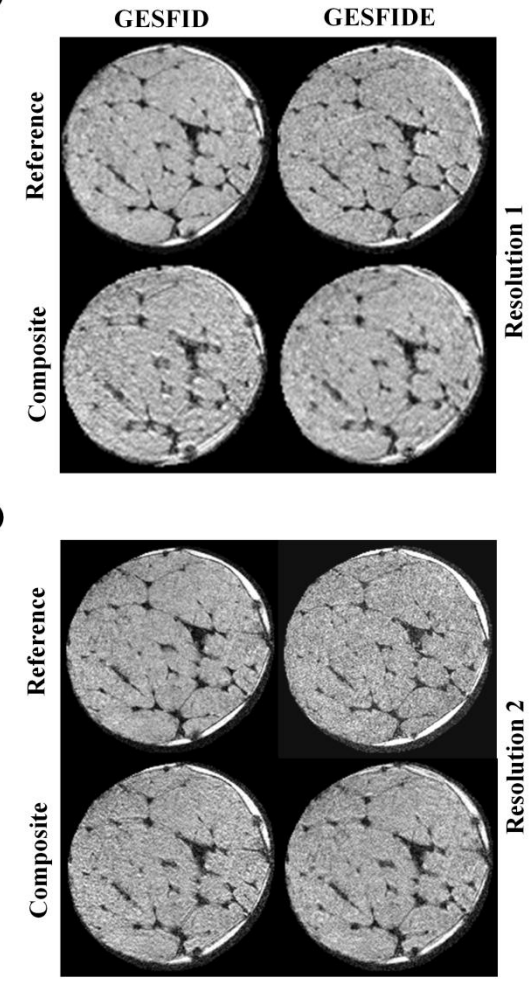

Figure 2: Effect of echo combination for GESFID and GESFIDE at two spatial resolutions. k-space is filled in a centric fashion, i.e. the first GE occupying the center of the resulting k-space and the last one the upper thirds.

$0.25 \times 0.25 \times 2$ mm^3 respectively. A pair of sinc selective pulses of the same bandwidth (4 kHz) were used for excitation and refocusing.

Composite GESFID and GESFIDE images were reconstructed offline by multiplexing *k*-spaces of the three corresponding echoes in a centric fashion, the first GE occupying the center of the resulting *k*-space for the reason explained previously. GESFID and GESFIDE composite images were compared to their reference which corresponds to the first GE of the train.

For half Fourier imaging, c lines of the full symmetric *k*-space were zero-filled ($c \in [0, m/2]$). Images were then reconstructed using POCS iterative algorithm, in which iterations were repeated until mean square difference in entire sample between images at iteration i and i+1 was less than 1%. For sake of clarity, the resulting images are henceforth named PF-GESFID and PF-GESFID, where the acceleration factor is equal to $m/c = 8/5 = 1.6$. Again, PF versions of GESFID and GESFIDE composite images were compared in to their full-Fourier reference.

T_2^*-weighted images were continuously acquired during heating between 20 °C and 75 °C under optimized conditions of resolutions and contrast. This was done using the PF-GESFID protocol with $tGE_{1,2,3}$ = 15, 27.5, 40.1 ms. The other image parameters were: Cartesian encoding, TR = 2 s, flip angle (FA) = 80°, FOV = 64 x 64 mm², m = 256 and slice thickness = 2 mm, leading to a voxel volume of $0.25 \times 0.25 \times 2$ mm^3. The acquisition time was 1'46''.

3.3 RESULTS

Figure 1 shows the images with full *k*-space acquisition obtained at different tGE. GESFID differs from GESFIDE echo train by the reinforcement of susceptibility contrast due to the increase in T_2'-weighting with tGE. This reinforcement is more prominent at the highest spatial resolution (Fig. 1-B) because the inter-echo delay (i.e. tGE_{i+1} - tGE_i) increases with matrix size in the frequency-encoding horizontal (x) direction. For the same reason, there is a higher decrease in SNR at the highest spatial resolution because of a higher T_2 attenuation.

Figure 2 allows comparing the composite images reconstructed by combining three echoes obtained at different tGE and their reference reconstructed from the first GE of the train. Echo

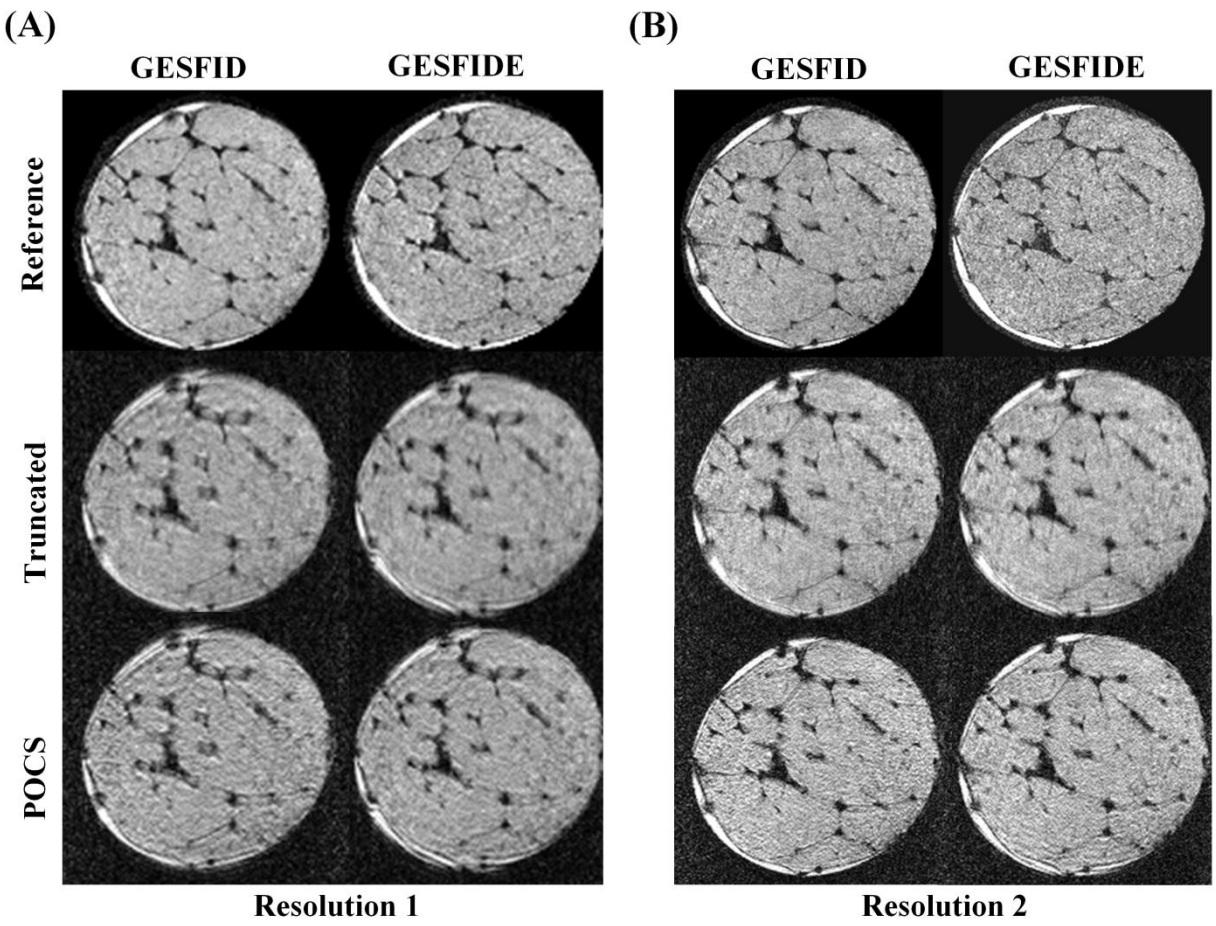

Figure 3: Effect of half Fourier truncation (5/8 of the full k-space) and POCS reconstruction on composite images obtained by echo combination for GESFID and GESFIDE and at two spatial resolutions.

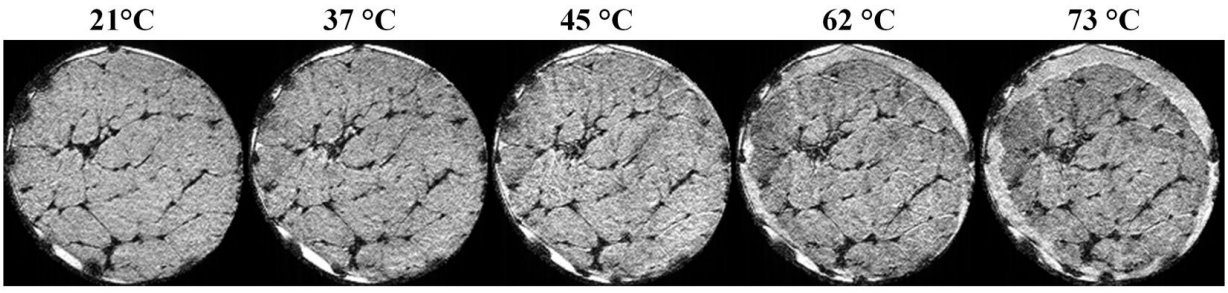

Figure 4: Follow-up of muscle evolution during heating using fast acquisition of susceptibility-weighted images (three GESFID echoes per TR, Half-Fourier and POCS reconstruction).

combination introduces blur at various degree in the composite images, and artifacts in the form of image details which either vanish or appear in the phase-encoding vertical y direction in both hypo- and hyper- intensities. The latter degradation is above all observed when GESFID echoes are combined and is visually awkward at the lowest spatial resolution (Fig. 2-A).

Figure 3 shows the effect of reducing the *k*-space to 5/8 on the composite images reconstructed by combining three echoes obtained at different tGE (i.e. those shown in Fig. 2). It highlights a SNR loss and a degradation of spatial resolution which is partly corrected by the use of POCS reconstruction.

Figure 4 shows several T_2^*-weighted images obtained during heating at 5 arbitrary chosen average temperature under optimized conditions of resolutions and contrast.

3.4 DISCUSSION

In the present work, we have developed solutions based on multiple GE acquisition for accelerating acquisition of T_2^*-weighted images. Figure 2 reveals artifacts in the composite image reconstructed from the three GESFID echoes. This is due to echo combination because such artifacts are not present in the original images (Fig. 1). First, it has been checked that there is no spatial shift in any direction between the GESFID images (data not shown). This does not mean that there is no spatial distortion in the frequency-encoding (x) direction due to off resonance conditions, but that there are the same for the different echo times. Actually, the shift cause by a frequency offset $\Delta\omega$ at a given (x, y) location in the latter direction is equal to $\Delta\omega/\gamma G_x$, where G_x is the gradient amplitude [14, 27] and therefore do not depend on tGE. In fact, we explain the observed artifacts due to echo combination by the phase offset $\Delta k = \Delta\omega . tGE$ which is accrued from the excitation in-phase moment. It shifts the "pseudo-echo" by Δk in the k_y direction proportionally to the echo time. In other words, the combined *k*-space results from lines which are shifted differently, in contrast to conventional images obtained at the same tGE for all lines (Fig. 1) for which the "pseudo echo" as a whole is shifted, which induce signal loss and phase modulation in the spatial domain. As increasing resolution in the phase-encoding direction is a generic solution for correcting such signal loss [14], it has the same beneficial effect when different GESFID echoes are combined because

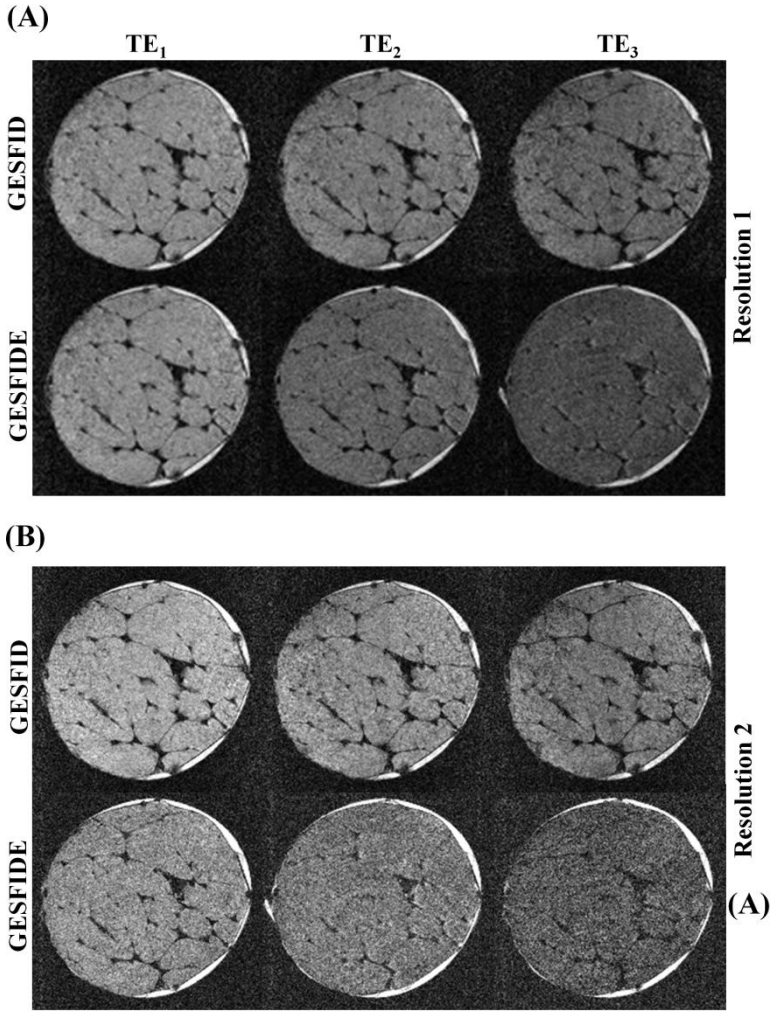

Figure 1: Susceptibility-weighted images of muscle obtained at three different echo times with GESFID and GESFIDE and at two spatial resolutions.

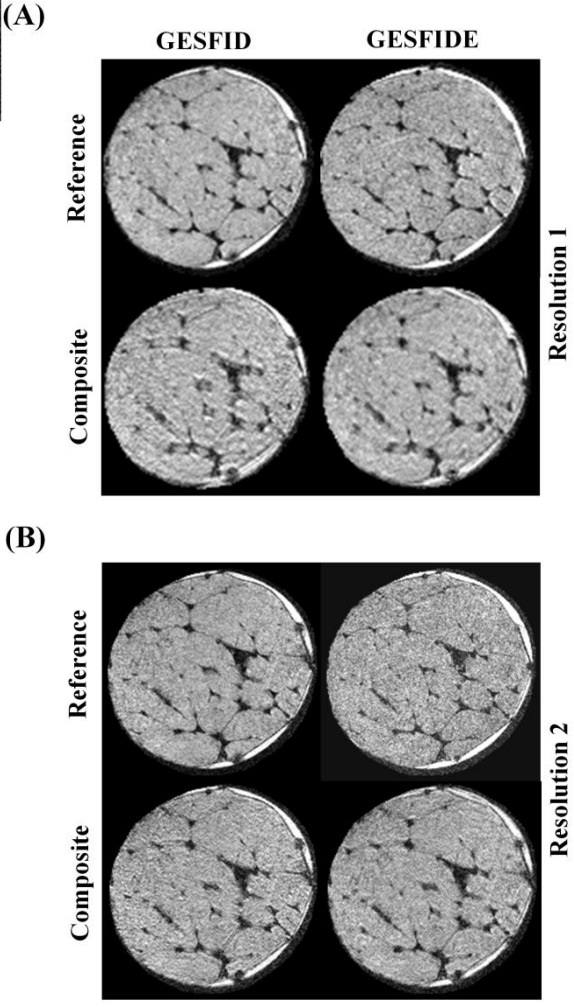

Figure 2: Effect of echo combination for GESFID and GESFIDE at two spatial resolutions. k-space is filled in a centric fashion, i.e. the first GE occupying the center of the resulting k-space and the last one the upper thirds.

Δk becomes small compared to the true position k_y when the stretch of *k*-space is larger. This explains why artifacts are less prominent at the highest spatial resolution (Fig. 2-B). In this respect, the combination of GESFIDE echoes is much less prone to off resonance effects (Fig. 2), even at low spatial resolution. On principle, the delays in between the in-phase moments (i.e. excitation and spin-echo refocusing) and acquisitions are the same for having with the same T_2'-weighting. The phase offset $\Delta k = \Delta\omega . tGE_1$ accrued during this delay is hence the same for the three echoes.

Even if the sensitivity to off resonance conditions is less for GESFIDE, the latter is disadvantaged by longer echo times compared to GESFID. Roughly speaking, by considering the same duration T_p for excitation and refocusing pulses, one can consider that $tSE \approx 4. tGE_1$. This leads to $tGE_2 \approx 3. tGE_1$ and $tGE_3 \approx 5. tGE_1$ for GESFIDE, instead of $tGE_2 \approx 3. tGE_1 - T_p$ and $tGE_3 \approx 5. tGE_1 - 2. T_p$ for GESFID. This highlights that the counterpart for obtaining a constant T_2'-weighting with GESFIDE is a higher T_2 attenuation. Because tGE_1 increases with spatial resolution in the frequency-encoding direction, T_2 attenuation is the main limiting factor of GESFIDE approach. Also, this is for this reason that GESFID was preferred for high resolution dynamic imaging of muscle during heating. We previously measured a T_2 decrease from 29 ms to 22 ms between 20 °C and 75 °C [23]. The SNR loss of late echoes of the GESFIDE train, already significant at 20 °C (Fig. 1-B), becomes too important at higher temperature. For GESFID and GESFIDE, T_2^* attenuation of echoes along k_y degrades spatial resolution in the corresponding vertical direction.

Further acceleration can be theoretically obtained by acquiring more than three echoes. In addition to the off resonance effects discussed before, GESFID is not well adapted for such lengthening of echo train because both reversible and irreversible spin dephasing cumulate for attenuating the echo train. Provided T_2 is not too short for maintaining sufficient SNR in the different echoes, GESFIDE is a better strategy for acquiring more than three echoes with a constant T_2' attenuation. It can also turn some previous developments to advantage for stabilizing spin-echo amplitudes and for reducing specific absorption rate by using a low refocusing angle [28-30].

It should be noted that Multi Echo Recalled Gradient Echo (MERGE) technique was proposed for combining multiple GE into an image [31, 32], thus following a principle close enough to the one developed here in GESFID. However, the objective of MERGE was not to accelerate image process but averaging full *k*-spaces obtained at different echo times for both

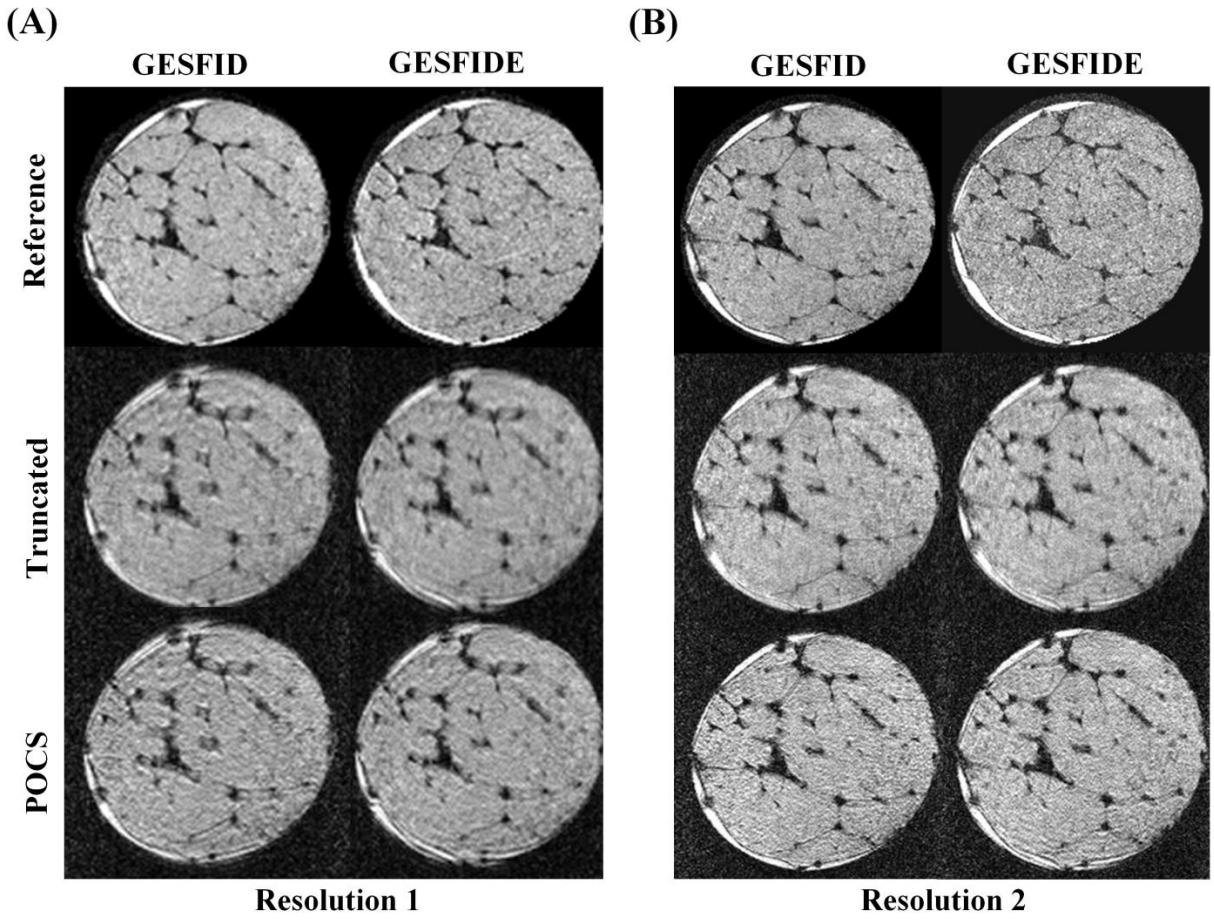

Figure 3: Effect of half Fourier truncation (5/8 of the full k-space) and POCS reconstruction on composite images obtained by echo combination for GESFID and GESFIDE and at two spatial resolutions.

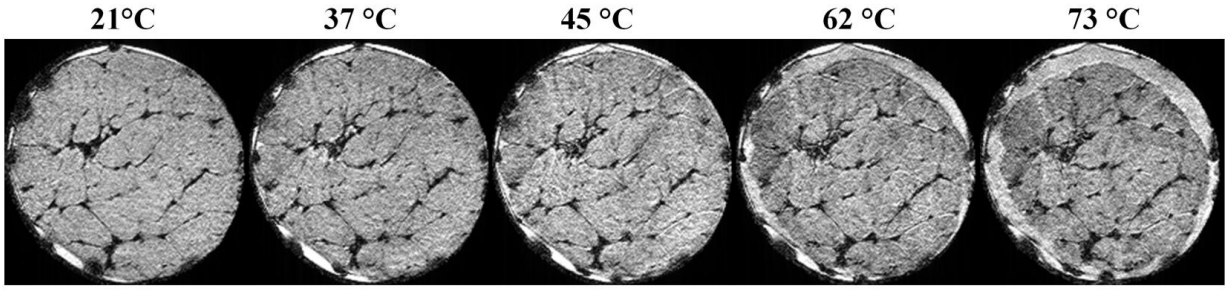

Figure 4: Follow-up of muscle evolution during heating using fast acquisition of susceptibility-weighted images (three GESFID echoes per TR, Half-Fourier and POCS reconstruction).

retaining a high SNR and increasing tissue contrast. It is possible to extend MERGE to a GESFIDE train in order to average images exhibiting the same T_2' -weighting. This should allow an accurate control of susceptibility contrast in the resulting MERGE images.

Our experimental results shows that half Fourier acquisition allows further accelerating the acquisition process. It also confirms that POCS reconstruction corrects some phase errors and reduces blurring in the resulting images (Fig. 3). Noted that other recent reconstruction methods are likely to further improve image quality acquired with partial *k*-space (e.g. [33]). Although incomplete, halving *k*-space has been considered here because it keeps an high-frequency information in the acquired *k*-space. For our dynamic imaging application which continuously repeats acquisitions, an alternative approach consists in refreshing high-frequency part of the *k*-space less frequently than the central part [34]. This was tested by continuously acquiring 4 sets with a reduced resolution in k_y direction (i.e. 64 centered lines) and by reconstructing the missing upper parts of *k*-space by linear interpolation of the high resolution *k*-spaces (i.e. 192 lines) which surrounded the quickly acquired datasets. While being acceptable for our practical application, this technique sacrifices some of the frequency information in the *k*-space. This induces an increase of the error with temperature when the interpolated image was compared to the one obtained from the full *k*-space [35], unlike to the HF-POCS method for which the error is nearly constant with temperature.

In spite of very unfavorable experimental conditions, i.e. heating, turbulent water circulation around the sample and evoluting NMR conditions [23], high-resolution susceptibility-weighted MRI were rapidly obtained using combination of GESFID echoes and half Fourier acquisition (Fig. 4). Image quality is comparable to the one obtained with the reference approach (single GE, full *k*-space) which is more than 4 times longer [15]). While assessing muscle deformation, a water network is revealed characterized by a hypersignal on the images. It corresponds to water migrating from myofibers owing to the contraction of the connective network, which then collects in the interfascicular space and then out of the meat.

3.5 CONCLUSION

We have described two methods for accelerating acquisition of high resolution susceptibility-weighted images. They are based on dispatching GE trains over the *k*-space. Two strategies

were tested and discussed which are based on the refocusing (GESFIDE) or not (GESFID) of the reversible part of the T_2^* decay. Because of a lesser inter-echo time, GESFID approach should be preferred for imaging short T_2 populations, but the spatial resolution should be high enough for limiting the artifacts due to off resonance conditions. Conversely, GESFIDE has the advantage of being not prone to the latter effects at the cost of a higher SNR loss due to T_2 attenuation. GESFID technique was applied successfully for depicting the rapid evolution of muscle structure during heating in spite of the T_2 shortening with temperature.

3.6 CITED REFERENCES IN ARTICLE 3

1. He X, Y DA (2009) Biophysical mechanisms of phase contrast in gradient echo MRI. Proc Natl Acad Sci USA 106:13558-13563.

2. Marques JP, Maddage R, Mlynarik V, Gruetter R (2009) On the origin of the MR image phase contrast: An *in vivo* MR microscopy study of the rat brain at 14.1 T. NeuroImage 46:345-352.

3. Duyn JH, Van Gelderen P, Li TQ, De Zwart JA, Koretsky AP, Fukunaga M (2007) High-field MRI of brain cortical substructure based on signal phase. Proc Natl Acad Sci USA 104:11796-11801.

4. Schäfer A, Wharton S, Gowland P, Bowtell R (2009) Using magnetic field simulation to study susceptibility-related phase contrast in gradient echo MRI. NeuroImage 48:126-137.

5. Wehrli FW (2007) Structural and functional assessment of trabecluar and cortical bone by micro magnetic resonance imaging. J Magn Reson Imaging 25:390-409.

6. Bonny JM, Laurent W, Renou JP (2000) Detection of susceptibility effects using simultaneous T_2^* and magnetic field mapping. Magn Reson Imaging 18:1125-1128.

7. Bonny JM, Laurent W, Labas R, Taylor R, Berge P, Renou JP (2001) Magnetic resonance imaging of connective tissue: a non-destructive method for characterising muscle structure. J Sci Food Agric 81:337-341.

8. Mills PH, Ahrens ET (2009) Enhanced positive-contrast visualization of paramagnetic contrast agents using phase images. Magn Reson Med 62(5):1349-1355.

9. Weisskoff RM, Zuo CS, Boxerman JL, Rosen BR (1994) Microscopic susceptibility variation and transverse relaxation: theory and experiment. Magn Reson Med 31(6):601-610.

10. Sukstanskii AL, Yablonskiy DA (2001) Theory of FID NMR signal dephasing induced by mesoscopic magnetic field inhomogeneities in biological systems 151:107-117.

11. Yablonskiy DA, Haacke EM (1994) Theory of NMR signal behavior in magnetically inhomogeneous tissues: the static dephasing regime. Magn Reson Med 32:749-763.

12. Haase A (1986) FLASH imaging: rapid NMR imaging using low flip angle pulses. J Magn Reson 67:258-266.

13. Haacke EM, Tkach JA, Parrish TB (1989) Reduction of T_2^* dephasing in gradient field-echo imaging. Radiology 170(2):457-462.

14. Reichenbach JR, Venkatesan R, Yablonskiy DA, Thompson MR, Lai S, Haacke EM (1997) Theory and application of static field inhomogeneity effects in gradient-echo imaging. J Magn Reson Imaging 7:266-279.

15. Bouhrara M, Clerjon S, Damez JL, Chevarin C, Portanguen S, Kondjoyan A, Bonny JM (2011) Dynamic MRI and thermal simulation to interpret deformation and water transfer in meat during heating. J Agri Food Chem 59:1229-1235.

16. Yudilevich E, Stark H (1987) Spiral sampling in magnetic resonance imaging-the effect of inhomogeneities. IEEE Trans Med Imag 6(4):337-345.

17. Wu B, Li W, Van Avram A, Gho SM, Liu C (2012) Fast and tissue-optimized mapping of magnetic susceptibility and T_2^* with multi-echo and multi-shot spirals. NeuroImage 59:297-305.

18. Mansfield P (1977) Multi-planat image formation using NMR spin echoes. J Phys C: Solid State Phys 10:55-58.

19. Hennig J, Nauerth A, Friedburg H (1986) RARE imaging: a fast imaging method for clinical MR. Magn Reson Med 3:823-833.

20. Ma J, Wehrli FW (1996) Method for image-based measurement of the reversible and ireversible contribution to the transverse-relaxation rate. J Magn Reson, Series B 111:61-69.$

21. Mulkern RV, Wong ST, Winalski C, Jolesz FA (1990) Contrast manipulation and artifact assessment of 2D and 3D RARE sequences. Magn Reson Imaging 8:557-566.

22. Jovicich J, Norris DG (1998) GRASE imaging at 3 Tesla with template interactive phase-encoding. Magn Reson Med 39:970-979.

23. Bouhrara M, Lehallier B, Clerjon C, Damez JL, Bonny JM (2011) Mapping of muscle deformation during heating: *in situ* dynamic MRI and non-linear registration. Magn Reson Imaging (In Press, DOI: 10.1016/j.mri.2011.10.002).

24. MacFall JR, Pelc NJ, Vavrek RM (1988) Correction of spatially dependent phase shifts for partial Fourier imaging. Magn Reson Imaging 6:143-155.

25. Finsterbusch J, Frahm J (2002) Half-Fourier single-shot STEAM MRI. Magn Reson Med 47:611-615.

26. Haacke EM, Lindskog ED, Lin W (1991) A fast, iterative, Partial-Fourier technique capable of Local Phase Recovery. J Magn Reson 92:126-145.

27. Hinks RS, Derbyshire JA, LeRoux P (1998) Virtual frequency encoding: archieving symmetry in *K*-space. Magn Reson Med 39:1019-1024.

28. Alsop DC (1997) The sensitivity of low flip angle RARE imaging. Magn Reson Med 37:176-184.

29. LeRoux P, Hinks RS (1993) Stabilization of echo amplitudes in FSE sequences. Magn Reson Med 30:183-190.

30. Hennig J, Scheffler K (2000) Easy Improvement of Signal-to-Noise in RARE-Sequences with Low Refocusing Flip Angles. Magn Reson Med 44: 983-985.

31. Vertinsky AT, Krasnokutsky MV, Augustin M, Bammer R (2007) Cutting-edge imaging of the spine. Neuroimaging Clin N Am 17(1):117-136.

32. Moseley ME, Liu C, Rodriguez S, Brosnan T (2009) Advances in Magnetic Resonance Neuroimaging. Neurol Clin 27(1):1-19.

33. Huang F, Lin W, Li Y (2009) Partial Fourier reconstruction through data fitting and convolution in k-space. Magn Reson Med 62:1261-1269.

34. Doyle M, Walsh EG, Blackwell GG, Pohost GM (1995) Block Regional Interpolation Scheme for *k*-space (BRISK): a rapid cardiac imaging technique. Magn Reson Med 33:163-170.

35. Bouhrara M, Clerjon S, Damez JL, Bonny JM (2010) *In situ* MR imaging of food during continous heating. The 17th International Society for Magnetic Resonance Conference 2010. Frienze/Italy.

4. Article 4 : Cartographie multicoupes du champ B_1 à l'aide d'impulsions sélectives

A ce stade, nous sommes capables de suivre d'une manière rapide l'évolution locale de la structure du muscle pendant le chauffage. Le lien entre la déformation obtenue par recalage des images RMN et la température obtenue par simulation numérique a été établi de manière robuste. Or, cette déformation température-dépendante engendre des transferts d'eau à l'intérieur et à l'extérieur de l'échantillon, la répartition finale de l'eau étant un déterminant important de la qualité des viandes cuites. Comme pour la déformation, la dernière étape consiste donc à mesurer dynamiquement la quantité d'eau par IRM afin de construire un modèle moyen entre température et quantité d'eau.

Par principe, la cartographie de densité de protons est influencée par les variations spatiales de l'amplitude du champ excitateur B_1 et du champ récepteur, qui sont équivalents (par réciprocité) lorsqu'une même antenne est utilisée en émission et en réception. Dans l'absolu, la cartographie de la densité de protons nécessite donc de connaitre la distribution spatiale du champ afin de corriger les biais des cartes paramétriques, notamment à haut champ où les hétérogénéités du champ B_1 sont plus prégnantes (Glover 1985, Bottomley 1978). Pour notre application où seule la variation de densité de protons est utile, la correction n'est nécessaire que si le champ B_1 évolue au cours de la cuisson. Or, sa distribution dépend de plusieurs facteurs variables pendant la cuisson comme les dimensions et propriétés diélectriques de l'échantillon et la fréquence de résonance. Il devient donc primordial de cartographier rapidement la distribution spatiale du champ B_1 de façon continue au cours du chauffage.

Nous avons choisi d'utiliser la méthode de référence appelée *double angle method* (DAM, Stollberger 1996) qui requiert deux images dont le rapport des amplitudes dépend uniquement de l'amplitude B_1 au prix d'un temps d'acquisition long. Une nouvelle méthode baptisée DAM-SP (pour *DAM with selective pulse*) a été développée pour accélérer l'acquisition de ces deux images. Elle est fondée sur l'utilisation d'impulsions sélectives pour restreindre la cartographie du champ B_1 à certaines coupes choisies *a priori* et s'affranchir ainsi d'un codage de l'ensemble de l'échantillon exhaustif et couteux en temps.

Les résultats montrent que les imprécisions liées à l'utilisation de ces impulsions peuvent être corrigées et que la méthode peut être optimisée pour atteindre une qualité de cartographie du

champ B_1 comparable à celle obtenue avec des acquisitions de référence 100 fois plus longues.

Ce travail est en impression dans *Magnetic Resonance in Medicine*.

B_1 mapping with selective pulses

Mustapha BOUHRARA and Jean-Marie BONNY*

UR370 Qualité des Produits Animaux, INRA, F-63122 Saint-Genès-Champanelle

Phone: +33-4- 73-62-41-52.

Fax: +33-4-73-62-40-89

E-mail: jean-marie.bonny@clermont.inra.fr

4.1 ABSTRACT

Knowledge of B_1^+ distribution is crucial for many applications, such as quantitative MRI. A novel method has been developed in order to improve the accuracy of the conventionally applied double-angle method for B_1^+ mapping. It solves the remaining issues raised by the use of selective pulses for slice selection in order to accelerate the acquisition process.

A general approach for reconstructing B_1^+ maps is presented first. It takes B_1^+-induced slice profile distortions over off-resonance frequencies into account. It is then shown how the ratio between the prescribed flip angles can be adjusted to reach a compromise between the level of noise propagated onto B_1^+ maps and the width of the range in which the field can be mapped. Lastly, several solutions are proposed for reducing the B_1^+-dependent pollution of regions distal to the image slice which participates significantly in the inaccuracy of B_1^+ mapping. These methods were experimentally tested by comparison with gold standard B_1^+ maps obtained on a phantom using a non-selective and thus much slower technique.

As they are independent and lead to significant improvements, these solutions can be combined to achieve high-precision and fast B_1^+-mapping using spin-echo DAM.

KEYWORDS: B_1^+ mapping; selective pulse; Shinnar-Le Roux algorithm; double-angle method; quantitative imaging

4.2 INTRODUCTION

Mapping the B_1^+ amplitude of the active emission field is necessary for many MRI applications, for example, for correcting errors in spin density (1, 2), quantitative T_1 (3, 4) and T_2 (5) maps, coil design (6, 7) and image reconstruction in transmit and receive parallel imaging. In practice, experimental mapping of B_1^+ is often preferred to numerical simulations because its distribution depends on unknown or evolving factors of the sample studied, such as shape, position relative to the coil(s) and dielectric properties (8). Furthermore, mapping becomes crucial for high field MRI since the spatial inhomogeneity of B_1^+ increases with static field strength, due to the reduction of RF field wavelength compared to sample size (9, 10).

Existing B_1^+ mapping methods are based on a one-parameter relationship between $\propto B_1^+$ and the MR image. Although original techniques based on image phase have been proposed recently (11,12), the most widely used methods are based on acquiring at least two magnitude images at different prescribed values for flip angles by using standard sequences (see the introduction of ref. (12) for a review of these methods). The first drawback of this conventionally applied double-angle method (DAM, 13) is its long acquisition time, due to the long repetition time (TR) required for mitigating T_1 dependence. This was circumvented by using EPI encoding (1, 14), the reset preparation scheme with spiral acquisition (15) and interleaved spoiled gradient echo imaging (16, 17).

In the present study we address other persistent issues raised by magnitude-based methods and by DAM in particular. The first issue has been underlined by several authors as a prominent source of errors on B_1^+ maps (16, 18-21), and it concerns their inaccuracy over a wide range of B_1^+ when selective pulses are used for slice selection. As a solution we propose to couple $\propto B_1^+$ and MR image amplitude, by taking such B_1^+-induced slice profile distortions over off-resonance frequencies into account, by numerical simulation of the evolution of the flip angle. The second issue concerns the level of propagated noise which is inherently significant when only two noisy images are acquired for fast B_1^+ mapping, as in DAM. We show here how the ratio between prescribed flip angles can be optimized for minimizing the level of propagated noise on B_1^+ maps obtained by spin-echo (SE) DAM. The last issue concerns the transverse coherence from outside the bandwidth of the selective pulse. B_1^+ inhomogeneities causes the flip angle to deviate from the value for which the pulse has been

optimized, increasing the contribution of out-of-bandwidth magnetization (OBM) in the total signal. This corresponds to a B_1^+-dependent pollution of regions distal to the imaged slice which can participate in inaccurate B_1^+ mapping. This point is addressed here by using an unconventional ratio of excitation, by refocusing angles in SE sequences and by making a pertinent choice of pulse shapes that minimize OBM.

4.3 THEORY

4.3.1 Extension of B_1^+ mapping using DAM for selective pulses

The initial methods (22-24) for mapping B_1^+ use hard RF pulses in order to take advantage of the linearity between B_1^+ and flip angles, assuming that γB_1^+ is much stronger than the off-resonance dispersion in the sample (25). To speed up the acquisition process, it is natural to replace each hard RF pulse by a soft RF pulse combined with a magnetic field gradient. By using such selective pulses, the longitudinal field corresponding to off-resonance effects cannot be neglected in comparison to the amplitude of the shaped pulse RF field throughout its time course. For the sake of accuracy, the flip angle α produced by any selective pulse should be described by its own non-linear dependence on the off-frequency ω and amplitude γB_1^+ of the pulse. To do this, simulations of Bloch equations were performed to obtain the flip angle as a function of ω and γB_1^+ using $\alpha(\omega; \gamma B_1^+) = \arccos\left(M_z(\omega; \gamma B_1^+)\right)$, where M_z is the amplitude of longitudinal magnetization. Provided that the in-slice dephasing of transverse magnetization $\mathbf{M}_{xy}$ due to selective excitation is compensated, the amplitude of transverse magnetization can be calculated by

$$M_{xy}(\gamma B_1^+) = \int M_{xy}(\omega; \gamma B_1^+)\, d\omega. \qquad [2]$$

Although this approach is applicable to any sequence, here we address only the case of the SE sequence because it is less prone to susceptibility artifacts than gradient-echo sequences, especially when echo-planar encoding has to be introduced to further accelerate the acquisition process. Neglecting relaxation and diffusion, M_{xy} for SE is given by (26)

$$M_{xy}^{SE}(\omega;\ \gamma B_{1,exc}^+, C) = M_0 E_2 \sin\alpha(\omega;\ \gamma B_{1,exc}^+) \sin^2\left(\beta(\omega; C\,\gamma B_{1,exc}^+)/2\right) \quad [3]$$

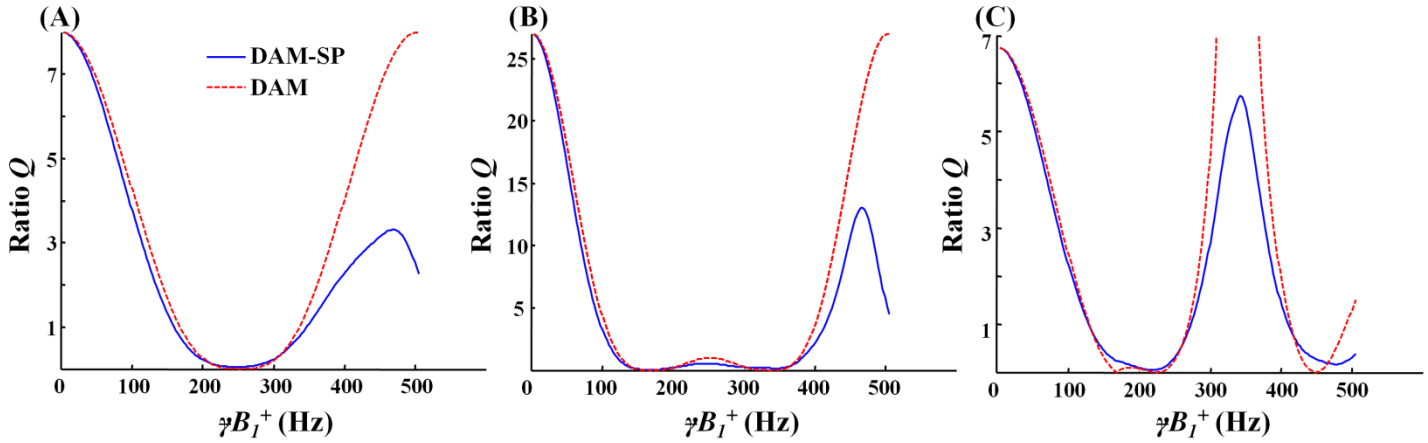

Figure 1: Ratio Q between two SE images as a function of γB_1^+ for three different sets of K, C_1 and C_2 (A) K = 2, C_1 = C_2 =2 (B) K = 3, C_1 = C_2 = 2 (C) K = 3, C_1 = 3 and C_2 = 1.5. It was calculated for excitation and refocusing shaped pulses of the same bandwidth (= 1 kHz) and duration (= 4.096 ms) which were generated using the Shinnar-LeRoux algorithm with in-slice and out-of-slice ripples of 1%. The two curves correspond to Q obtained by taking pulse profiles into account and to that derived by considering ideal square pulses.

where α and β are the excitation and the refocusing flip angles respectively, C the ratio between the amplitudes of the excitation and refocusing soft pulses (i.e. $C = B_{1,ref}^{+}/B_{1,exc}^{+}$), and M_0E_2 the product of equilibrium magnetization and T_2-weighting. After computing Eq. [2], the signal amplitude is obtained as a function of B_1^+ for any pair of soft pulses.

The principle of DAM is to couple the B_1^+ desired with ratio Q between two magnitude images obtained with different nominal flip angles. These angles differ by factor K ($K > 1$) chosen *a priori* which is a degree-of-freedom of DAM. As they are multiplicative and insensitive to flip angle values, the dependences on receiver coil sensitivity and M_0E_2 are cancelled by calculating Q, together with T_1-weighting, provided the non-steady state condition is fulfilled (TR $\geq$ 5 T_1). Consequently, Q depends only on B_1^+ of the emission coil as

$$Q\left(\not{\gamma}B_1^+; K, C_1, C_2\right) = \int M_{xy}^{SE}\left(\omega; K\not{\gamma}B_1^+, C_2\right) d\omega / \int M_{xy}^{SE}\left(\omega;\ \not{\gamma}B_1^+, C_1\right) d\omega$$

$$= M_{xy}^{SE}\left(K\not{\gamma}B_1^+, C_2\right) / M_{xy}^{SE}\left(\not{\gamma}B_1^+, C_1\right), \qquad [4]$$

where C_1 and C_2 are the respective C-ratios of the two images. To calculate B_1^+ voxelwise, Q was first computed for a large range of $\not{\gamma}B_1^+$. As ratio Q_{exp} was mapped experimentally from two magnitude images, B_1^+ was estimated using a 1D linear interpolation i.e.

$$Q_{interp}\left(\not{\gamma}\hat{B}_1^+; K\right) = Q_{exp}. \qquad [5]$$

For the sake of clarity, this new approach is henceforth referred to as DAM-SP (i.e. DAM which takes into account the effects of $\not{\gamma}B_1^+$ variations on Selective Pulses).

Figure 1 shows several regions in which there is a one-to-one relationship between Q and B_1^+, and therefore in which B_1^+ can be mapped, provided the nominal value $\not{\gamma}B_{1,nom}^+$ is well prescribed in the chosen region. The number and characteristics of these regions depend on the choice of the degrees-of-freedom K, C_1 and C_2, available for many B_1^+ mapping protocols using DAM-SP. For example, there are two bijective regions (centered at 125 Hz or 44.5° and 360 Hz or 128.5°) ranging from 0 to 480 Hz for $K = C_1 = C_2 = 2$ (Fig. 1-A), whereas there is one more bijective region (centered at 100.5 Hz or 39.5°, 282 Hz or 100.5°, and 411 Hz or 146.5°) in nearly the same range for the unconventional K = 3 and $C_1 = 3$, $C_2 = 1.5$ (Fig. 1-C).

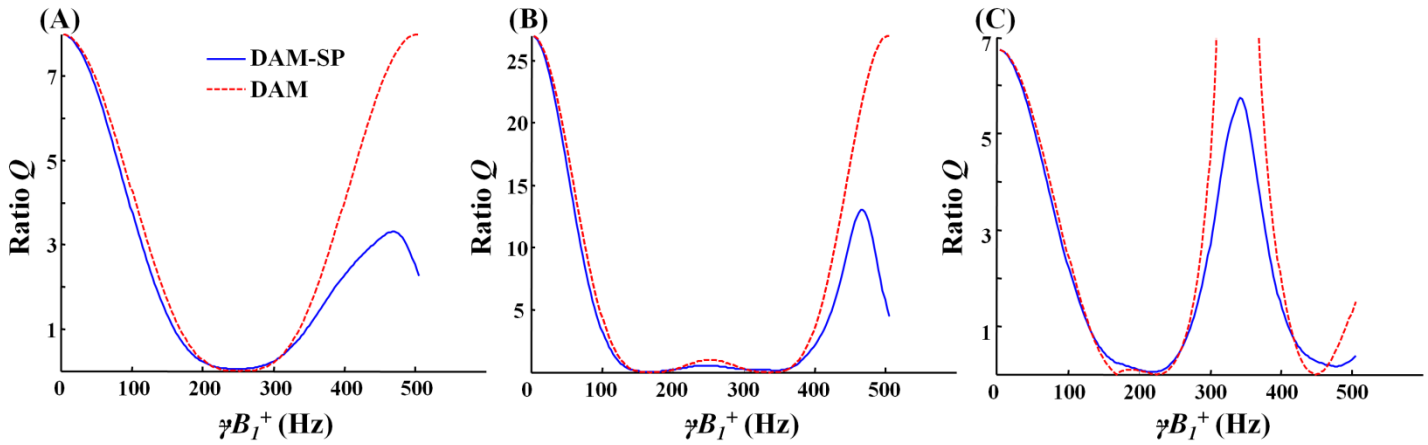

Figure 1: Ratio Q between two SE images as a function of γB_1^+ for three different sets of K, C_1 and C_2 (A) K = 2, C_1 = C_2 =2 (B) K = 3, C_1 = C_2 = 2 (C) K = 3, C_1 = 3 and C_2 = 1.5. It was calculated for excitation and refocusing shaped pulses of the same bandwidth (= 1 kHz) and duration (= 4.096 ms) which were generated using the Shinnar-LeRoux algorithm with in-slice and out-of-slice ripples of 1%. The two curves correspond to Q obtained by taking pulse profiles into account and to that derived by considering ideal square pulses.

4.3.2 Expression of noise propagated onto the B_1^+ map using DAM-SP

As the non-linear correspondence between Q and B_1^+ depends on K (Fig. 1), it is necessary to study how noise will propagate onto the B_1^+ map. Assuming that the noise corrupting both images has the same variance σ^2, the variance of Q fluctuations is approximated by (27)

$$\sigma_Q^2 = \left(\left[\frac{\partial Q}{\partial M_{xy}^{SEQ}(K \not\propto B_1^+)} \right]^2 + \left[\frac{\partial Q}{\partial M_{xy}^{SEQ}(\not\propto B_1^+)} \right]^2 \right) \sigma^2 \qquad [6]$$

$$= \frac{M_{xy}^{SEQ}(\not\propto B_1^+)^2 + M_{xy}^{SEQ}(K \not\propto B_1^+)^2}{M_{xy}^{SEQ}(\not\propto B_1^+)^4} \sigma^2$$

The variance of the noise propagated onto the B_1^+ map is given by

$$\sigma^2_{\not\propto B_1^+} = \left(\frac{\partial Q}{\partial \not\propto B_1^+} \right)^{-2} \sigma_Q^2$$

$$= \left(\frac{\partial Q}{\partial \not\propto B_1^+} \right)^{-2} \left[\frac{M_{xy}^{SEQ}(\not\propto B_1^+)^2 + M_{xy}^{SEQ}(K \not\propto B_1^+)^2}{M_{xy}^{SEQ}(\not\propto B_1^+)^4} \right] \sigma^2$$

[7]

Finally, we introduce the following merit factor Γ which is inversely proportional to the level of noise propagated onto the B_1^+ map

$$\Gamma = \left(\sqrt{\frac{\sigma^2_{\not\propto B_1^+}}{\sigma^2}} \right)^{-1} = \left| \frac{\partial Q}{\partial \not\propto B_1^+} \right| \frac{M_{xy}^{SEQ}(\not\propto B_1^+)^2}{\sqrt{M_{xy}^{SEQ}(\not\propto B_1^+)^2 + M_{xy}^{SEQ}(K \not\propto B_1^+)^2}}$$

[8]

Using the latter expression, each region of $Q(\not\propto B_1^+; K, C_1, C_2)$ can be characterized by its level of propagated noise by averaging Γ over the range of $\not\propto B_1^+$ in which Q is bijective. The relative width of this range and the corresponding mean $\bar{\Gamma}$ provide two quantitative factors which should be maximized simultaneously to optimize the B_1^+ mapping protocol.

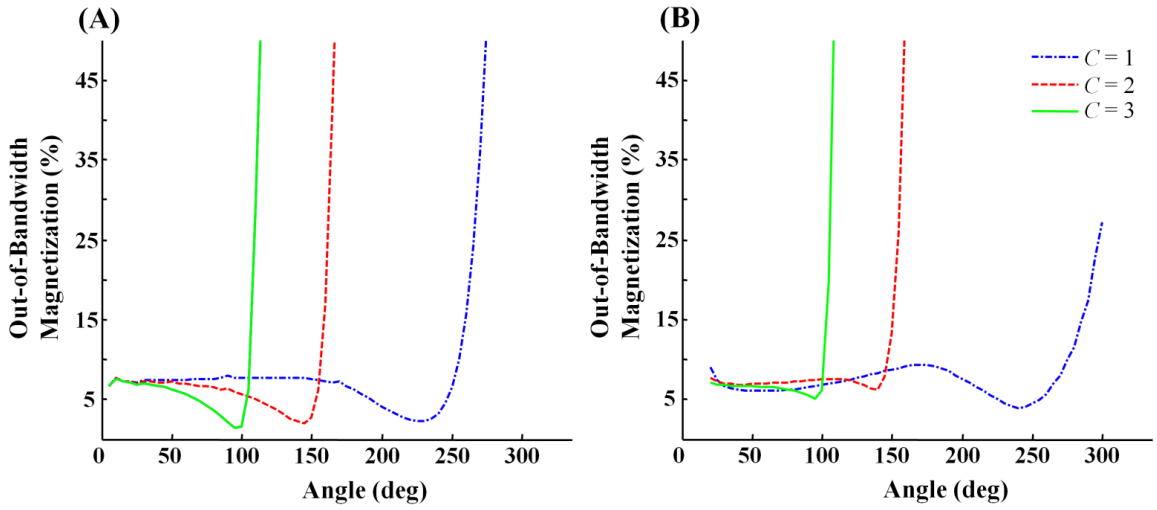

Figure 2: Relative contribution of out-of-bandwidth magnetization in the total SE signal for different ratios C between excitation and refocusing angles obtained from (A) simulations and (B) experiments. SE profiles were produced by a pair of Shinnar-LeRoux pulses (TB = 2.048 ms x 1 kHz, in-slice and out-of-slice ripples of 1%).

4.3.3 Errors due the signal from outside the nominal pulse bandwidth

Most of selective pulses are designed for inducing a given profile at a nominal on-resonance angle. Any difference from this nominal level distorts pulse profile (28) which therefore introduces a contribution of OBM in the total signal. OBM is another source of B_1^+ mapping inaccuracy because $\not\propto B_1^+$ values vary with distance to the image slice.

For the SE sequence, OBM results from the out-of-bandwidth distortions of both excitation and refocusing pulses. Figure 2-A shows the relative OBM signal as a function of the excitation flip angle for conventional SE ($C = 2$) obtained by simulations. OBM depends on $\not\propto B_1^+$ and the increases at the both sides of the minimum are asymmetric. This means that OBM-related inaccuracy can be minimized by prescribing $\not\propto B_{1,nom}^+$ on the left of this minimum in order to prevent B_1^+-inhomogeneities from leading to excitation angles larger than 150°, for which OBM increases rapidly. Figure 2 also shows that changing the ratio between excitation and refocusing angles allows shifting the minimum OBM towards lower or higher excitation angles. This is a solution for minimizing OBM by adjusting C_1 and C_2 to the nominal angles prescribed for acquiring the two SE images necessary for the DAM-SP protocol.

4.4 MATERIALS AND METHODS

4.4.1 Validation of the model integrating pulse profiles

Investigations were performed on a Biospec horizontal 4.7 T MRI system (Bruker GmbH, Ettlingen, Germany), with a 26 cm diameter bore, equipped with a BGA-26 gradient system and using a linear polarized birdcage coil for both emission and reception.

All numerical procedures were performed with Matlab (MathWorks Inc., Natick, USA).

Models of SE amplitude ($C = 2$) as a function of B_1^+ were assessed by comparing computed signals to experimental ones obtained on a homogeneous phantom with a sequence integrating selective pulses. The first model did not take pulse profiles into account ($M_{xy}^{SE} \propto \sin^3$) whereas the second one did, by using Eq. [1,2] and bounds of integration equal to the pulse bandwidth. The phantom was a cylinder 15 cm in diameter made of gelatin ($T_1 \approx 350$ ms and $T_2 \approx 40$ ms). A pair of selective pulses of the same duration and bandwidth (TB = 4.096 ms x

1 kHz, in-slice and out-of-slice ripples of 1%) was used with the Shinnar-LeRoux transform (SLR, 29) implemented under Matpulse 2.0 (28). The other image parameters were: spin-warp encoding, TR = 2500 ms, TE = 14.6 ms, FOV = 160 x 160 mm², matrix = 100 x 100 and slice thickness = 4 mm. The accuracy of the theoretical model was quantified by computing the relative fitting error between theoretical and experimental signals voxelwise over the phantom (i.e. the mean of the absolute residuals over 28 different values of $\not\propto \mathrm{B}_1^+$ divided by the mean of experimental magnitudes).

Flip angle distributions produced by shaped pulse as a function of off-resonance frequencies were obtained numerically using Bloch equations for any $\not\propto \mathrm{B}_1^+$ (to which corresponds a specific on-resonance flip angle), neglecting relaxation and assuming the piece-wise constant amplitude of $B_1^+(t)$ field (25).

4.4.2 Validation and optimization of B_1^+ mapping using DAM-SP

First, DAM-SP and original DAM reconstruction methods were compared. To do this, the same pair of SE images obtained on the homogeneous gelatin phantom were used with $K = C_1 = C_2 = 2$. The nominal $\not\propto B_{1,nom}^+$ for the excitation pulse of the first reference image was set to the value for which merit factor Γ is maximum (i.e. 171 Hz or 61°). The parameters of the SLR pulse pair used were: TB = 4.096 ms x 1 kHz, in-slice and out-of-slice ripples of 1%. The other image parameters used for all SE acquisitions were: spin-warp 2D encoding, TR = 2500 ms, TE = 14.6 ms, FOV = 160 x 160 mm², matrix = 160 x 160 and slice thickness = 6 mm. The look-up tables linking Q and B_1^+ were computed prior to the voxelwise estimation of $\not\propto \hat{B}_1^+$ (Eq. [5]).

Next, the effect of K on B_1^+ maps was analyzed. The merit factor Γ was first computed for different values of K as a function of the nominal $\not\propto B_{1,nom}^+$ and for the SLR pulse pair with TB = 4.096. Furthermore, two SE pairs were acquired for B_1^+ mapping with K = 1.5 and 3, $\not\propto B_{1,nom}^+$ with the first image being set to their optimal levels equal to α_1 =77° (216 Hz) and 44° (123 Hz) respectively. It should be noted that C_1 and C_2 were kept constant to 2 in both cases.

All the B_1^+ maps were compared to a gold standard. The latter was obtained by DAM using a spin-warp 3D encoding sequence, which acquires the FID response of the fully relaxed longitudinal magnetization. The shortest hard pulse (duration = 0.5 ms) was used for

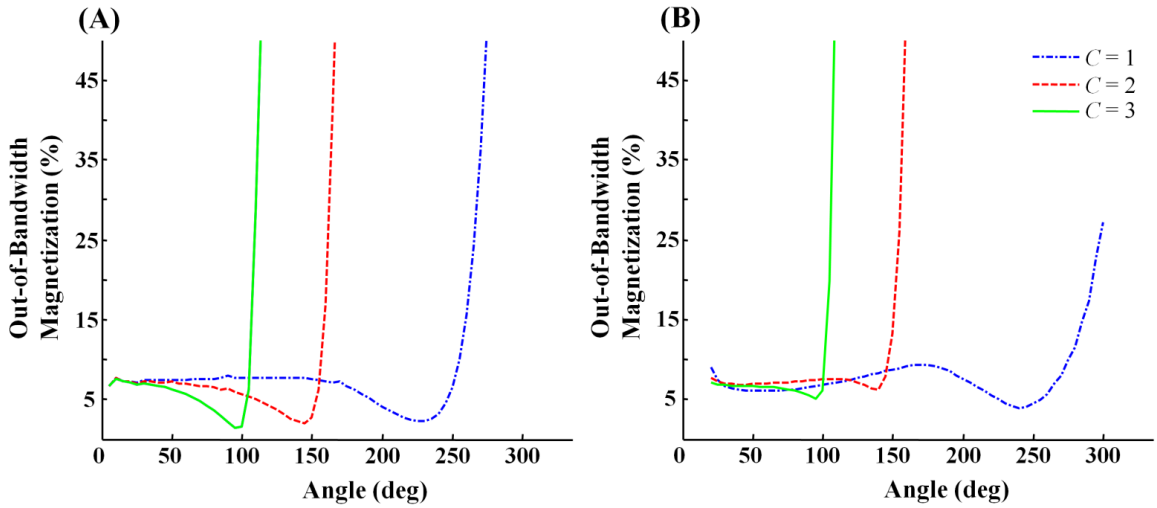

Figure 2: Relative contribution of out-of-bandwidth magnetization in the total SE signal for different ratios C between excitation and refocusing angles obtained from (A) simulations and (B) experiments. SE profiles were produced by a pair of Shinnar-LeRoux pulses (TB = 2.048 ms x 1 kHz, in-slice and out-of-slice ripples of 1%).

excitation, ensuring that γB_1^+ is much stronger than the off-resonance dispersion in the whole phantom for the two prescribed angles, $\alpha_1 = 60°$ and $\alpha_2 = 120°$. The other image parameters were: TR = 2500 ms, TE = 2.4 ms, FOV = 160 x 160 x 60 mm^3, matrix = 160 x 160 x 60, leading to an isotropic voxel volume of 1 mm^3. Before the reconstruction of B_1^+ map, 6 contiguous slices were averaged for perfect registration with the thicker slice imaged by 2D sequences.

B_1^+ maps were first normalized to obtain the same amplitude in a region-of-interest centered in the phantom, and then compare maps obtained with different prescribed angles. The mean relative error (i.e. the voxelwise $100 \times \left(\gamma \hat{B}_1^+ / \gamma B_{1,gold\ standard}^+ - 1 \right)$) was represented as a function of γB_1^+ in the form of a Bland and Altman plot (30). In addition, Lin's concordance correlation coefficient ρ_c (31) was calculated as a global index of agreement.

Assuming the profile of the coil to vary smoothly, noise maps N were inferred by image processing in order to emphasize noise propagated onto B_1^+ map (32) using $N = g * B_1^+ - B_1^+$, where g was a Gaussian filter of size 3 x 3.

4.4.3 Minimization of the signal outside the nominal pulse bandwidth

In order to confirm the simulations shown in Figure 2-A, SE profiles of the SLR pulse pair with TB = 2.048 were measured as a function of the excitation flip angle for three values of C. It consisted in acquiring a single SE, read out by the same gradient as that used during excitation and refocusing to obtain direct one-to-one mapping of the SE profile in the frequency domain ranging from -5 to 5 kHz. Relative OBM resulted from numerical integration over the frequencies outside the bandwidth of pulses.

The adjustment of C_1 and C_2 was the first solution tested for reducing OBM dependent on B_1^+ maps. The SE pair was acquired with the optimized parameters K = 3, C_1 = 3 and C_2 = 1.5, $\gamma B_{1,nom}^+$ of the first image set to α_1 = 49° (137.5 Hz). The strategy for obtaining these parameters is discussed further on.

In addition, complementary solutions were addressed by changing pulse shapes. SLR pulses produce repetitive and constant patterns inside the rejection band, which is able to generate OBM far from the selected slice. In contrast, a Gaussian-shaped pulse is characterized by a continuous decrease of the signal with off-resonance in the rejection band. This is why B_1^+ was mapped with conventional $K = C_1 = C_2 = 2$ but using two other pulse pairs; SLR

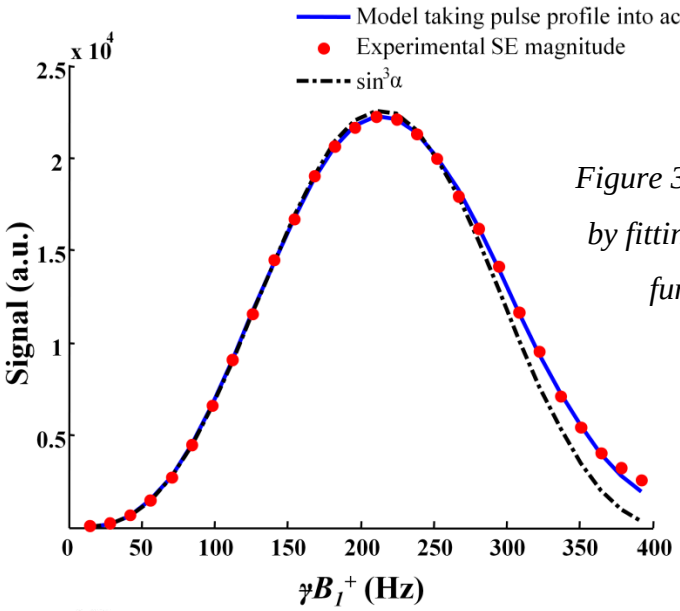

Figure 3: Comparison of theoretical models by fitting experimental SE amplitudes as a function of γB_1^+ in a given voxel.

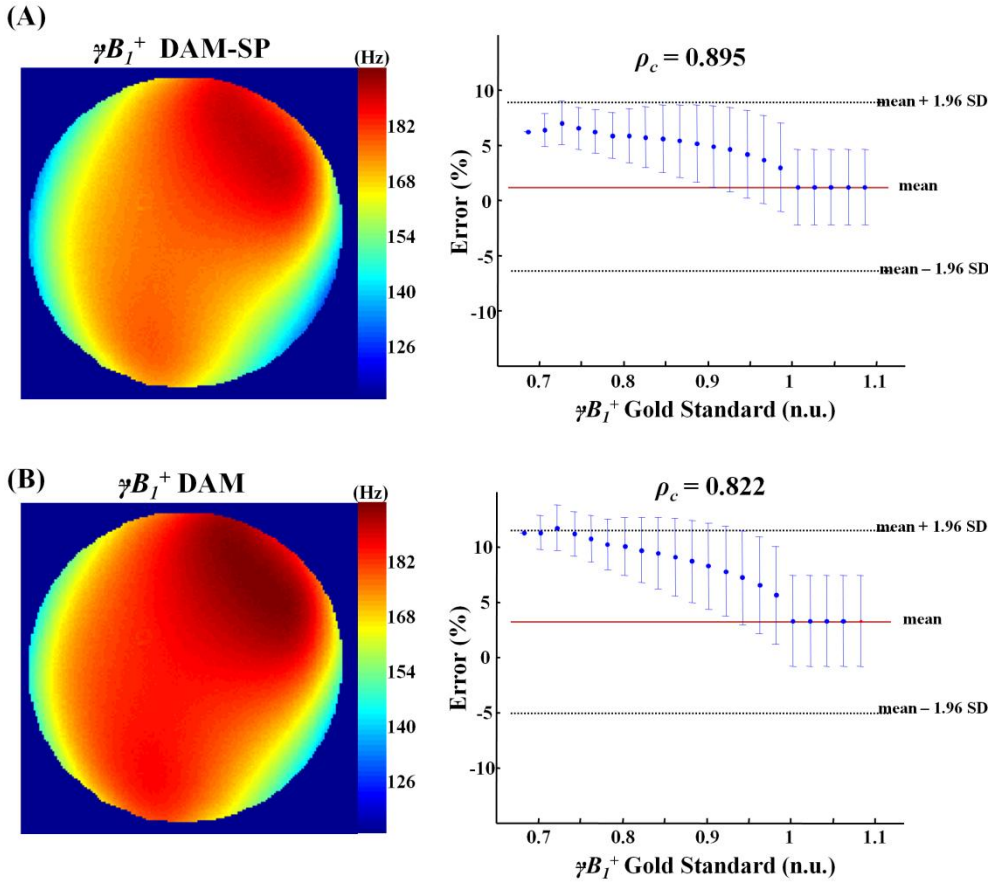

Figure 4: (Left) B_1^+ maps derived from the same acquisitions of a homogeneous phantom with $K = C_1 = C_2 = 2$ using (A) DAM-SP and (B) DAM. (C) Gold standard B_1^+ map. (Right) Respective Bland and Altman plots.

pulses with TB = 4.096 generated with the out-of-slice ripple reduced by a factor 100 (0.01%) and Gaussians with TB = 2.74 ms x 1 kHz.

4.5 RESULTS

4.5.1 Validation of the theoretical model

Figure 3 compares the experimental SE magnitudes in a voxel as a function of $\measuredangle B_1^+$ with fitted models obtained with and without taking pulse profiles into account. When the effects of selective pulse profiles are neglected, the deviations between experimental and theoretical values are substantial because both excitation and refocusing errors cumulate for SE, especially for large $\measuredangle B_1^+$, i.e. excitation angle above 110°. As expected, even if the voxel was chosen in a region of B_1^+-hyperintensity, our numerical model of pulse profiles fits perfectly with the experimental values for the whole range of excitation angles. Quantitative evaluation of the fitting error between the experimental measurements and theoretical models leads to an average error of 1.0 ± 1.1% in the entire phantom when the pulse profiles were taken into account in the model, instead of 4.9 ± 6.2% for the rough $\sin^3$ model.

4.5.2 Optimization and validation of B_1^+ mapping by using DAM-SP

Figure 4 shows B_1^+ maps obtained from the same pair of images, but after DAM and DAM-SP reconstructions. Quantitative analysis indicates that DAM-SP is clearly better than DAM by both decreasing bias and errors as a function of $\measuredangle B_1^+$, and increasing the factor of agreement ρ_c.

Figure 5-A presents merit factor Γ as function of $\measuredangle B_1^+$ for three values of K. It highlights that for each K, there is an optimal value of $\measuredangle B_1^+$ for which merit factor Γ is maximal. This value is located in the first peak which has the advantage of requiring less RF power than the next peaks and for which there is bijectivity between Q and $\measuredangle B_1^+$. It also highlights that increasing K improves merit factor Γ to the detriment of peak width. Figure 5-B validates this decrease of propagated noise onto B_1^+ maps for increasing K. It also leads to a slight improvement of the concordance index (0.891, 0.895, 0.897 for $K = 1.5,\ 2,\ 3$ respectively).

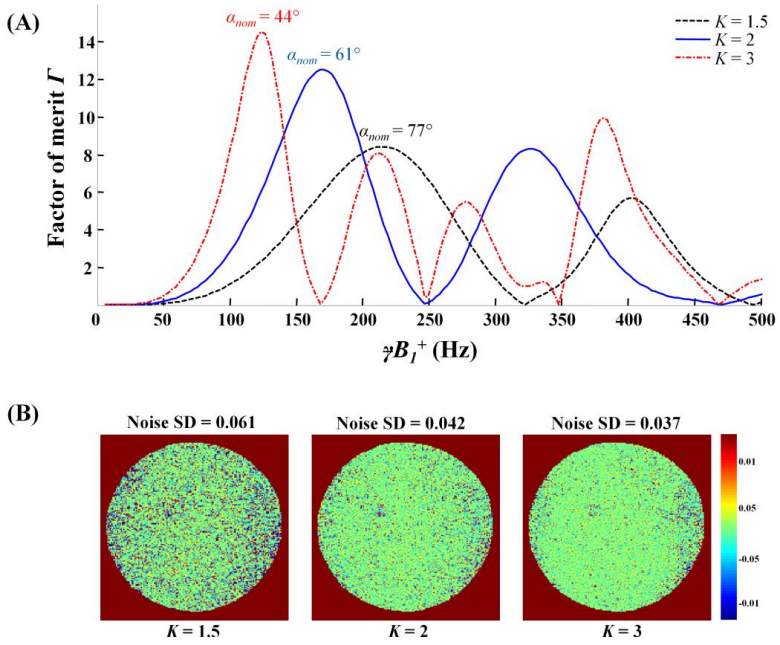

Figure 5: (A) Factor of merit Γ as a function of γB_1^+ for three values of K (B) Maps of noise propagated onto B_1^+ maps for the same values of K.

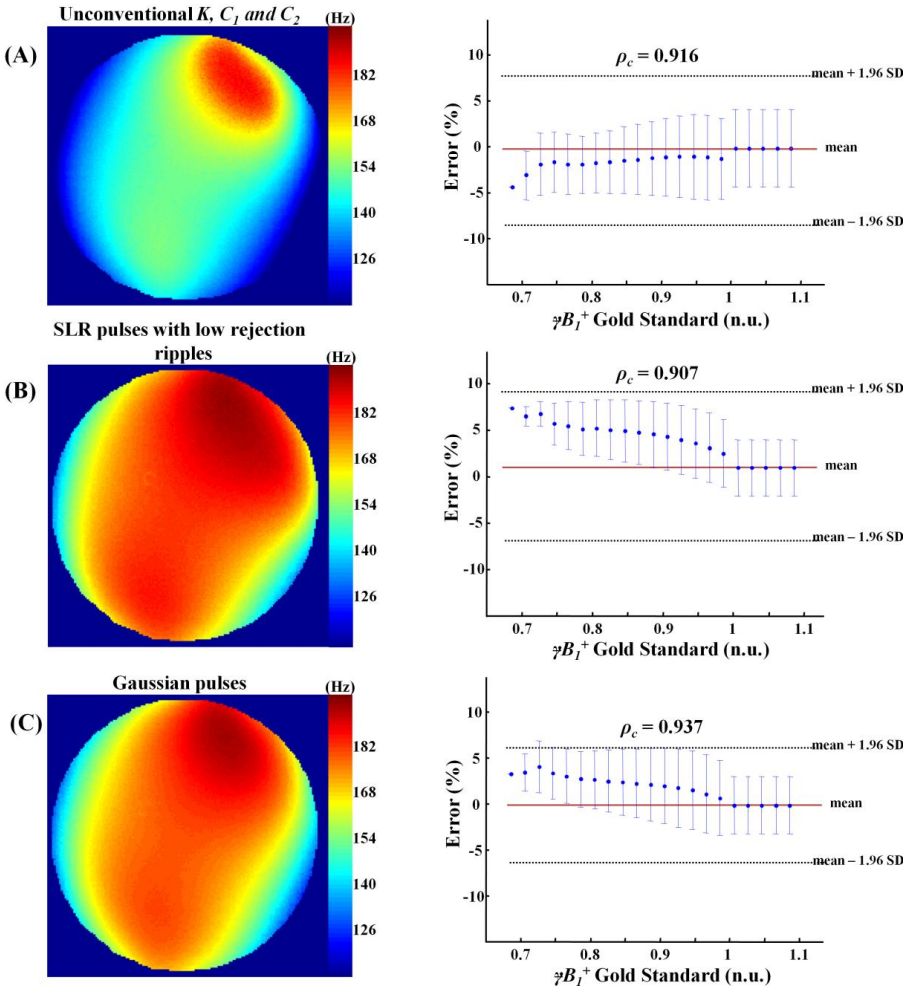

Figure 6: (Left) B_1^+maps obtained by DAM-SP with different strategies for reducing OBM-dependent inaccuracies (A) K = 3, C_1 = 3, C_2 = 1.5 (B) SLR pair with rejection ripple = 0.01% (C) Gaussian pair. (Right) Respective Bland and Altman plots.

4.5.3 Minimization of signal outside the nominal pulse bandwidth

Both the simulations and experimental results shown in Figure 2 exhibit a considerable increase in OBM for large flip angles. The angle for which OBM is minimum changes with C, with a higher value shifting towards a lower angle, and conversely. An effect of moving average is found when comparing Figure 2-B to Figure 2-A. This can be explained by the non-localized technique used for measuring profile which averages signals from magnetizations processed at the same off-resonance frequency, but resulting from different flip angles due to the spatial B_1^+-inhomogeneities in the phantom.

Figure 6 shows the efficiency of the three strategies used for reducing OBM-dependent errors. They lead, at varying degrees, to B_1^+-maps with better accuracy compared to the reference shown in Figure 4-A.

4.6 DISCUSSION

We propose a method of correcting some DAM inaccuracies regarding slice profile B_1^+-dependence. It is based on a computational procedure which consists in calculating the flip angle by interpolating a stringent bi-dimensional sampling of $\alpha(\omega; \not\propto B_1^+)$ obtained by Bloch simulation. The numerical model given by Eq. [2,3] fits well with the flip angle behavior, even for large angles, and it results in better accuracy of B_1^+-map obtained by DAM-SP. While requiring heavy calculation burden, the computation of look-up table Q can be done prior to the faster reconstruction of B_1^+-map, and for any pulse pair. The amplitude of bias corrected by DAM-SP corresponds to the shift between the two Q-curves obtained for DAM and DAM-SP shown in Figure 1. Although this bias can be fortuitously low for some specific experimental parameters, it is preferable to systematically perform DAM-SP reconstruction to avoid any bias introduced by slice profile B_1^+-dependence.

Factor of merit Γ presenting several peaks as a function of $\not\propto B_1^+$ (Fig. 5-A), reveals that the sensitivity to $\not\propto B_1^+$ variations is far from constant, and that $\not\propto B_{1,nom}^+$ should therefore be chosen with care, close to a maximum of Γ. It is not certain however that this prescription will correspond to the effective value emitted by the coil in the regions-of-interest, because most practical calibration protocols are global and prone to inaccuracies. We used an alternative

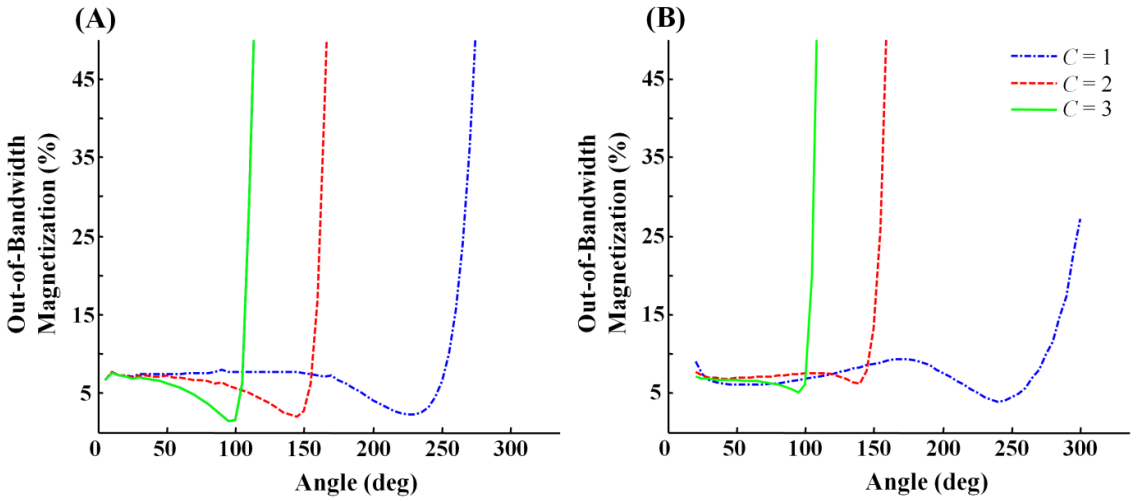

Figure 2: Relative contribution of out-of-bandwidth magnetization in the total SE signal for different ratios C between excitation and refocusing angles obtained from (A) simulations and (B) experiments. SE profiles were produced by a pair of Shinnar-LeRoux pulses (TB = 2.048 ms x 1 kHz, in-slice and out-of-slice ripples of 1%).

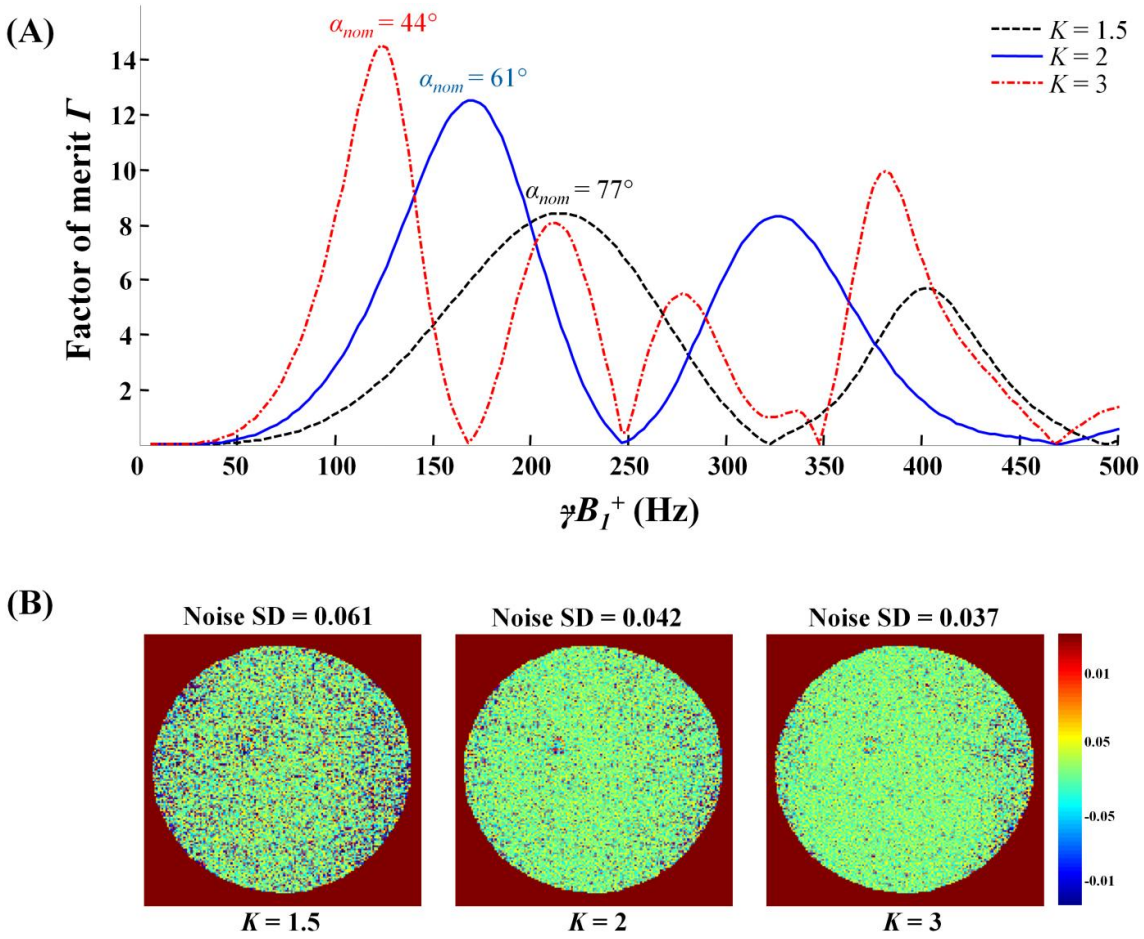

Figure 5: (A) Factor of merit Γ as a function of $\gamma B1^+$ for three values of K (B) Maps of noise propagated onto γB_1^+ maps for the same values of K.

procedure which consists in mapping $\not\propto B_1^+$ with DAM-SP in the regions-of-interest beforehand, in order to measure the difference between prescribed and effective $\not\propto B_1^+$ levels, and to eliminate this difference for the next acquisitions.

Until now, DAM was mostly documented with K set at 2, probably because of the simple algebraic relationship between $\not\propto B_1^+$ and ratio Q in this case, which therefore facilitates the estimation of $\not\propto B_1^+$ from Q_{exp} values. Nonetheless, it is shown here that increasing K leads to a decrease of propagated noise to the detriment of the dynamic range. This provides an interesting degree-of-freedom for adapting the sensitivity and dynamic range of the method to $\not\propto B_1^+$-inhomogeneity in the region-of-interest. A large K is useful for mapping a homogeneous B_1^+-field and a low K for a more inhomogeneous one. Increasing K also multiplies the number of regions in which Q is bijective, and then where the B_1^+-field can be mapped (Fig. 5-A). In most situations, it is recommended to select that leading to a low $\not\propto B_{1,nom}^+$ for the practical reason that it requires less RF power and benefits from a higher dynamic range.

If DAM-SP works for any pulse pair, the characteristics of pulse shapes have to be considered in the design of the B_1^+-mapping protocol. SLR pulses were preferred due to the ability of the SLR transform to prescribe TB, the current gauge of pulse performance, and the in-slice and out-of-slice ripples. For variable loading of the RF coil, it allows maximizing pulse bandwidth while remaining within RF power limits, the most stringent limit being imposed by the refocusing pulse polarized at $KC_2 \not\propto B_{1,nom}^+$. Pulse length can be optimized independently, as longer SLR pulses lead to a narrower transition band but induce higher T_2-attenuation and stronger T_2-dependence of the pulse profile.

It is shown that the accuracy of DAM-SP can be further improved by decreasing pollution due to the out-of-slice signal. The most important insight underlined by Figure 2 is that OBM rapidly increases when $\not\propto B_1^+$ is higher than the RF field amplitude of the minimum. This implies that DAM(-SP) can be biased in regions for which coil inhomogeneities lead to large angles. To address this issue, we demonstrated that changing the ratio between excitation and refocusing angles shifts the minimum OBM towards lower or higher excitation angles. It is noteworthy that the minimum OBM for conventional SE with $C = 2$ is reached at 145°, far from 90°, which is however the commonly angle prescribed for most quantitative mapping

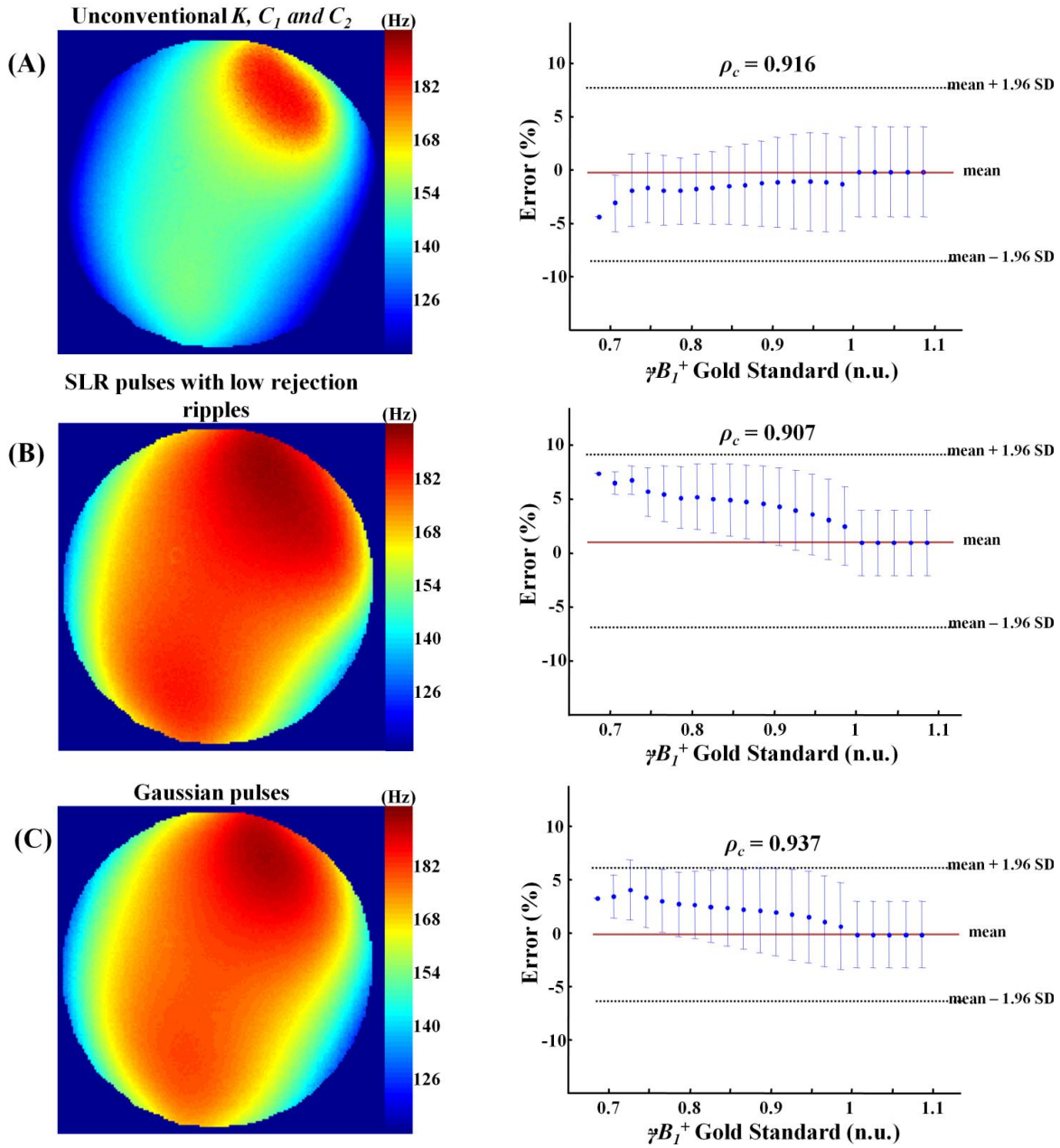

Figure 6: (Left) γB_1^+ maps obtained by DAM-SP with different strategies for reducing OBM-dependent inaccuracies (A) K = 3, C_1 = 3, C_2 = 1.5 (B) SLR pair with rejection ripple = 0.01% (C) Gaussian pair. (Right) Respective Bland and Altman plots.

based on multi-slice SE. The problem of designing a B_1^+-mapping protocol using this concept is to choose C_1 and C_2 at a given K for which; (i) the prescribed angle α_1 corresponds to a Γ-maxima, (ii) OBM is minimum for both angles α_1 and $\alpha_2(=K\alpha_1)$ (iii) the dynamics is not too small. Several coherent sets of C_1 and C_2 were determined numerically for different K, and in particular that tested experimentally, leading to improved accuracy (Fig. 6-A). However, iterative conjoint optimization of K, C_1 and C_2 deserves further study to identify the optimal sets.

Besides, reducing the out-of-slice ripple of SLR pulses (Fig. 6-B) and using Gaussian shapes (Fig. 6-C) is additional solutions for improving the accuracy of B_1^+-mapping with DAM-SP. The greater improvement obtained when using Gaussian pulses indicates that the continuous increase in out-of-slice rejection with off-resonance is preferable to minimizing a constant out-of-slice ripple.

A possible limitation of slice-selective B_1^+ mapping is that variations in spin density, T_1 and T_2 through the slice render efforts to compensate for slice profile ineffective. If a non steady-state condition holds for all T_1-populations of the imaged volume, only proton density and T_2 weightings remain in the expression of transverse magnetization amplitude. Therefore the integral of Eq.[2] over the off-resonance frequency, which mapped the slice direction, should be extended as follows

$$M_{xy}\left(\not\propto B_1^+, C\right) = \int M_0(\omega)E_2(\omega)\sin\alpha\left(\omega;\ \not\propto B_{1,exc}^+\right)\sin^2\left(\beta\left(\omega; C\not\propto B_{1,exc}^+\right)/2\right)\ d\omega. \quad [9]$$

This expression underlies a constant $\not\propto B_1^+$ over the voxel volume, which is reasonable for the current voxel volume. Because B_1^+-dependent and B_1^+-independent terms are separable, one can rewrite

$$M_{xy}\left(\not\propto B_1^+, C\right) = \sum_i v^i M_0^i E_2^i \int \sin\alpha\left(\omega;\ \not\propto B_{1,exc}^+\right)\sin^2\left(\beta\left(\omega; C\not\propto B_{1,exc}^+\right)/2\right)d\omega, \quad [10]$$

Where v^i is the relative volume of the *i*-th population, characterized by spin density M_0^i and T_2 weighting E_2^i. The expression $\sum_i v^i M_0^i E_2^i$ cancels after calculating ratio Q, which demonstrates that the resulting B_1^+-map does not depend on variations in spin density, T_1 and T_2 through the slice.

DAM has emerged as the reference method for B_1^+ mapping, partly because it uses widely available sequences. Now DAM-SP reconstruction and the protocol design based on verifying

the factor of merit Γ presented here can be applied to any sequence, such as FID data collections (33) or STEAM sequences (18).

Although we show here that DAM-SP improves the accuracy of DAM, it still suffers from long acquisition time, especially for high T_1 populations, justifying the replacement of spin warp by EPI in order to improve temporal resolution. In line with (1, 14), good agreement was observed between B_1^+ maps obtained with echo-planar and spin-warp encodings, except in the regions affected by strong susceptibility artifacts (data not shown). The number of segmentation steps should be determined in each particular experimental context with regard to the extent of these artifacts and to the decrease of SNR. Other trajectories should be used, starting from the center of the *k*-space (e.g. spiral) in order to limit SNR loss due to acceleration (15).

In conclusion, we highlighted solutions for correcting three significant sources of errors when B_1^+ is mapped using the DAM method and selective pulses. As they are independent, these solutions can now be combined for high-precision and fast B_1^+-mapping using spin-echo DAM. Such development paves the way for improving the precision of many applications for which rapid knowledge of B_1^+ distribution is crucial.

4.7 CITED REFERENCES IN ARTICLE 4

1. Thulborn KR, Boada FE, Shen GX, Christensen JD, Reese TG. Correction of B_1 inhomogeneities using echo-planar imaging of water. Magn Reson Med 1998;39:369-75.

2. Shah NJ, Ermer V, Oros-Preusquens AM. Measuring the absolute water content of the brain using quantitative MRI. Methods Mol Biol 2011;711:29-64.

3. Cheng HLM, Wright GA. Rapid high-resolution T_1 mapping by variable flip angles: Accurate and precise measurements in the presence of radiofrequency field inhomogeneity. Magn Reson Med 2006;55:566-74.

4. Deoni SCL. High-resolution T_1 mapping of the brain at 3T with driven equilibrium single pulse observation of T_1 with high-speed incorporation of RF field inhomogeneities (DESPOT1-HIFI). J Magn Reson Imaging 2007;26:1106-1111.

5. Sled JG, Pike GB. Correction for B_1 and B_0 variations in quantitative T_2 measurements using MRI. Magn Reson Med 2000;43:589-593.

6. Roberts DA, Insko EK, Bolinger L, Leigh JS. Biplanar radiofrequency coil design. J Magn Reson 1993;102:34-41.

7. Shen GX, Boada FE, Thulborn KR. Dual-frequency, dual-quadrature, birdcage RF coil design with identical B_1 pattern for sodium and proton imaging of the human brain at 1.5 T. Magn Reson Med 1997;38:717-725.

8. Simmons A, Tofts PS, Barker GJ, Arridge SR. Sources of intensity nonuniformity in spin echo images at 1.5 T. Magn Reson Med 1994;32:121-128.

9. Glover GH, Hayes CE, Pelc NJ, Edelstein WA, Mueller OM, Hart HR, Hardy CJ, O'Donnell M, Barber WD. Comparison of linear and circular polarization for magnetic resonance imaging. J Magn Reson 1985;64:255-270.

10. Bottomley, P. A. and Andrew, E. R. RF magnetic field penetration, phase shift and power dissipation in biological tissue: implications for NMR imaging. Phys Med Biol 1978;23:630-643.

11. Morrell GR. A phase-sensitive method of flip angle mapping. Magn Reson Med 2008;60:889-894.

12. Sacolick LI, Wiesinger F, Hancu I, Vogel MW. B_1 mapping by Bloch-Siegert shift. Magn Reson Med 2010;63:1315-1322.

13. Stollberger R, Wach P. Imaging of the active B_1 field in vivo. Magn Reson Med 1996;35:246-251.

14. Wang J, Qiu M, Yang QX, Smith MB, Constable RT. Measurement and correction of transmitter and receiver induced nonuniformities in vivo. Magn Reson Med 2005;53:408-417.

15. Cunningham CH, Pauly JM, Nayak KS. Saturated double-angle method for rapid B_1^+ mapping. Magn Reson Med 2006;55:1326-1333.

16. Yarnykh VL. Actual flip-angle imaging in the pulsed steady state: A method for rapid three-dimensional mapping of the transmitted radiofrequency field. Magn Reson Med 2007;57:192-200.

17. Nehrke K. On the steady-state properties of actual flip angle imaging (AFI). Magn Reson Med 2009;61:84-92.

18. Akoka S, Franconi F, Seguin F, Le Pape A. Radiofrequency map of an NMR coil by imaging. Magn ResonImaging 1993;11:437-441.

19. Pan JW, Twieg DB, Hetherington HP. Quantitative spectroscopic imaging of the human brain. Magn Reson Med 1998;40:363-369.

20. Wang J, Mao W, Qiu M, Smith MB, Constable RT. Factors influencing flip angle mapping in MRI: RF pulse shape, slice-select gradients, off-resonance excitation, and B0 inhomogeneities. Magn Reson Med 2006;56:463-468.

21. Schär M, Vonken EJ, Stuber M. Simultaneous B_0- and B_1^+-Map acquisition for fast localized shim, frequency, and RF power determination in the heart at 3 T. Magn Reson Med 2010;63:419-426.

22. Hornak JP, Szumowski J, Bryant RG. Magnetic field mapping. Magn Reson Med 1988;6:158-163.

23. Talagala SL, Gillen J. Experimental determination of three-dimensional RF magnetic field distribution of nmr coils. J Magn Reson 1991;94:493-500.

24. Zelaya FO, Roffmann WU, Crozier S, Teed S, Gross D, Doddrell DM. Direct visualisation of B_1 inhomogeneity by flip angle dependency. Magn Reson Imaging 1997;4:497-504.

25. Ernst RR, Bodenhausen G, Wokaun A. Principles of nuclear magnetic resonance in one and two dimensions. Oxford: Oxford University Press;1987. p 118-124.

26. Bendall MR, Gordon RE. Depth and refocusing pulses designed for multipulse NMR with surface coils. J Magn Reson 1983;53:365-385.

27. Bevington PR, Robinson KD. Data reduction and error analysis for the physical sciences, 2nd edition. New York: McGraw-Hill; 1992. p 38-52.

28. Matson GB. An integrated program for amplitude-modulated RF pulse generation and re-mapping with shaped gradients. Magn Reson Imaging 1994;12:1205-1225.

29. Pauly J, Le Roux P, Nishimura D, Macovski A. Parameter relations for the Shinnar-Le Roux selective excitation pulse design algorithm. IEEE Trans Med Imaging 1991;10:53-65.

30. Bland JM, Altman DG. Statistical methods for assessing agreement between two methods of clinical measurement. Lancet 1986;1:307-310.

31. Lin LI. A note on the concordance correlation coefficient. Biometrics 2000;56:324-325.

32. Meer P, Jolion JM, Rosenfeld A. A fast parallel algorithm for blind estimation of noise variance. IEEE 1990;2:216-223.

33. Wang D, Heberlein K, LaConte S, Hu X. Inherent insensitivity to RF inhomogeneity in FLASH imaging. Magn Reson Med 2004;52:927-931.

5. Article 5 : Modélisation des déformations et des transferts d'eau dans la viande pendant le chauffage

Après avoir mis au point un dispositif expérimental de chauffage et une méthode de cartographie de température, nous avons montré comment la déformation du muscle peut être cartographiée par imagerie rapide et traitement *ad hoc* des images obtenues. Une démarche générique a été appliquée pour construire des modèles en moyennant les courbes reliant température et déformation obtenues localement. Enfin, une méthode a été mise au point pour disposer du champ radiofréquence B_1 nécessaire à la cartographie non biaisée de la densité de protons.

En s'appuyant sur les différents développements méthodologiques et les résultats préliminaires exposés précédemment, nous sommes en mesure de répondre à l'objectif principal de cette thèse qui est la construction de modèles robustes liant température, déformation et quantité d'eau dans la viande pendant la cuisson.

Ce dernier manuscrit présente d'abord une synthèse des développements méthodologiques qui ont permis la construction des premiers modèles liant température, déformation et quantité d'eau. Cette démarche a été appliquée à deux types de muscle qui diffèrent essentiellement par la quantité de tissu conjonctif : le premier groupe en contenant peu, le second beaucoup plus. Les résultats montrent principalement une augmentation de la déformation avec la température, cette augmentation présentant une nette accélération vers 53 °C pour les échantillons présentant peu de tissu conjonctif et vers 59 °C pour les autres. Ce mécanisme peut être expliqué par des degrés de réticulation différents du collagène suivant l'âge de l'animal. Par ailleurs, la densité de proton diminue avec la température. Quoi que contre-intuitive, il existe une relation linéaire positive entre déformation et quantité d'eau. Tous ces résultats sont largement interprétés au regard notamment du comportement à la température des composants du muscle.

Ce dernier article fait largement écho aux perspectives dressées dans le premier article (Bouhrara 2011a). Il a donc été soumis au même journal (*Journal of Agricultural and Food Chemistry*) pour répondre à l'invitation du rédacteur en chef et des relecteurs qui demandaient à connaitre la fin de l'histoire …

In situ imaging highlights local structural changes during heating: The case of meat

Mustapha BOUHRARA, Sylvie CLERJON*, Jean-Louis DAMEZ, Alain KONDJOYAN and Jean-Marie BONNY.

UR370 Qualité des Produits Animaux, INRA, F-63122 Saint-Genès-Champanelle

Phone: +33-4- 73-62-45-93.

Fax: +33-4-73-62-40-89

E-mail: sylvie.clerjon@clermont.inra.fr

5.1 ABSTRACT

Understanding and monitoring deformation and water content changes in meat during cooking is of prime importance. We show the possibilities offered by nuclear magnetic resonance imaging (MRI) for the *in situ* dynamic measurement of deformation fields and water content mapping during beef heating from 20 to 75 °C. MRIs were acquired during heating, and image registration was used to calculate the deformation field. The temperature distribution in the sample was simulated numerically to link structural modifications and water transfer to temperature values. During heating, proton density decreases because of a magnetic susceptibility drop with temperature and water expulsion due to muscle contraction. A positive relationship was found between local cumulative deformation and water content. This new approach makes it possible to identify the deformation field and water transfer simultaneously and to trace thermal history to build heuristic models linking these parameters.

KEYWORDS: Cooking loss; deformation fields; heating; meat; quantitative MRI; structure

5.2 INTRODUCTION

Control of the sensory, nutritional, and technological qualities of end products is of prime importance for both consumers and industry. The case of meat is of particular interest because of the high sensitivity of its palatability traits to heating processes. The stakes are high for industrial companies that have to manage the cooking process of an increasing range of meat products.

Juice loss (also called water loss because it contains only 5−10% of dry matter) is a major palatability trait emphasized by consumers, which has to be monitored and controlled by the meat industry to ensure more efficient marketing of muscles and muscle groups (1) Furthermore, juiciness has been reported to be correlated with tenderness, the main palatability trait (2, 3) but with low correlation as reported by Dransfield *et al* (4). Indeed, water loss leads to lower perceived toughness, as the juices act as a sort of lubricant during mastication (5). In particular, higher juiciness plays a crucial role in acceptance of meat by young and elderly people, leading to longer mastication time of the bolus and in turn leading to better assimilation of nutrients (6).

Water losses are induced by structural changes that occur in meat during cooking (7). Classically, cooking loss is measured by weighing the samples before and after heat treatment and expressed as a percentage of the original weight. The reference method for obtaining this parameter was well-described by Honikel (8). An improvement of this reference method is to collect and weigh the water in real time during the heating process (9). Moreover, the latter authors measured the electrical conductivity of juice during cooking. With this technique, it is possible to correlate cooking loss and protein denaturation. Indirect, contactless methods of measuring water content after cooking have been developed. By using meat color measurement, Zheng (10) showed good correlation between moisture content and color features after cooking beef *triceps brachii* pieces cooked in a water-bath until their core temperature reached 72 °C. The result subjected to image analysis (11) showed that the cooking shrinkage of the surface area and volume was significantly correlated with cooking loss. In addition to the simple measurement of cooking loss, magnetic resonance imaging (MRI) makes it possible to monitor water transfer dynamically and locally during processes. It has been applied for wheat kernels drying (12), the rehydration of extruded pasta (13), the drying of a food gelatin analogue (14), and the rehydration of rice grains (15) during cooking. However, to our knowledge, it has never been applied during meat heating.

MRI is a nondestructive imaging method adapted to *in situ* and local analysis. Applied to meat during heating, it opens new paths for observing detailed changes in muscle structure and internal water transfer simultaneously. It requires prior methodological adjustments in order to apply a controlled thermal constraint to a sample in the high-field MRI magnet and acquire images from which deformation and water content can be derived with time. To achieve this, we introduced a novel MRI-compatible device, which heats the sample via a fluid, and a strategy based on the dynamic acquisition of images showing the contrast between muscle fibers and intramuscular connective tissue (16). Tracking these fiducial markers allowed reconstructing the required deformation maps (17). By using an additional validated simulation method, which provided temperature in the sample with time, the relationship between deformation and temperature was measured in different regions of the sample and was then averaged in a model. The underlying mechanisms of the three deformation phases, highlighted globally, were elucidated on the basis of the known behaviors of thermally sensitive muscle compounds (i.e., myosin, collagen, and sarcoplasmic proteins).

Finally, the water is expelled by the formation of intermyofibrilar channels between the fiber bundles followed by a global deformation of the meat (18, 5). The pertinence of the approach followed by these works leads us to continue these qualitative observations and map the water content in meat during heating and then investigate the quantitative relationship between temperature, deformation, and water content. Nevertheless, simultaneous mapping of deformation and water content requires major developments in MRI to acquire images rapidly enough to monitor the fast structural changes and water transfer occurring in muscles, especially at high critical temperatures. A second key aim is to map water content (i.e., proton spin density, PD) by taking the main source of bias into account, i.e., the variations of amplitude B_1 of the active emission radiofrequency (RF) field (pulsed during the MRI experiments) with temperature.

In this article, we present our results quantifying temperature, deformation, and water content during a meat heating process. Advantage was taken of *in situ* imaging to obtain local and simultaneous assessment for the first time. It is organized as followed: (i) we provide a brief description of the experimental hardware and meat samples; (ii) a description is then given of the MRI methods developed and used to solve the issues introduced before, by focusing on the approach used for accelerating the MRI acquisition process and mapping both

deformation and PD; (iii) finally, the interactions between parameters is presented and discussed in view to understanding the mechanisms linking temperature, deformation, and water content during meat heating.

5.3 MATERIAL & METHODS

5.3.1 Samples and hardware

Biceps femoris (BF) coming from Charolais cow samples were cut in the form of cylinders 5 cm in diameter by 6 cm in length, with the muscle fibers oriented axially. We chose this muscle because its richness in elastin is visible by T_2^*-weighted MRI. The dimensions of the sample were chosen to obtain an adequate picture of the perimysial structure of the muscle and still fit the dimensions of the MR imager. The meat cylinders were then placed in plastic bags in a vacuum to prevent direct contact with the circulating heating water. The results presented here were obtained from four samples: two samples from the same first animal containing high IMCT (intramuscular connective tissue) (high IMCT content 1 and high IMCT content 2), and the two others from a second animal containing low IMCT (low IMCT content 1 and low IMCT content 2). This rating according to IMCT content was based on visual observation. For each sample, our analyses were performed on five transverse slices, which intercepted the muscle fiber axis perpendicularly.

Each sample was heated over the temperature range 20−75 °C using water circulating (42 L/min) in an MRI-compatible device. It comprised a watertight sample holder cell made of polyetheretherketone placed inside a Teflon sleeve to ensure thermal insulation between the cell and the RF coil. The regulation system was programmed so that the temperature of the water rose constantly at a gradient of 0.63 °C/min. This low gradient (regarding those commonly applied in industrial processes) was chosen for being compatible with our MRI acquisition times.

Image acquisition was carried out using a Biospec horizontal 4.7 T MRI system (Bruker GmbH, Ettlingen, Germany), with a 26 cm diameter bore, equipped with a BGA-26 rapid gradient system and using a linear polarized birdcage coil for both emission and reception. The main fiber axis in the sample was placed approximately parallel to the direction of the static magnetic field of the magnet. The heating water run-off was roughly directed by the pump installed in parallel in this direction.

5.3.2 Temperature mapping

Temperature maps were obtained from numerical simulations with finite elements using the Comsol Multiphysics 3.4 software. The heat exchanges in the juice and the meat were considered as purely conductive. Water flow inside the sample was neglected because it was checked by simulations for having a very low influence in the heat exchanges. The calculation was performed stepwise on the basis of the areas occupied by the meat after shrinkage and by the expelled juice, respectively. These areas were determined at each step by manual segmentation of MR images, which clearly delineated the juice−meat interface throughout the heating process. This approach was described in more detail and compared in ref 16 with invasive measurements, which demonstrated a maximum error of between 0.5 and 1 °C.

5.3.3 Dynamic MRI for deformation and proton density mapping

The imaging protocol consisted in continuous acquisition during heating of the same block made up of four different image sets. These sets were designed to acquire the images needed for accurate and fast quantitative mapping of deformation and PD.

The first set of images, named deformation images (DI), was acquired for highlighting the contrast between muscle fibers and intramuscular connective tissue. To do this, T_2^*-weighted images sensitive to differences of the magnetic susceptibility produced by the fiber-connective tissue interfaces inside the muscle were required. The protocol described in ref. 17 for mapping only deformation was perfected in order to accelerate image acquisition, the objective being to keep a reasonable delay between two successive T_2^*-weighted data sets because part of the time was spent acquiring the images needed for PD mapping. To this end, three gradient-echoes (GE) were acquired instead of a single echo during each repetition time (TR). We used centric encoding to maximize the signal-to-noise ratio (SNR) and minimize artifacts due to static field inhomogeneities. This approach was combined with half *k*-space sampling (19), a dedicated algorithm (POCS, 20) used for reconstructing images free of artifacts due to the missing part of *k*-space. The other image parameters were TR = 2 s, effective TE = 13 ms, FOV = 54 × 54 mm2, matrix = 216 × 216, and slice thickness = 2 mm (volume of the resulting voxel 0.25 × 0.25 × 2 mm^3). Multiple-GE and partial-sampling strategies led to an acceleration by 3 and 1.6, respectively, with an acquisition time of (2″ × 216) / (3 × 1.6) = 1′30″.

The acquisition of second and third sets of images, named PD images (PDI_1 and PDI_2), was necessary for PD mapping. It consisted in two spin−echo (SE) acquisitions of the same slices

differing only by their echo times (i.e., TE_1 = 13 ms and TE_2 = 51 ms, respectively). Since a long TR was necessary for mitigating T_1 dependence liable to bias PD maps, segmented echo planar encoding was used for accelerating PDI acquisition. This was logical because SE-EPI is much less prone to susceptibility artifacts than GE-EPI and is well-adapted for quantitative mapping of PD at low spatial resolution (21) as such resolution is sufficient for steady variation of water content in the muscle. The other image parameters were TR = 6 s, FOV = 54 × 54 mm^2, matrix = 108 × 108, slice thickness = 2 mm (volume of the resulting voxel 0.5 × 0.5 × 2 mm^3), and flip angles = 64°/180°. The use of segmented EPI led to an acceleration by a factor of 4 with the acquisition time being (6″ × 108)/4 = 2′42″ per PDI.

The last set of images was acquired for measuring amplitude B_1 of the active emission RF field. In the high field (here, 4.7 T), the interactions between this emission RF field and the (muscle) sample caused inhomogeneity of B_1, which was no longer negligible. Indeed, this inhomogeneity causes undesired effects during both spin excitation and signal reception, biasing the determination of PD when using the procedure described in the previous paragraph. B_1 distribution results from complex interference between decaying magnetic waves traveling in the sample-coil set and near fields induced by reflections at the interfaces (i.e., muscle, plastic bag, water, device, air, and coil). Equally important, the electromagnetic properties of the muscle evolve during heating because permittivity (encompassing conductivity and dielectric constant) increases with both temperature and water content (22, 23). Sample shrinkage during heating modifies the coupling between the sample and the RF coil (17, 24, 25). Since B_1 distribution depends on these unknown and evolving factors, experimental mapping of B_1 was preferred to numerical simulations and was done along with the acquisition of PDI_1 and PDI_2, to obtain adequate correction of PD maps during heating. The protocol for measuring B_1 distribution was an extension of the reference double angle method (26), which achieved high-precision and fast B_1-mapping using two SE images (27). It used PDI_1 obtained with an excitation flip angle of 64° and a second one differing only by its excitation flip angle of 127°. Note that these two images are named B_1 images ($B1I_1$ and $B1I_2$, respectively) and that PDI_1 and $B1I_1$ denominate the same image.

DI, PDI_1/ $B1I_1$, PDI_2, and $B1I_2$ were obtained in the same 5 slices spaced at 4 mm, oriented in the transverse plane to intercept the muscle fiber axis perpendicularly. The total acquisition time for the 4 image sets was (1′30″ + (3 × 2′42″)) = 9′36″. It was repeated 10 times during the temperature increase of the heating water between 20 and 75 °C (0.63 °C/min).

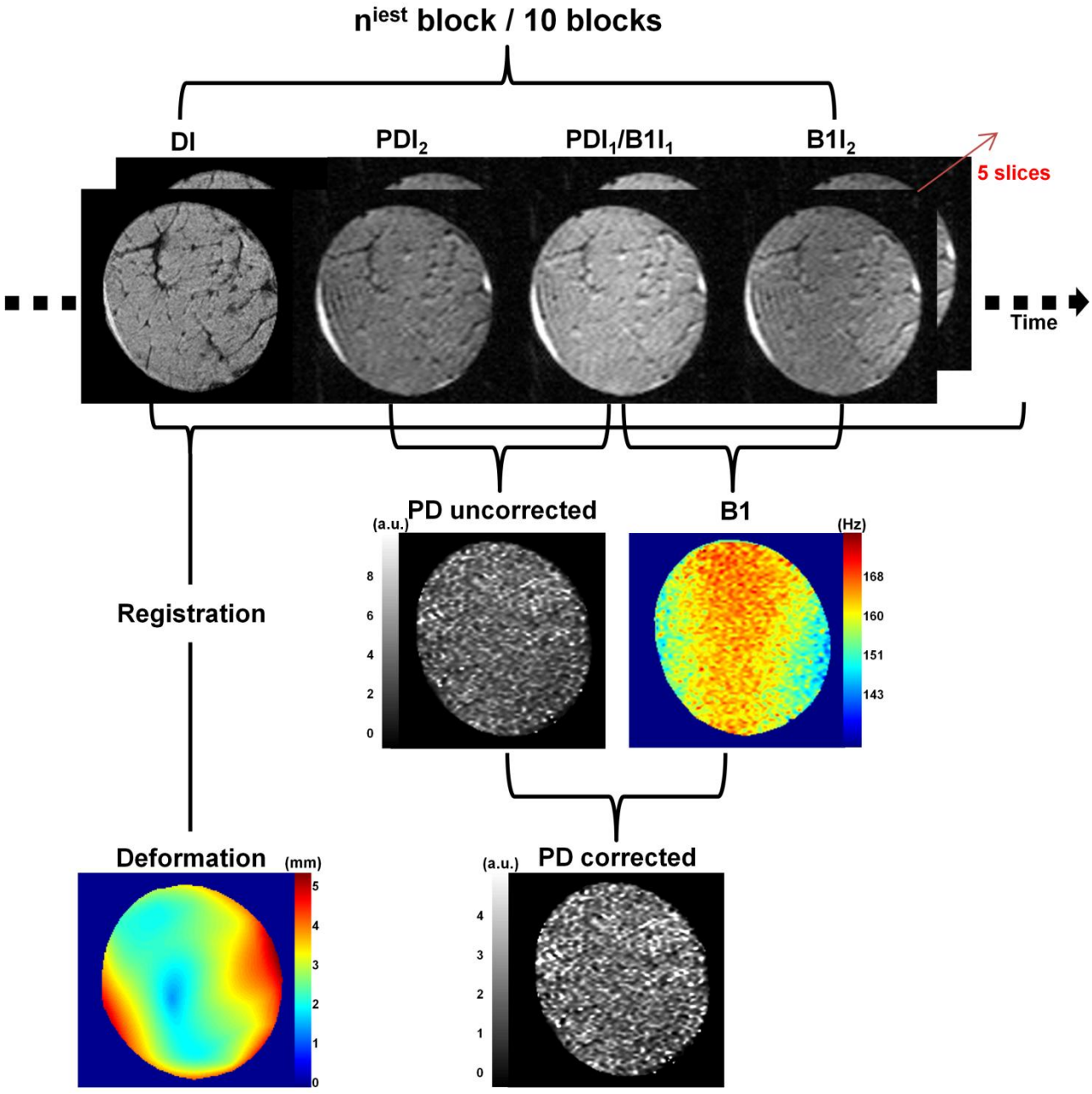

Figure 1: schematic representation of deformation and water content mapping during heating by dynamic MRI.

5.3.4 Reconstruction of deformation and proton density maps

The first step was to reconstruct the deformation fields of the sample from two successively acquired DIs. The deformation field at temperature t_i is the geometrical transformation required to pass from the image obtained at temperature t_{i-1} to that obtained at temperature t_i. We demonstrated previously that a 2D fourth order polynomial spatial transformation is adequate for modeling muscle deformation during heating (17). Then, the degrees-of-freedom of this transformation were estimated by minimizing the difference between the two DIs using an automated image registration package (28, 29). This registration is possible provided that the internal fiducial markers appear in the DIs throughout the heating process. Finally, the deformation field $\mathbf{w}(t_i)$ was inferred by computing the two components of 2D displacement in each voxel position of the image.

Using the two PDIs acquired at temperature t_i, the uncorrected PD was computed voxelwise according to

$$\widehat{PD}(t_i) = PDI_1 . \exp\left(TE_1/\hat{T}_2\right), \qquad [11]$$

where $\hat{T}_2$ was estimated assuming a mono-exponential behavior of T_2-decays, i.e.

$$\hat{T}_2(t_i) = (TE_2 - TE_1)/\ln(PDI_1/PDI_2). \qquad [12]$$

B_1-maps were reconstructed from the two SE images, $B1I_1$ and $B1I_2$ according to the method described in (27). The effects of B_1 inhomogeneities were integrated in a single spatially-varying correction factor assuming reciprocity, i.e. since the same coil was used for emission and reception, reception sensitivity was proportional to the amplitude of the emission field. Finally, corrected PD was obtained by dividing $\widehat{PD}(t_i)$ by this correction factor.

The whole approach for image acquisition and reconstructing quantitative maps is shown in Figure 1.

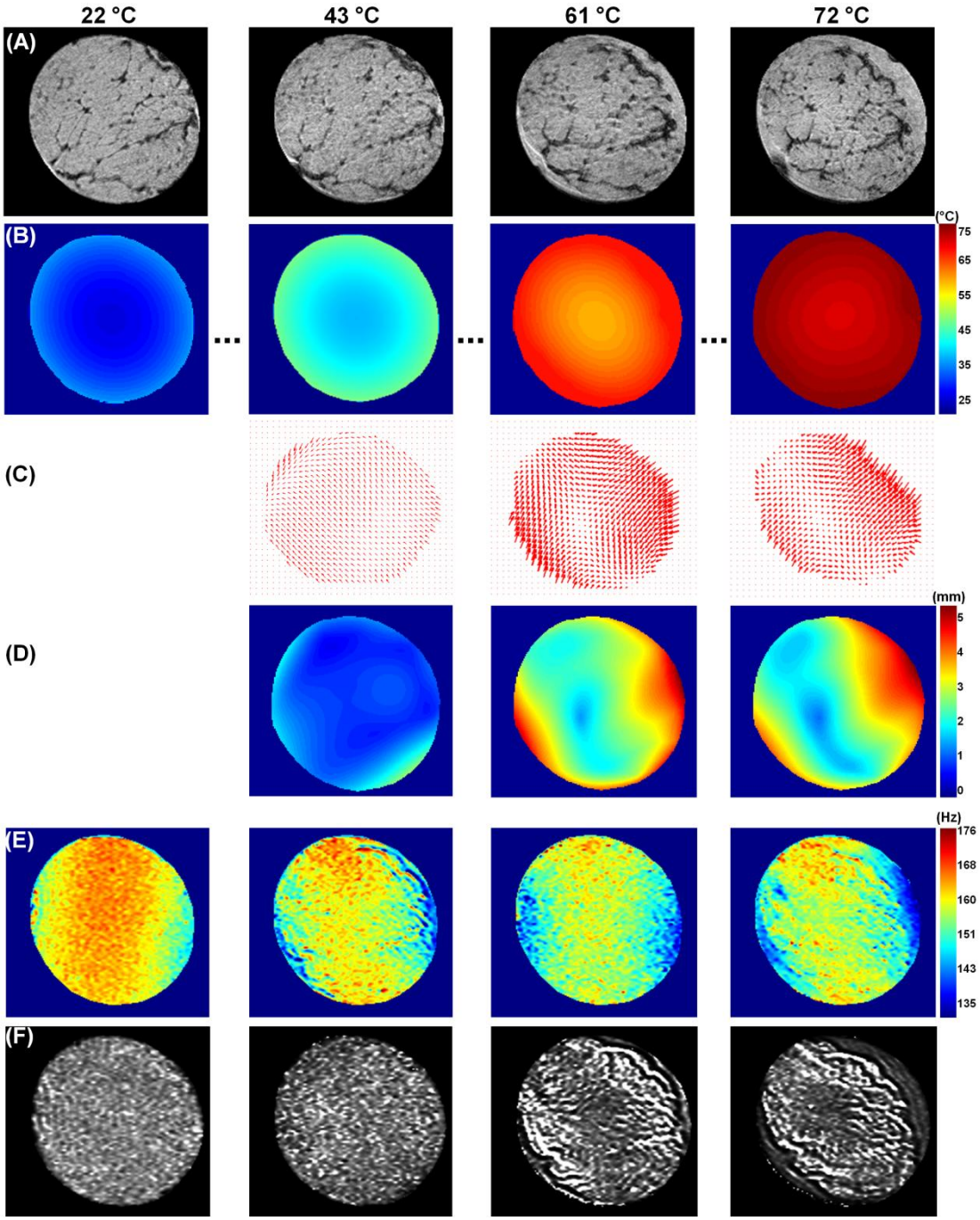

Figure 2: Sample with high IMCT content (slice 3/5). (A) T_2^*-weighted MR images (DIs). The windowing of gray levels was adjusted for each image to compensate for continuous SNR loss. (B) Corresponding temperature maps obtained by numerical simulation for four average temperatures in the sample. (C) Corresponding representations of deformation as a function of direction and magnitude calculated by nonlinear optimal registration from two consecutive DIs. (D) Corresponding representations of the magnitude of deformation calculated by nonlinear optimal registration from two consecutive DIs. (E) Corresponding B_1 maps. (F) Corresponding proton density maps.

5.3.5 From local information to average behaviors

The specific evolution of temperature was known locally and as a function of time. It was therefore possible to link the deformation and proton density time-courses measured in a given voxel from the maps, to their temperature rates. Our general approach was then to average such local relations for all the voxels of the images in order to highlight general laws.

Each voxel of the image obtained at 20 °C was tracked by successively applying the transformation $\mathbf{w}(t_i)$. Deformation, PD and temperature were collected from the quantitative maps along this trajectory as a function of time t_i. From an application point of view, it is interesting to know the impact of temperature on the final deformation; this corresponds to the accumulation of deformations between two successive images. Cumulative deformation and PD time-courses were placed in a common space where temperature became the abscissa. Lastly, these temperature-courses were averaged over all the voxels of the slice. All our samples were heated from 20 to 75 °C. Despite this, at the end of cooking, few voxels had effectively reached 75 °C. Thus to ensure robustness, the average models were only defined up to 70 °C.

In order to quantify the correlation between the PD and the cumulative deformation, several regions of interest (ROI) were defined manually for each of the 5 slices of each sample and for the last two images of our acquisition series, presenting the highest average temperatures (~70 °C). We chose to work on these images of the end of the process on which cumulative deformation and PD were most visible. For the ROI a homogenous deformation zone was chosen and the average cumulative deformation and the corresponding PD in this ROI were calculated.

All the numerical procedures were performed with Matlab (MathWorks Inc., Natick, USA).

5.4 RESULTS & DISCUSSION

Figures 2 and 3 show the different maps obtained at 4 average temperatures and in the central slice (3/5) of the sample for a high IMCT content sample and for a low IMCT content sample, respectively. They validate two important hypotheses: (i) DIs clearly show internal fiducial markers at each temperature despite the difficult experimental conditions leading to the

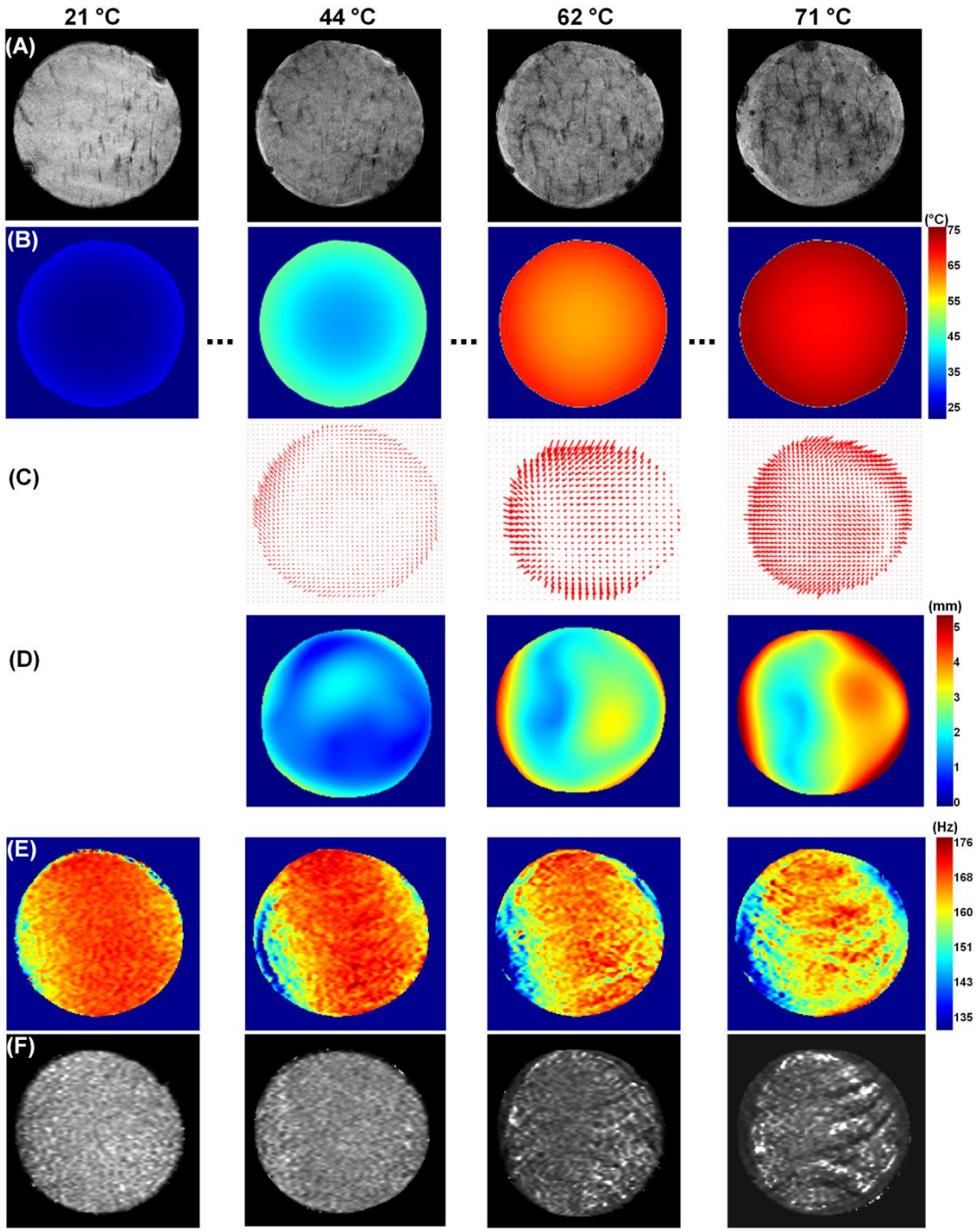

Figure 3: Sample with low IMCT content (slice 3/5). (A) T_2^*-weighted MR images (DIs). The windowing of gray levels was adjusted for each image to compensate for continuous SNR loss. (B) Corresponding temperature maps obtained by numerical simulation for four average temperatures in the sample. (C) Corresponding representations of deformation as a function of direction and magnitude calculated by nonlinear optimal registration from two consecutive DIs. (D) Corresponding representations of the magnitude of deformation calculated by nonlinear optimal registration from two consecutive DIs. (E) Corresponding B_1 maps. (F) Corresponding proton density maps.

continuous loss of SNR (Fig. 2A and 3A), (ii) experimental B_1 distribution is inhomogeneous in the sample and evolves with temperature (Fig. 2E and 3E), and (iii) temperature is inhomogenously distributed and leads to significant spatial variation of both deformation and PD. Under these conditions, the spatial registration step converged whatever the temperature and resulted in a robust estimation of the deformation fields in direction and magnitude (Fig. 2C,D and 3C,D). Figures 2E and 3E show the pertinence of this corrective mapping for PD as a function of temperature. Indeed, field B_1 depends on several factors, notably the dimensions of the sample and its dielectric properties (permittivity and conductivity), resonance frequency, type, and geometry of the coil used. This indicates moreover that the precise measurement *in situ* of the PD in MRI during heating must always be accompanied with a map of field B_1 to take into account its evolution due to deformation and to variations of the sample's dielectric properties. Lastly, the resulting temperature, deformations, and transfers of water cannot be considered as homogeneous, emphasizing the advantage of *in situ* MRI to model phenomena.

For better visual inspection, it should be noted that the gray scale windowing was adjusted to compensate for SNR loss for the PD maps shown in Figures 2F and 3F.

5.4.1 Average temperature-courses of deformation

High and low IMCT content samples presented similar deformation responses to thermal treatment. For both samples, deformation was greater at the surface than at the center of the sample because of the thermal gradient, the highest temperatures being on the external part of the sample. Cumulative deformation versus temperature (Fig. 4) exhibits the same behavior for both samples: before 40 °C, cumulative deformation is very slight (0.01 mm/°C) and corresponds to the accumulation of the image registration error module during field deformation computation (17). After this, a shallow slope can be observed before an inflection point (see red asterisks in Figure 4) marking a rise in the slope. The slopes are the same for the 4 samples: 0.030 ± 0.003 mm/°C before the inflection point and 0.21 ± 0.02 mm/°C after. Local information reveals a moderate strain between ∼38 °C and ∼55 °C. This phase corresponds to myosin denaturing, and the beginning of collagen denaturing, 30, 31 explaining the slight deformation observed. During this phase, juice is essentially transferred to interfascicular spaces within the muscle (16, 32, 33). The acceleration of deformation is due, on the one hand, to the heating of sarcoplasmic proteins (34) leading to their denaturing, as reported in Hoult (35), and therefore to a reduction of the mechanical resistance of the

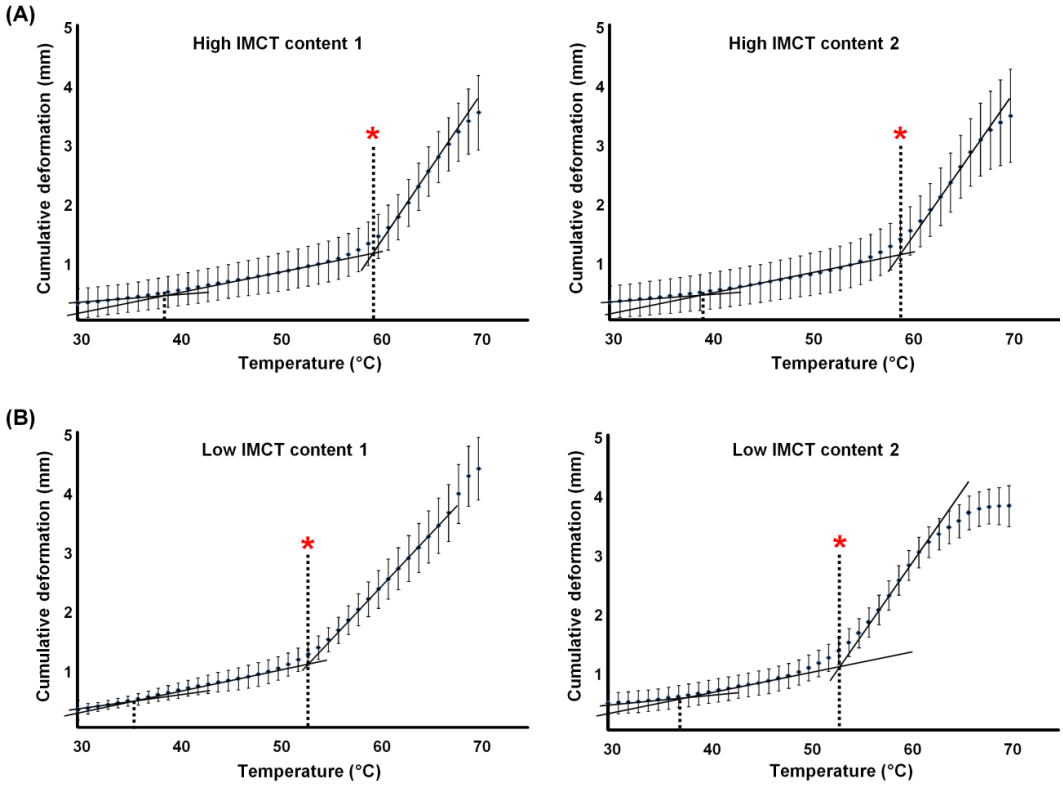

Figure 4: cumulative deformation (mm) versus temperature (°C) for high (A) and low (B) IMCT content samples. Error bars represent the standard deviation. The red star marks the inflexion point.

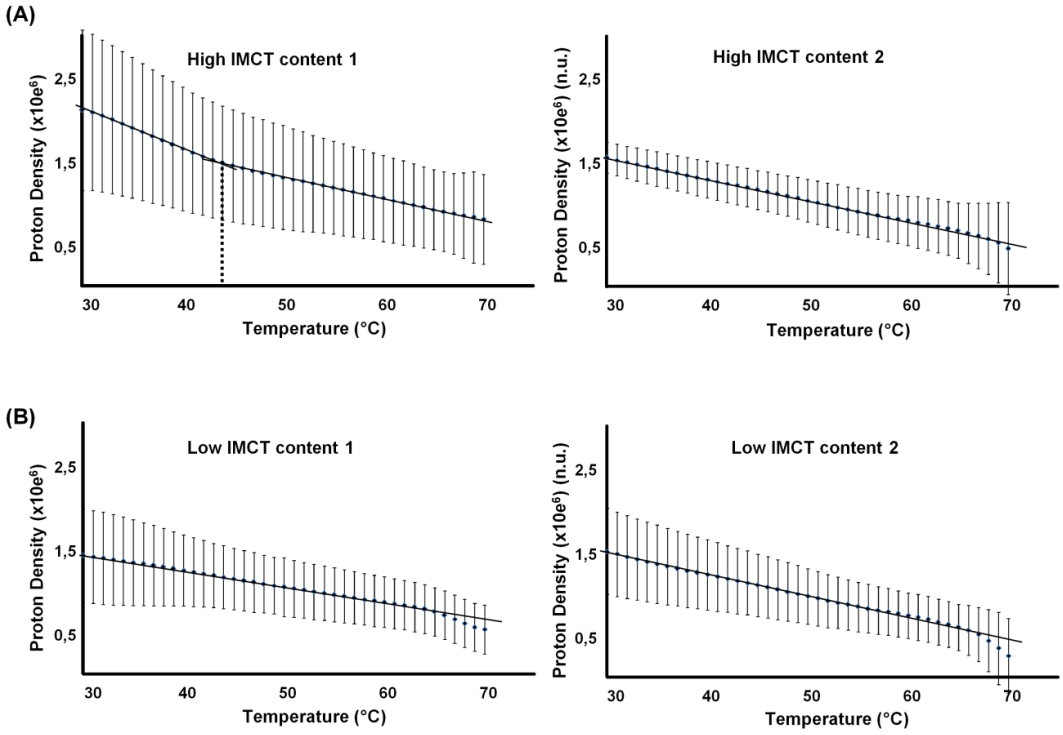

Figure 5: proton density versus average temperature (°C) for high (A) and low (B) IMCT content samples. Error bars represent the standard deviation.

myofibers to a mechanical stress; however, the deformation is due to the contraction of collagen leading to mechanical constraints that in turn lead to the contraction of the connective network (36). Water is then expelled to the exterior of the sample (32) visible as a surrounding hypersignal in Figures 2A and 3A, which explains the strong deformation observed. Plateaus of deformations that occur from ~68 °C can be explained by the end of one or several of these phenomena. Finally, the total (final) transverse deformation is the same whatever the IMCT content. This is consistent with the limitative characteristic of the muscle fiber's mechanical resistance to transverse contraction (37).

Although our experiments were performed on only two samples per category (low IMCT and high IMCT contents), a significant difference of deformation was revealed between these categories. Nevertheless, our results are consistent for the five studied slices. The samples with little connective tissue presented accelerated deformation from 53 °C, whereas it occurs at a higher temperature, i.e., 58.5 °C, in samples with higher connective tissue content (Fig. 4). This difference can first be explained by a difference in collagen type. Higher collagen content is often characteristic of older animals, whose degree of collagen reticulation and thus denaturation temperature increases (38). This could also explain that at the end of cooking, more marked and earlier (65 °C) saturation of deformation was observed for the second sample with low IMCT content. The second assumption is the difference of denaturation temperature between the endomysium and the perimysium (39). Denaturation of the endomysium at about 53 °C can cause measurable contraction only if there is little perimysium (Fig. 4B). Otherwise, the latter prevents contraction by the endomysium by providing a protective sheath to the muscle up to 58 °C, which is the temperature of its own denaturation and the resulting contraction (Fig. 4A). In addition, we observed (Fig. 2A and 3A) that the deformation did not follow the same radial symmetry as temperature, emphasizing that factors other than temperature likely determine deformation, in particular structural factors, such as the distribution of IMCT. The hypothesis is that a high amount of connective tissue is expressed by greater heterogeneity of its distribution inducing anisotropic contraction. Conversely, when this amount is less, its distribution is homogeneous and contraction is more radial.

5.4.2 Average temperature-courses of proton density

As shown in Figure 5, the PD in the muscle decreases considerably with temperature. This decrease is consistent with that reported by Micklander *et al.* (40) and Shaarani *et al.* (41). For three samples, we observed a linear loss of 2%/°C up to 65−67 °C, which then tended to be greater close to 70 °C, mainly in the case of low muscle IMTC. For the first sample containing a large amount of IMCT, two clear slopes could be observed, 4.7% / °C from 30 to 44 °C and 2.5% / °C from 44 to 70 °C. These losses lead to a reduction of total PD during cooking from 60 to 83% depending on the sample. This reduction is in part due to Curie's law that states that PD is inversely proportional to temperature (42, 43) i.e., corresponding to a signal change of 0.29% / °C to 0.34% / °C in our experimental range of 20−75 °C. The reduction of PD with temperature can also be explained by contraction that expels intramuscular water outside the muscle. This is undoubtedly the phenomenon that explains the sudden fall of PD when close to 70 °C for 3 of our samples. The quantification of final water loss (16, 44) permits explaining approximately 40% of the reduction of PD.

Instead of a true PD map, we in fact measured the amplitude of magnetization present in each voxel of the sample. This amplitude was proportional not only to the density of the spins observed but also to the temperature, as shown by the decrease of PD measured as a function of temperature. Because the observation frequency was tuned to the resonance of water protons, the measured amplitude was therefore theoretically proportional to their density, i.e., water content.

The amplitude of magnetization was derived from two SE acquisitions differing by their echo times, from which only a single amplitude can be inferred. In general, this amplitude is a biased estimate of total water content since the ideal unbiased approach requires summing the amplitudes of all the water pools. However, when a single water pool dominates, as in muscle, the bias due to monoexponential modeling is low, provided T_2 of the bulk component remains higher than the lowest echo time.

The results of Bertram *et al.* (18) obtained by the reference nonlocalized NMR method show that there is no major redistribution of water pools when comparing distributions of T_2 relaxation times between raw and cooked pork meat at the same room temperature, and *in situ* during heating for a temperature range similar to ours. A bulk water pool remains that shifts slightly toward lower T_2. This is consistent with the results reported later on chicken meat (41) and with our previous findings (17) indicating a decrease of T_2, measured by a two-point

imaging protocol. For all these studies, bulk T_2 was in the range from 20 to 80 ms, which remained higher than our lowest echo time (13 ms).

When heating a muscle to 76 °C and monitoring return to the initial temperature, Chen *et al.* (43) and Kovacsné *et al.* (45) showed that the evolution of PD with temperature is not reversible, contrary to what is observed in fat. The authors therefore conclude on an effect linked to the thermal modification of the constituents of the muscle since fat is not denatured at this temperature. Our results permit adding that transfers of water from intracellular spaces to interfascicular spaces, and then to the exterior of the muscle, also contribute to this irreversibility.

The sample high IMCT content 1 presented shrinkage of PD with temperature twice as fast below 44 °C. This phenomenon can likely be explained by the considerably higher PD of this sample before cooking, possibly resulting in a high loss of water (44).

For all the samples, it should be noted that the large standard deviations reflect the noise propagated on the maps of PD (Fig. 2F and 3F). In spite of all this, the very high number of voxels per slice (more than 10,000) endows statistic robustness to the averaged values presented.

5.4.3 Proton density versus cumulative deformation

An original aspect of our approach is that it provides a direct and average relation between deformation and quantity of water.

Figures 2 and 3 seem to show a correlation between the deformation modulus (line D) and the density of protons (line F) at high temperatures. A preliminary study has shown that there is no correlation between deformation and PD when comparing measurements voxel by voxel due to considerable spatial variations of PD (contrary to deformation). Part of this variability is moreover due to the presence of mobile water in the interfascicular spaces, which remains visible in spite of the partial volume effect (16). We therefore chose to average PD in ROIs in order to reduce this variability. This approach highlights the correlation coefficient of Spearman R^2 of the order 0.63 to 0.70 (Fig. 6), which shows that the most deformed zones are those where PD is highest, which may seem counterintuitive, though consistent with the poroelastic theory (46). This theory describes moisture transport using Darcy's law, which states that the fluid flow rate is linear with the pressure gradient. The pressure is partly due to

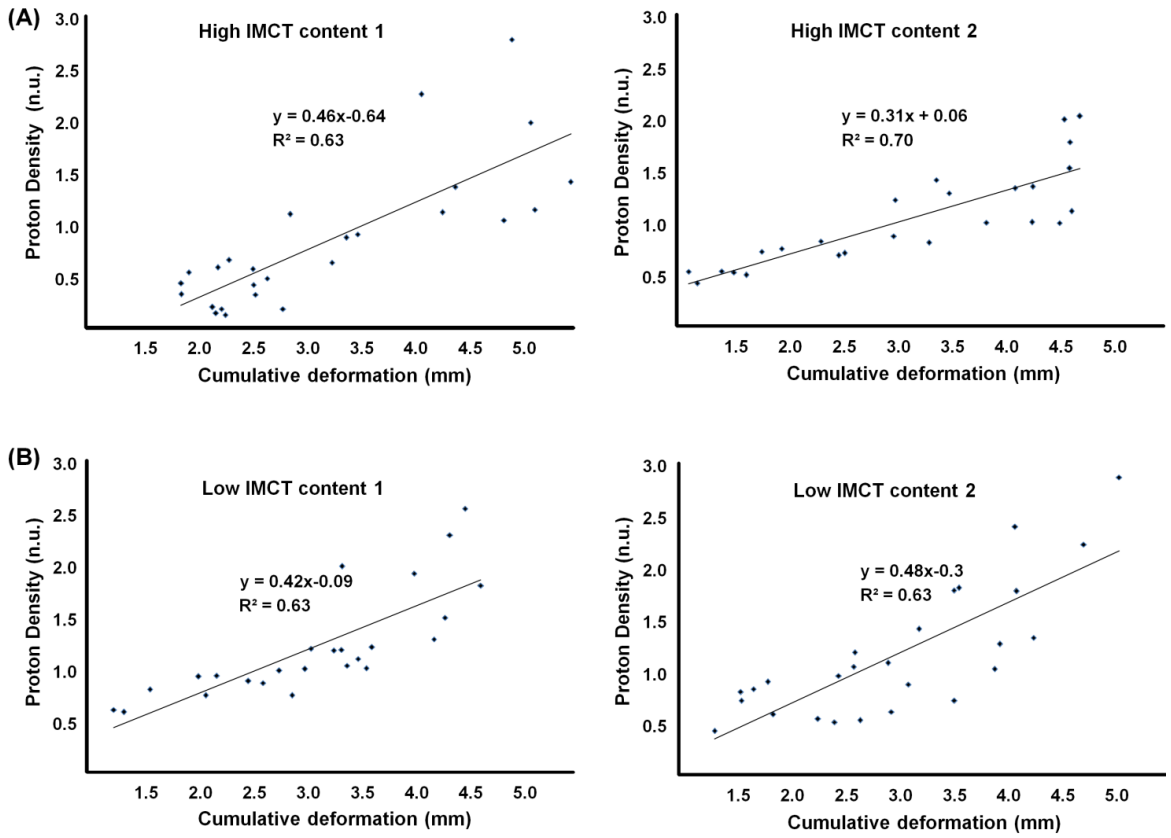

Figure 6: proton density versus cumulative deformation (mm) for high (A) and low (B) IMCT content samples. These results are obtained on several ROIs taking on 5 slices of each sample on the last two acquisitions at high temperature.

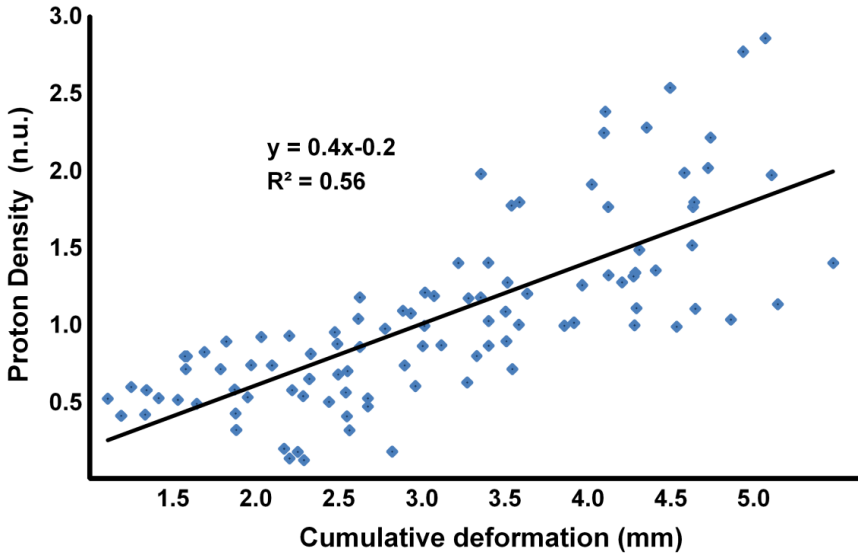

Figure 7: proton density versus cumulative deformation (mm) for merged data. These results are obtained on several ROIs taking on 5 slices of each sample on the last two acquisitions at high temperature.

the elasticity of the solid matrix of the porous material. It is fair to assume that the poroelastic theory also applies to meat during cooking, but in this case, it is supplemented with a constitutive equation for the pressure exerted by the contracting protein network during heating on the interstitial fluid (47). In this study, the interpretation was based on Darcy's law: water migrates from a high pressure area to a low pressure area. In the case of meat cooking, because of muscle contractions, the pressure in the muscle becomes higher than the external pressure, thus causing water to transfer from the sample toward the exterior. Moreover, at the superficial area of the sample, the temperature is higher than at the center, leading to the creation of interfascicular channels that may trap the migrating water. It is worthwhile noting that our method is dynamical and thus gives instantaneous images of PD during the heating process, a feature for which there is no equivalent, while water content in cooking meat is classically studied at the end of the heating process.

Figure 6 shows for 3 of the 4 samples, an increase of PD of 0.45 (n.u.) per mm of cumulative deformation. The fourth seems to be less sensitive to deformation (0.31 n.u. per mm). The calculation of confidence intervals of 95% of the slopes of our four lines of correlation are 0.31−0.61, 0.22−0.39, 0.28−0.56, and 0.32−0.64 for the samples high IMCT content 1, high IMCT content 2, low IMCT content 1, and low IMCT content 2, respectively. These intervals overlap, meaning that the four models are not significantly different justifying merging the data in a global model presented in Figure 7. This global model confirms the positive relationship between cumulative deformation and proton density.

The effects of temperature on cumulative deformation and water content described here were reproducibly observed for four different samples of the same muscle type (BF). On the basis of the spatial information provided by our imaging methodology to intramuscular structural variability (e.g., size of fascicles) and to differences of temperature regime inside the sample, a single experiment provides extensive information for modeling the relationship between temperature and deformation. However, both interanimal variation and muscle type are likely to have important effects, which deserve further studies on different muscle types, from different animals. Indeed, our method can be generalized provided that muscles sufficiently rich in elastin are used, as they guarantee good contrast of T_2^*-weighted MRI.

Whatever the case, the works presented here are pioneering in that they focus on the simultaneous presentation of deformation maps, water content, and temperature during

cooking. They should permit even better understanding of the occurrence of denaturation phenomena and contraction as a function of the type and state of proteins. Nonetheless, we admit that our cooking method is slower than that used in reality, as this slow gradient was chosen to highlight all the phenomena, despite the time resolution of the MRI.

In addition to the map of water content, information on its local diffusivity would help in interpreting water transfers observed at different scales during cooking. To take this understanding still further, it will be necessary to associate biochemical and spectroscopic analyses to know the nature and structural state of sarcoplasmic, myofibrillar, and collagen proteins present in each of the samples analyzed by MRI. More thorough modeling of the link between mechanical constraints and transfers of water should also permit improving the interpretation of the phenomena studied.

Better knowledge of the mechanisms responsible for the transfer of juice during cooking will permit better quantification of the fate, in the food, of hydrosoluble micronutrients since some of these micronutrients, such as iron and vitamins of group B, are very present and bioavailable in meats, especially beef. The fact of being able to study simultaneously water transfer and mechanical constraints will also lead to better understanding of the link between the tenderness and juiciness of meats. Since, in a general way, the reaction kinetics involved depend on the concentration of water, this work will permit better understanding of the sequence of all the biochemical reactions responsible for the quality of cooked meat.

In the framework of developing industrial cooking, it would be possible to study the effect of mechanical prestressing mainly that exerted during maturation, on deformation in cooking, another issue of interest to industry. The role of ingredients is also fundamental, for example, the effects of salting on cooking are of interest for the pork processing industry. Lastly, *in situ* monitoring of structural changes during cooking should be applied to all foods for which cooking is the decisive parameter for final quality.

5.5 CITED REFERENCES IN ARTICLE 5

1. Jeremiah, L.E.; Gibson, L.L.; Aalhus, J.L.; & Dugan, M.E.R. Assessment of palatability attributes of the major beef muscles. *Meat Science* **2003**, *65*, 949-958.
2. Harris, J.M.; Rhodes, D.N.; & Chrystall, B.B. Meat texture: I. Subjective assessment of the texture of cooked beef. *Journal of the Science of Food and Agriculture* **1972**, *3*, 101-114.
3. Becker, T. Consumer perceptions of fresh meat quality: A framework for analysis. *British Food Journal* **2000**, *102*, 158-176.
4. Dransfield, E; Francombe, M.A; & Whelehan, O.P. Relationships between sensory attribues in cooked meat. *Journal of Texture Study* **1984**, 15, 33-48.
5. Tornberg, E. Effects of heat on meat proteins-Implications on structure and quality of meat products. *Meat Science* **2005**, 70, 493-508.
6. Yven, C.; Culioli, J.; & Mioche, L. Meat bolus properties in relation with meat texture and chewing context. *Meat Science* **2005**, *70*, 365-371.
7. Bouton, P. E.; & Harris, P. V. The effects of cooking temperature and time on some mechanical properties of meat. *Journal of Food Science* **1972**, *37*, 140-144.
8. Honikel, K.O. Reference methods for the assessment of physical characteristics of meat. *Meat Science* **1998**, *49*, 447-457.
9. Brunton, N.P.; Lyng, J.G.; Zhang, L.; & Jacquier, J.C. The use of dielectric properties and other physical analyses for assessing protein denaturation in beef *biceps femoris* muscle during cooking from 5 to 85 °C. *Meat Science* **2006**, *72*, 236-244.
10. Zheng, C.; Sun, D.W.; & Zheng, L. Correlating colour to moisture content of large cooked beef joints by computer vision. *Journal of Food Engineering* **2006**, *77*, 858-863.
11. Du, C.J.; & Sun, D.W. Correlating shrinkage with yield, water content and texture of pork ham by computer vision. *Journal of Food Process Engineering* **2005**, *28*, 219-232.
12. Ghosh, P.K.; Jayas, D.S.; Gruwel, M.L.H.; & White, N.D.G. Magnetic Resonance Image analysis to explain moisture movement during wheat drying. *American Society of Agricultural and Biological Engineers* **2006**, *49*, 1181-1191.
13. Hills, B. Food processing: An MRI perspective. *Trends in Food Science & Technology* **1995**, *6*, 111-116.

14. Ruiz-Cabrera, M.A.; Foucat, L.; Bonny, J.M.; Renou, J.P.; & Daudin, J.D. Assessment of water diffusivity in gelatin gel from moisture profiles. I-Non-Destructive measurement of 1D moisture profiles during drying from 2D nuclear magnetic resonance images. *Journal of Food Engineering* **2005**, *68*, 209-219.
15. Mohoric, A.; Vergeldt, F.; Gerkema, E.; Van Dalen, G.; Van den Doel, L.R.; Van Vliet, L.J.; Van Ad, H.; & Van Duynhoven, J. The effect of rice kernel microstructure on cooking behavior: a combined µ-CT and MRI study. *Food Chemistry* **2009**, *115*, 1491-1499.
16. Bouhrara, M.; Clerjon, C.; Damez, J.L.; Chevarin, C.; Portanguen, S.; Kondjoyan, A.; & Bonny, J.M. Dynamic MRI and thermal simulation to interpret deformation and water transfer in meat during heating. *Journal of Agricultural and Food Chemistry* **2011**, *59*, 1229-1235.
17. Bouhrara, M.; Lehallier, B.; Clerjon, C.; Damez, J.L.; & Bonny, J.M. Mapping of muscle deformation during heating: *in situ* dynamic MRI and non-linear registration. *Magnetic Resonance Imaging* **2012**, 30, 422-430.
18. Bertram, H.C.; Engelsen, S.B.; Busk, Hans.; Karlson, A.H.; & Andersen, H.J. Water propreties during cooking of pork studied by low-fiel NMR relaxation: effects of curing and the RN¯gene. *Meat Science* **2004**, *66*, 437-446.
19. Finsterbusch, J.; & Frahm, J. Half-Fourier single-shot STEAM MRI. *Magnetic Resonance in Medicine* **2002**, *47*, 611-615.
20. Haacke, E.M.; Lindskog, E.D.; & Lin, W. A fast, iterative, Partial-Fourier technique capable of local phase recovery. *Journal of Magnetic Resonance* **1991**, *92*, 126-145.
21. Tawara, N.; Nitta, O.; Kuruma, H.; Niitsu, M.; & Itoh, A. T_2 mapping of muscle activity using ultrafast imaging. *Magnetic Resonance in Medical Sciences* **2011**, *10*, 85-91.
22. Simmons, A.; Tofts, P.S.; Barker, G.J.; & Arridge, S.R. Sources of intensity nonuniformity in spin echo images at 1.5 T. *Magnetic Resonance in Medicine* **1994**, *32*, 121-128.
23. Alecci, M.; Collins, C.M.; Smith, M.B.; & Jezzard, P. Radio Frequency Magnetic field mapping of a 3 Tesla birdcage coil: experimental and theoretical dependence on sample properties. *Magnetic Resonance in Medicine* **2001**, *46*, 370-385.
24. Zhuang, H.; Nelson, S.O.; Trabelsi, S.; & Savage, E.M. Dielectric Properties of Uncooked Chicken Breast Muscles from Ten to One Thousand Eight Hundred Megahertz. *Poultry Science* **2007**, *86*, 2433-2440.

25. Sipahioglu, O.; Barringer, S. A.; Taub, I.; & Prakash, A. Modeling the dielectric properties of ham as function of temperature and composition. *Journal of Food Science* **2003**, 68, 904−909.
26. Stollberger, R.; & Wach, P. Imaging of the active B_1 field in vivo. *Magnetic Resonance in Medicine* **1996**, 35, 246−251.
27. Bouhrara, M.; & Bonny, J.M. B_1 mapping with selective pulses. *Magnetic Resonance in Medicine* **2012** (Online, DOI: 10.1002/mrm.24146).
28. Woods, R.P.; Grafton, S.T.; Holmes, C.J.; Cherry, S.R.; & Mazziotta, J.C. Automated image registration: I. General methods and intrasubject, intramodality validation. *Journal of Computer Assisted Tomography* **1998**, *22*, 139-152.
29. Woods, R.P.; Grafton, S.T.; Holmes; C.J.; Cherry, S.R.; & Mazziotta, J.C. Automated image registration: II. Intersubject validation of linear and non-linear models. *Journal of Computer Assisted Tomography* **1998**, *22*, 153-165.
30. Martens, H.; Stabursvik, E.; & Martens, M. Texture and colour changes in meat during cooking related to thermal denaturation of muscle proteins. *Journal of Texture Studies* **1982**, *13*, 291-309.
31. Hindman, J.C. Proton resonance shift of water in the gas and liquid states. *The Journal of Chemical Physics* **1966**, *44*, 4582-4592.
32. Christensen, M.; Purslow, P.P.; & Larsen, L.M. The effect of cooking temperature on mechanical properties of whole meat, single muscle fibres and perimysial connective tissue. *Meat Science* **2000**, *55*, 301-307.
33. Straadt, I. K.; Rasmussen, M.; Andersen, H. J.; & Bertram, H. C. Aging-induced changes in microstructure and water distribution in fresh and cooked pork in relation to water-holding capacity and cooking loss - A combined confocal laser scanning microscopy (CLSM) and low-field nuclear magnetic resonance relaxation study. *Meat Science* **2007**, *75*, 687-695.
34. Nikmaram, P.; Yarmand, M.S.; Emamjomeh, Z.; & Darehabi, H.K. The effect of cooking methods on textural and microstructure properties of Veal muscle. *Global Veterinaria* **2011**, *6*, 201-207.
35. Hoult, D. I., & Lauterbur, P. C. The Sensitivity of the Zeugmatographic Experiment Involving Human Samples. Journal of Magnetic Resonance 1979, 34, 425-433.
36. Darrasse, L., & Ginefri, J. C. Perspectives with cryogenic RF probes in biomedical MRI. Biochimie 2003, 85, 915-937.

37. Lepetit, J. A theoretical approach of the relationships between collagen content; collagen cross-links and meat tenderness. Meat Science 2007, 76, 147-159.
38. Horgan, D.J.; Jones, P.N.; King, N.L.; Kurth, L.B.; & Kuypers, R. The relationship between animal age and the thermal stability and cross-link content of collagen from five goat muscles. *Meat Science* **1991**, *29*, 251-262.
39. Li, C.B.; Zhou, G.H.; & Xu, X.L. Dynamical Changes of Beef Intramuscular Connective Tissue and Muscle Fiber during Heating and their Effects on Beef Shear Force. *Food and Bioprocess Technology* **2010**, *3*, 521-527.
40. Micklander, E.; Peshlov, B.; Purslow, P.P.; & Engelsen, S.B. NMR-cooking: monitoring the changes in meat during cooking by low-field H-1-NMR. *Trends in Food Science & Technology* **2002**, *13*, 341-346.
41. Shaarani, S. M.; Nott, K. P.; & Hall, L.D. Combination of NMR and MRI quantitation of structure and structure changes for convection cooking of fresh chicken meat. *Meat Science* **2006**, *72*, 398-403.
42. Abragam, A. *The principles of the nuclear magnetism*, New York: Oxford University Press, 1983, pp 599.
43. Chen, J.; Bruce, L.; & Pauly, K.B. Investigation of proton density for measuring tissue temperature. *Journal of Magnetic Resonance Imaging* **2006**, *23*, 430-434.
44. Oillic, S.; Lemoine, E.; Gros, J.B.; & Kondjoyan, A. Kinetic analysis of cooking losses from beef and other animal muscles heated in a water bath – Effect of sample dimensions and prior freezing and ageing. *Meat Science* **2011**, *88*, 338-346.
45. Kovacsne O.B.; Bayod, E.; Sjoholm, I.; & Tornberg, E. The mechanisms controlling heat and mass transfer on frying of beefburgers. III. Mass transfer evolution during frying. *Journal of Food Engineering* **2006**, 76, 169−178.
46. Barriere, B.; & Leibler, L. Kinetics of solvent absorption and permeation through a highly swellable Elastomeric network. *Journal of Polymer Science B* **2003**, *41*, 166-182.
47. Van der Sman, R. G. M. Moisture transport during cooking of meat: An analysis based on Flory-Rehner theory. *Meat Science* **2007**, *76*, 730-738.

VII. Conclusion générale et perspectives

Ce travail de thèse porte sur l'évolution de la structure et des transferts d'eau dans la viande en fonction de la température. Il a demandé des développements méthodologiques conséquents qui ont permis, *in fine*, d'établir des modèles robustes pour la compréhension de l'impact du chauffage sur le muscle (article 5, partie 5.4). Ce travail montre d'abord que l'imagerie dynamique, quantitative et multiparamétrique (appelée aussi multispectrale) permet de décrypter des mécanismes intervenant lors de la cuisson sans établir des hypothèses réductrices lors de l'interprétation de ces phénomènes. Plus précisément, on ne fait ni hypothèse réductionniste en étudiant un échantillon intact à l'échelle macroscopique, ni hypothèse simplificatrice en prenant en compte les variations spatiales de la température dans l'échantillon.

Le développement des méthodes expérimentales a constitué une partie essentielle du travail. Il s'est agit successivement de concevoir, faire construire et tester la cellule de chauffage, de caractériser et de maitriser les conditions d'une expérience RMN pendant le chauffage, de simuler numériquement la distribution de la température dans l'échantillon et de la valider, de cartographier dynamiquement déformation et densité de protons, et enfin de construire les modèles à partir de l'information locale. Ce développement ne s'est pas fait au détriment de la question de sciences des aliments, posée initialement, qui est traitée et discutée dans le dernier manuscrit. Les modèles requis, couplant température, déformation et transfert de matière ont bien été obtenus. Leur reproductibilité a été testée en répétant les expériences et les comportements observés sont cohérents avec des mécanismes mis en évidence à d'autres échelles et par d'autres techniques. Plus qu'une validation, les résultats de cette thèse montrent les mécanismes dominants et ouvrent des voies vers l'étude de l'influence d'autres déterminants externes (régime de température, solutés) ou internes (structure musculaire).

Dans un temps limité, il s'est avéré délicat, voire frustrant, de ne pas pouvoir poursuivre tel ou tel aspect méthodologique excitant. C'est le cas par exemple de la technique d'imagerie GESFIDE qui présente des avantages substantiels (peu de sensibilité *off-resonance,* pondération en susceptibilité constante), mais n'a pu être généralisée et testée dans un contexte plus propice (T_2 long). Un effort particulier a été cependant réalisé sur la cartographie du champ radiofréquence B_1 pour prendre en compte les imprécisions liées aux

impulsions sélectives, et qui a mené la méthode à un haut degré de sophistication. Ceci a permis de démontrer expérimentalement que le champ radiofréquence B_1 est très variable en fonction de la température et qu'il est donc nécessaire de corriger ses effets dans les cartographies de densité de spins effectuées *in situ*, ce qui n'est pas toujours le cas dans la littérature.

Une grande partie des développements mis en place pour atteindre nos objectifs en science des aliments est sans doute transposable dans d'autres domaines, comme par exemple le domaine biomédical. C'est le cas d'abord de l'étude consacrée à l'accélération de l'imagerie haute résolution pondérée en susceptibilité (article 3, partie 3.4). L'analyse structurelle fondée sur l'analyse de l'évolution temporelle du signal RMN en module et/ou en phase est un domaine émergeant. Elle a été appliquée au cerveau (Duyn 2007, He 2009, Marques 2009, Schäfer 2009), à l'os trabéculaire (Wehrli 2007), au muscle (Bonny 2000, Bonny 2001) ou pour améliorer la détection d'agents de contraste. Ceci permet de faciliter le diagnostic et le suivi de l'évolution de certaines pathologies cérébrales (Thomas 2008, Haacke 2009, Holveck 2010). Néanmoins, les techniques classiques d'imagerie sont limitées par la diminution rapide du signal (Posse 1990, Callaghan 1990), par les distorsions géométriques dans les images RMN (Ericsson 1988, Bakker 1993, Reichenbach 1997) et par un temps d'acquisition trop long. Les techniques multi-écho proposées dans cette thèse (GESFID et GESFIDE) sont des solutions à ces inconvénients et sont donc très largement applicables.

La cartographie précise et rapide du champ radiofréquence B_1 (article 4, partie 4.2) est indispensable pour la quantification de la densité de spins en imagerie et en spectroscopie. Or, notre technique DAM-SP permet d'améliorer la rapidité et la précision des cartographies B_1 fondées sur l'utilisation d'impulsions sélectives. Ce sujet est d'actualité car les hétérogénéités spatiales de ce champ deviennent prégnantes à haut-champ et l'accès au haut-champ est de plus en plus large chez l'homme ou l'animal modèle. Outre les applications nombreuses en agro-alimentaire, mesurer la densité de proton délivre une information capitale dans le domaine biomédical, pour le diagnostic et le suivi de l'évolution de nombreuses pathologies, par exemple cérébrales (Badaut 2002, Wick 2004) ou pulmonaires (Fernández-Mondéjar 2003). Il en est de même pour le noyau de sodium, responsable du goût salé des aliments, et qui est par ailleurs impliqué dans certaines pathologies articulaires (Shapiro 2002, Borthakur 2006), et dans le métabolisme cardiaque (Jansen 2004) et cérébral (Thulborn 1999, Ouwerkerk 2003, Mellon 2009, Yushmanov 2009).

Ce travail original montre la faisabilité de l'IRM quantitative *in situ* sous contrainte thermique (article 1, partie 1.4.2). Si déformation et transfert d'eau ont principalement été ciblés, l'évolution de la dynamique rotationnelle de l'eau (temps de relaxations T_1 et T_2) a été abordée à une échelle très grossière (article 2, partie 2.4.1) et dans le but essentiel de maitriser les contraintes métrologiques. Il serait pertinent de quantifier ces mêmes paramètres à une échelle plus élevée, en fonction de la température et d'étendre ces mesures à la diffusion. Ceci permettrait de préciser les changements physicochimiques de la matrice (évolution des protéines, interactions de l'eau avec les macromolécules). Une perspective de ce travail est aussi d'aborder les propriétés viscoélastiques d'un l'aliment cuit qui sont habituellement évaluées par des tests mécaniques ou sensoriels, par essence peu localisés. Jusqu'à présent, le lien entre structure/composition et ces propriétés viscoélastiques était évalué de façon indirecte : la structure/composition par imagerie et les propriétés viscoélastiques par d'autres moyens. Ce processus est à la fois compliqué et générateur d'erreurs. Il pose des problèmes de constance de l'objet d'étude au cours des deux investigations. De plus, alors que les techniques d'imagerie fournissent une cartographie des constituants, l'évaluation des propriétés viscoélastiques demeure globale. Il est donc difficile, voire impossible, de relier une variation locale de structure ou de densité d'eau à un changement de propriétés viscoélastiques, et par conséquent très difficile de rattacher les propriétés viscoélastiques macroscopiques aux facteurs structuraux et compositionnels qui les gouvernent. Une solution consisterait à utiliser l'imagerie des propriétés viscoélastiques par élastographie IRM qui donne accès au module de cisaillement local sur l'aliment cuit (Manduca 2001, Manduca 2003) et donc reviendrait à imager les propriétés comme on image les structures. Ceci conduirait à traiter les mêmes objets au même moment avec la même technique pour établir des relations rigoureuses. Même si les travaux de cette thèse donnent une base solide, cette approche globale nécessite cependant des développements méthodologiques conséquents afin d'aboutir à des modèles explicites et reproductibles reliant l'ensemble de ces paramètres.

Un modèle thermique a été établi pour simuler numériquement la distribution spatio-temporelle de la température dans le muscle (article 1, 1.3.3). Ceci a permis de focaliser les mesures expérimentales par IRM sur les changements rapides de la structure de l'échantillon et de la quantité d'eau au cours du chauffage (article 5, partie 5.3.3). La simulation numérique de la température sous *Comsol Multiphysics* prend en compte la déformation du muscle en définissant ses contours par segmentation préalable des images RMN. Cette segmentation a été réalisée manuellement, ce qui a conduit à ne modéliser la température que dans la coupe

centrale et donc à faire l'hypothèse d'un comportement identique pour les coupes adjacentes. Bien que cette hypothèse ait été validée, il n'est pas certain qu'elle soit transposable à d'autres modes de cuisson. Pour cela, il serait souhaitable d'automatiser la segmentation pour l'étendre aux acquisitions tridimensionnelles ou de cartographier expérimentalement la température par IRM.

Par ailleurs, des expérimentations préliminaires ont montré que la déformation du muscle dans le sens longitudinal est négligeable car de l'ordre de 3%. Nos modèles ont donc été établis à partir d'acquisitions bidimensionnelles sur coupes transversales, en négligeant la déformation dans la direction longitudinale. Il n'est pas certain, là encore, que cette hypothèse de travail reste valable quel que soit l'échantillon étudié. L'hypothèse contraire imposerait d'améliorer nos méthodes de mesure par IRM, voire de changer d'approche. Par exemple, les gradients utilisés pour la saturation de l'eau chauffante engendrent une surchauffe lors d'acquisitions multicoupes jointives sur l'ensemble de l'échantillon.

Enfin, nos développements ont été adaptés pour un chauffage lent, ce qui permet de bien distinguer les mécanismes température-dépendant, et dans une gamme de températures comprises entre 20 et 80 °C. Bien que cette gamme soit représentative d'une cuisson industrielle, la montée en température est relativement lente. Pour être plus proche des modes de cuissons traditionnels, il conviendrait d'expérimenter d'autres régimes de température afin de mieux appréhender l'impact du chauffage sur la structure et la perte de matière dans la viande cuite. Par ailleurs, il serait aussi pertinent d'étudier l'effet de solutés ajoutés à la cuisson comme le sel. Ces deux aspects pourront être abordés sans difficulté en utilisant les mêmes outils.

Nous avons abordé le rôle de l'organisation structurale du muscle dans l'évolution de la déformation et de la perte en eau en fonction de la température (article 5, partie 5.4). Nous avons constaté, qu'un muscle riche en conjonctif se contracte moins rapidement avec la température. Ceci confirme que l'organisation structurale est un déterminant essentiel de la qualité organoleptique de la viande cuite. Pour préciser ce point, il est nécessaire d'étudier différents types de muscle avec des compositions et des organisations différentes. Cette information est cruciale notamment pour les industriels, car elle permettra, *in fine*, d'adapter le mode de cuisson pour chaque type de muscle dans le but de minimiser les pertes liées au chauffage.

En résumé, cette thèse avait pour but de décrire les mécanismes qui entrent en jeu lors du chauffage du muscle à partir d'une analyse quantitative, locale, dynamique et *in situ*. Elle y a répondu en apportant des connaissances nouvelles sur ce procédé universel. Elle a conduit de plus, à des développements méthodologiques applicables à d'autres champs et ouvre la voie à d'autres investigations dans le domaine de l'optimisation qualitative des produits carnés transformés.

Sur le plan personnel, au début de ma thèse je me suis particulièrement investi dans l'approfondissement de mes connaissances en IRM, au détriment des aspects « agro-alimentaires ». Au fil du temps, et bien sûr avec l'aide et la patience de mon équipe d'accueil, j'ai compris que travailler sur une matrice agroalimentaire était une chance. En effet, au-delà de la complexité du sujet et de la possibilité de développer des méthodologies nouvelles dans un milieu évolutif, cette thèse apporte des solutions originales et pluridisciplinaires en physique, mathématique et informatique pour répondre à des questions qui occupent depuis longtemps spécialistes en sciences des aliments et biophysiciens. Depuis mon premier cours d'IRM, j'ai toujours été attiré par cette technique probablement du fait de sa complexité et des possibilités qu'elle offre. C'est pourquoi j'ai choisi de préparer une thèse dans ce domaine. Dès le début, nous avons fait le choix de valoriser mes travaux sous forme de publications, ce qui m'a permis d'interagir concrètement avec une communauté scientifique élargie. Il en résulte une thèse sous forme d'articles certes, mais qui constitue un tout cohérent. Enfin, j'ai eu l'opportunité de côtoyer et de travailler avec des scientifiques de spécialités très différentes, qui ont su m'inculquer les compétences nécessaires et des valeurs humaines indispensables dans la carrière d'un jeune scientifique.

VIII. Bibliographie

Abbott JA **(1999)** Quality measurement of fruits and vegetables. *PostHarvest Bio Technol*,15:207-225.

Afssa **(2007)** Apport en protéines: consommation, qualité, besoins et recommandations (www.anses.fr/Documents/NUT-Ra-Proteines.pdf).

Altan A, Oztop MH, McCarthy KL, McCarthy MJ **(2011)** Monitoring changes in feta cheese during brining by magnetic resonance imaging and NMR relaxometry. *J Food Eng*, 107:200-207.

Amin MHG, Nott KP, Hall LD **(2007)** Quantitation by magnetic resonance imaging of heating of commercial baby foods in glass jars. *Inter J Food Sci Technol*, 42:1408-1415.

Antequera T, Caro A, Rodriguez PG, Perez T **(2007)** Monitoring the ripening process of Iberian ham by computer vision on magnetic resonance imaging. *Meat Sci*, 76:561-567.

Astruc T, Gatellier P, Labas R, Lhoutellier VS, Marinova P **(2010)** Microstructural changes in m.rectus abdominis bovine muscle after heating. *Meat Sci*, 85 :743-775.

Badaut J, Lasbennes F, Magistretti P, Regli L **(2002)** Aquaporins in brain: distribution, physiology and pathophysiology. *J Cerbral Blood Flow Metab*, 22:367-378.

Bailey AJ, Light ND **(1989)** Connective tissue in meat and meat products. *Elsevier Appl Sci*,1st ed, Essex.

Bakker CJG, Bhagwandien R, Moerland MA, Fuderer M **(1993)** Susceptibility artifacts in 2DFT spin-echo and gradient-echo imaging: the cylinder model revisited. *Magn Reson Imaging*, 11:539-548.

Barbera S, Tassone S **(2006)** Meat cooking shrinkage: measurement of a new meat quality parameter. *Meat Sci*, 73:467-474.

Barutcu I, McCarthy MJ, Seo YS, Sahin S **(2009)** Magnetic resonance temperature mapping of microwave-field chicken fingers. *J Food Sci*, 74:234-239.

Bejerholm C, Aaslyng MD **(2004)** Cooking of meat. *Encyclopedia of Meat Science*, Oxford, pp: 343-349.

Bendall JR, Restall DJ **(1983)** The cooking of single myofibres, small myofibre bundles and muscle strips from beef *M. psoas* and *M. sternomandibularis* muscles at varying heating rates and temperatures. *Meat Sci*, 8:93-117.

Bertin Y, Girardeau JP, Chaucheyras-Durand F, Lyan B, Pujos-Guillot E, Harel J, Martin C **(2011)** Enterohaemorrhagic Escherichia coli gains a competitive advantage by using ethanolamine as a nitrogen source in the bovine intestinal content. *Env Microb*, 13:365-377.

Bertola NC, Bevilacqua AE, Zaritzky NE **(1994)** Heat treatment effect on texture changes and thermal denaturation of proteins in beef muscle. *J Food Process*, 18:31-46.

Bertram HC, Donstrup S, Karlsson AH, Andersen HJ **(2002)** Continuous distribution analysis of T_2 relaxation in meat-an approach in the determination of water-holding capacity. *Meat Sci*, 60:279-285.

Bertram HC, Whittaker AK, Shorthose R, Andersen HJ, Karlsson AH **(2004)** Water characteristics in cooked beef as influenced by ageing and high-pressure treatment-an NMR micro imaging study. *Meat Sci*, 66:301-306.

Bertram HC, Engelsen SB, Busk H, Karlsson AH, Andersen HJ **(2004b)** water properties during cooking of pork studied by low-field NMR relaxation: effects of curing and the RN-gene. *Meat Sci*, 66:437-446.

Bock C, Sartoris FJ, Pörtner HO **(2002)** *In vivo* MR spectroscopy and MR imaging on non-anaesthetized marine fish: techniques and first results. *Magn Reson Imaging*, 20:165-172.

Bonny JM, Laurent W, Renou JP **(2000)** Detection of susceptibility effects using simultaneous T_2^* and magnetic field mapping. *Magn Reson Imaging*, 18:1125-1128.

Bonny JM, Laurent W, Labas R, Taylor R, Berge P, Renou JP **(2001)** Magnetic resonance imaging of connective tissue: a non-destructive method for characterizing muscle structure. *J Sci Food Agric*, 81:337-341.

Bonny JM, Rouille J, Valle GD, Devaux MF, Douliez JP, Renou JP **(2004)** Dynamic magnetic resonance microscopy of flour dough fermentation. *Magn Reson Imaging*, 22 :395-401.

Bonny JM **(2005)** Methods and applications of quantitative MRI. *Magn Reson Imaging*, 56:213-229.

Borisova MA, Oreshkin EF **(1992)** On the water condition in pork meat. *Meat Sci*, 31:257-265.

Borthakur A, Mellon E, Niyogi S, Witschey W, Kneeland JB, Reddy R **(2006)** Sodium and $T_{1\rho}$ MRI for molecular and diagnostic imaging of articular cartilage. *NMR Biomed*, 19:781-821.

Bottomley PA, Andrew ER **(1978)** RF magnetic field penetration, phase shift and power dissipation in biological tissue: implications for NMR imaging. *Phys Med Biol*, 23:630-643.

Bouhrara M, Clerjon C, Damez J.L, Chevarin C, Portanguen S, Kondjoyan A, Bonny J.M **(2011a)** Dynamic MRI and thermal simulation to interpret deformation and water transfer in meat during heating. *J Agric Food Chem*, 59:1229-1235.

Bouhrara M, Lehallier B, Clerjon C, Damez J.L, Bonny J.M **(2011b)** Mapping of muscle deformation during heating: *in situ* dynamic MRI and non-linear registration. *Magn Reson Imaging*, (In Press, DOI: 10.1016/j.mri.2011.10.002*).*

Bouton PE, Harris PV **(1972)** The effects of cooking temperature and time on some mechanical properties of meat. *J Food Sci*, 37:140-144.

Brown RJ, Capozzi F, Cavani C, Cremonini MA, Petracci M, Placucci G **(2000)** Relationships between ^{1}H NMR relaxation data and some technological parameters of meat: a chemometric approach. *J Magn Reson*, 147:89-94.

Burfoot D, James SJ **(1983)** Problems in mathematically modelling the cooking of a joint of meat. *In Thermal Processing and Quality of Foods, (edited by P. Zeuthen et al.),* pp. 467-472.

Burfoot D, James S J **(1988)** The effect of spacial variations of heat transfer coefficient on meat processing times, *J Food Eng*, 7: 41-61.

Cabrer PR, Van Duynhoven JPM Timmer H, Nicolay K **(2006)** Monitoring of moisture redistribution in multicomponent food systems by use of magnetic resonance imaging. *J Agric Food Chem*, 54:672-677.

California AN, Bertola NC, Bevilacqua AE, Zaritzky NE **(1997)** Effect of processing conditions on the hardness of cooked beef. *J Food Eng*, 34:41-54.

Callaghan PT **(1990)** Susceptibility-limited resolution in nuclear magnetic resonance microscopy. *J Magn Reson*, 87:304-318.

Carmody RN, Wrangham RW **(2009)** The energetic significance of cooking. *J Hum Evol*, 57:379-391.

Christensen M, Purslow PP, Larsen LM **(2000)** The effect of cooking temperature on mechanical properties of whole meat, single muscle fibres and perimysial connective tissue. *Meat Sci*, 55:301-307.

Clark CJ, Hockings, Joyce DC, Mazucco **(1997)** Application of magnetic resonance imaging to pre- and post-harvest studies of fruits and vegetables. *PostHarvest Bio Technol*, 11:1-21.

Culioli J, Berri C, Mourot J **(2003)** Muscle foods: consumption, composition and quality. *Sci Alim*, 23:13-34.

Currie RW, Wolfe FH **(1980)** Rigor related changes in mechanical properties (tensile and adhesive) and extracellular space in beff muscle. *Meat Sci*, 4:123:143.

Damez JL, Clerjon S **(2008)** Meat quality assessment using biophysical methods related to meat structure. *Meat Sci*, 80:132-149.

Davey CL, Gilbert K **(1974)** Temperature-dependent cooking toughness in beef. *J Sci Food Agric*, 25:931-938.

Delannoy J, Chen CN, Turner R, Levin RL, Le Bihan D **(1991)** Noninvasive temperature imaging using diffusion MRI. *Magn Reson Med*, 19:333-339.

Dickinson RJ, Hall AS, Hind AJ, Young IR **(1986)** Measurement of changes in tissue temperature using MR imaging. *J Comput Assist Tomogr*, 10:468-472.

Dubey JP, Kotula AW, Sharar AK, Andrews CD, Lindsay DS **(1990)** Effect of high temperature on infectivity of *Toxoplasma gondii* tissue cysts in pork. *J Parasitol*, 76:201-204.

Duyn JH, Van Gelderen P, Li TQ, De Zwart JA, Koretsky AP, Fukunaga M **(2007)** High-field MRI of brain cortical substructure based on signal phase. *Proc Natl Acad Sci USA* 104:11796-11801.

English AE, Joy MLG, Henkelman RM **(1991)** Pulsed NMR relaxometry of striated muscle fibers. *Magn Reson Med*, 21:264-281.

Ericsson A, Hemmingsson A, Jung B, Sperber GO **(1988)** Calculation of MRI artifacts caused by static field disturbances. *Phys Med Biol*, 33:1103-1112.

Evans SD, Nott KP, Kshirsagar AA, Hall LD **(1998)** The effect of freezing and thawing on the magnetic resonance imaging parameters of water in beef, lamb and pork meat. *Inter J Food Sci Technol*, 33:317-328.

Findlay CJ, Parkin KL, Stanley DW **(1986)** Differential scanning calorimetry can determine kinetics of thermal-denaturation of beef muscle proteins. *J Food Biochem*, 10:1-15.

Fjelkner-Modig S, Tornberg E **(1986)** water distribution in porcine M.longissimus dorsi in relation to sensory properties. *Meat Sci*, 17:213-231.

Fowler AJ, Bejan A **(1991)** The effect of shrinkage on the cooking of meat. *Inter J Heat Fluid Flow*, 12:375-383.

Galed G, Valle MEF, Martinez A, Heras A **(2004)** Application of MRI to monitor the process of ripening and decay in citrus treated with chitosan solutions. *Magn Reson Imaging*, 22:127-137.

Garcia-Segovia P, Andrés-Bello A, Martinez-Monzo J **(2007)** Effect of cooking method on mechanical propreties, color and structure of beef muscle (M. Pectoralis). *J Food Eng*, 80:813-821.

Gerber N, Scheeder MRL, Wenk C **(2009)** The influence of cooking and fat trimming on the actual nutrient intake from meat. *Meat Sci*, 81:148-154.

Gladden LF, Alexander P **(1996)** Application of nuclear magnetic resonance imaging in process engineering. *Meas Sci Technol*, 7:423:435.

Glover GH, Hayes CE, Pelc NJ, Edelstein WA, Mueller OM, Hart HR, Hardy CJ, O'Donnell M, Barber WD **(1985)** Comparison of linear and circular polarization for magnetic resonance imaging. *J Magn Reson*, 64:255-270.

Goni SM, Salvadori VO **(2010)** Prediction of cooking times and weight losses during meat roasting. *J Food Eng*, 100:1-11.

Götz J **(2006)** MRI in food process engineering. *Mod Magn Reson*, 1791-1796.

Gowen AA, Tiwari BK, Cullen PJ, McDonnell, O'Donnell CP **(2010)** Applications of thermal imaging in food quality and safety assessment. *Trends Food Sci Tech*, 21:190-200.

Guiheneuf TM, Couzens PJ, Wille HJ, Hall LD **(1997a)** Visualization of liquid tricyglycerol migration in chocolate by magnetic resonance imaging. *J Sci Food Agric*, 73:265-273.

Guiheneuf TM, Parker AD, Tessier JJ, Hall LD **(1997b)** Authentication of the effect of freezing/thawing of pork by quantitative magnetic resonance imaging. *Magn Reson Chem*, 35:112-118.

Haacke EM, Mittal S, Wu Z, Neelavalli J, Cheng YCN **(2009)** Susceptibility-weigthed imaging: technic aspects and clinical applications, part 1. *Am J Neuroradiol*, 30:19-30.

Hall LD, Talagala SL **(1985)** Mapping of pH and temperature distribution using chemical-shift-resolved tomography. *J Magn Reson*, 65:501-505.

Hall LD, Evans SD, Nott KP **(1998)** Mesurement of textural changes of food by MRI relaxometry. *Magn Reson Imaging*, 16:485-492.

Hamm R **(1960)** Biochemistry of meat hydratation. *Adv Food Res*, 10:355-463.

Hamm R **(1966)** Heating of muscle systems. *In the Physiology and Biochemistry of Muscle as a Food*, Madison, pp: 363-385.

Hamm R **(1977)** Changes of muscle proteins during the heating of meat. *In physical, Chemical and Biological Changes in Food Caused by Thermal Processing*, (Hoyen T, Kvale O, eds London), pp: 101-134.

Hazlewood CF, Chang DC, Nichols BL, Woessner DE **(1974)** Nuclear magnetic resonance transverse relaxation times of water protons in skeletal muscle. *Biophys J*, 14:583-606.

He X, Yablonskiy DA **(2009)** Biophysical mechanisms of phase contrast in gradient echo MRI. *Proc Natl Acad Sci*, 106:13558-13563.

Hearn LE, Penfield MP, Goertz GE **(1978)** Heating effects of bovine semitendinous: Shear force muscle fiber measurements and cooking losses. *J Food Sci*, 43:10-12.

Hills B **(1995)** Food processing: An MRI perspective. *Trends Food Sci Tech*, 6:111-117.

Holveck A, Grand S, Boini S, Kirchin M, Lebas JF, Dietemann JL, Bracard S, Kremer S **(2010)** Dynamic susceptibility contrast-enhanced MRI evaluation of cerebral intraventricular tumors: preliminary results. *J Neuroradiology*, 37:269-275.

Hostetler RL, Landman WA **(1968)** Photomicrographic studies of dynamic changes in muscle fiber fragments. 1. Effects of various heat treatments on length, width and birefringence. *J Food Sci*, 33:468-470.

Jansen MA, Van Emous JG, Nederhoff MGJ, Van Echted JA **(2004)** Assessment of myocardial viability by intracellular ^{23}Na magnetic resonance imaging. *J Am Heart Assoc*, 110:3457-3464.

Kantt CA,Webb AG, Litchfield JB **(1997)** Temperature measurement of foods using chemical shift magnetic resonance imaging as compared with T_1-weighted temperature mapping. *J Food Sci*, 62:1011-1016.

Kasai M, Lewis AR, Ayabe S, Hatae K, Fyfe C **(2007)** Quantitative NMR imaging study of the cooking of japonica and indica rice. *Food Res Inter*, 40:1020:1029.

Kerr WL, Clark CJ, McCarthy MJ, DeRopp JS **(1997)** Freezing effects in fruit tissue of kiwifruit observed by magnetic resonance imaging. *Scientia Horticulturae*, 69:169-179.

Koizumi M, Naito S, Haishi T, Utsuzawa S, Ishida N, Kano H **(2006)** Thawing of frozen vegetables observed by a small dedicated MRI for food research. *Magn Reson Imaging*, 24:1111-1119.

Kojima TI, Horigane AK, Yoshida M, Nagata T, Nagasawa A **(2001)** Change in the status of water in japanese noodles during and after boiling observed by NMR micro imaging. *Food Eng Phys Prop*, 9:1361-1365.

Kondjoyan A **(2008)** La cuisson des viandes et produits carnés et le couplage avec les reactions à l'origine de la qualité. *12^{e} JSMTV*, 41-48.

Laakkonen E **(1973)** Factores affecting tenderness during heating of meat. *Advances in Food Res*, 20:257-323.

Lassen A, Kall M, Hansen K, Oversen L **(2002)** A comparison of the retention of vitamins B1, B2 and B6, and cooking yield in pork loin with conventional and enhanced meal-service systems. *Eur Food Res Tech*, 215:194-199.

Laurent W, Bonny JM, Renou JP **(2000)** Muscle characterisation by NMR imaging and spectroscopic techniques. *Food Chem*, 69:419-426.

Layton DW, Bogen KT, Knize MG, Hatch FT, Johson VM, Felton JS **(1995)** Cancer risk of heterocyclic amines in cooked foods: an anlysis and implications for research. *Carcinogenesis*, 16:39-52.

Lepetit J **(2008)** Collagen contribution to meat toughness: theoretical aspects. *Meat Sci*, 80:960-967.

Hamilton WA, Sale AJH **(1967)** Effects of high electric fields on microorganisms: II.killing of bacteria and yeasts. *BioChim Biophys Acta* 148:789-800.

Mahdjoub R, Molegnana J, Seurin MJ, Briguer A **(2003)** High resolution magnetic resonance imaging evaluation of cheese. *Food Eng Phys Prop*, 68:1982-1984.

Manduca A, Oliphant TE, Dresner MA, Mahowald JL, Kruse SA, Amromin E, Felmlee JP, Greenleaf JF, Ehman RL **(2001)** Magnetic resonance elastography: non-invasive mapping of tissue elasticity. *Med Image Anal*, 5:237-254.

Manduca A, Lake DS, Kruse SA, Ehman RL **(2003)** Spatio-temporal directional filtering for improved inversion of MR elastography images. *Med Image Anal*, 7:465-473.

Marques JP, Maddage R, Mlynarik V, Gruetter R **(2009)** On the origin of the MR image phase contrast: an in vivo MR microscopy study of the rat brain at 14.1 T. *NeuroImage*, 46:345-352.

Martens H, Stabursvik E, Martens M **(1982)** Texture and colour changes in meat during cooking related to thermal denaturation of muscle proteins. *J Texture Studies*, 13:291-309.

McCarthy MJ, McCarthy KL **(1996)** Applications of magnetic resonance imaging to food research. *Magn Reson Imaging*, 14:799-802.

Mellon EA, Pilkinton DT, Clark CM, Elliott MA, Witschey WR, Borthakur A, Reddy R **(2009)** Sodium MR imaging detection of mild alzheimer disease: preliminary study. *Am J Neuroradiology*, 30:978-984.

Micklander E, Peshlov B, Purslow PP, Engelsen SB **(2002)** NMR-cooking monitoring the changes in meat during cooking by low field H^1 NMR. *Trends Food Sci Tech*, 13:341-346.

Mittal S, Wu Z, Neelavalli J, Haacke EM **(2009)** Susceptibility-weigthed imaging: technic aspects and clinical applications, part 2. *Am J Neuroradiol*, 30:232-252.

Mohr V, Bendall JR **(1969)** Constitution, physical and chemical properties of intramuscular connective tissue. *Nature*, 223:404:405.

Mondéjar EF, Pérez JC, Fernandez RR, Ruiz MC, Manzano F, Villares JMP, De la Chica R **(2003)** Quantification of lung water by transpulmonary thermodilution in neurmal and edematous lung. *J Crit Care*, 18:253-258.

Murphy RY, Marks BP **(2000)** Effect of meat temperature on proteins, texture and cook loss ground chicken beast patties. *Poultry Sci*, 79:99-104.

Musse M, Quellec S, Cambert M, Devaux MF, Lahaye M, Mariette F **(2009)** Monitoring the postharvest ripening of tomato fruit using quantitative MRI and NMR relaxometry. *PostHarvest Bio Technol*, 53:22-35.

Norat T *et al*. **(2005)** Meat, fish, and colorectal cancer risk: the european prospective investigation into cancer and nutrition. *J Natio cancer Institute*, 97(12):906-916.

Nott KP, Evans SD Hall LD **(1999)** Quantitative magnetic resonance imaging of fresh and frozen-thawed trout. *Magn Reson Imaging*, 17:445-455.

Nott KP, Hall LD **(1999b)** Advances in temperature validation of foods. *Trends Food Sci Technol*, 10:366-374.

Nott KP, Hall LD, Bows JR, Hale M, Patrick ML **(2000)** MRI phase mapping of temperature distributions induced in food by microwave heating. *Magn Reson Imaging*, 18:69-79.

Ogawa S, Tank DW, Menon R, Ellermann JM, Kim SG, Merkle H, Ugurbil K **(1992)** Instrinsic signal changes accompanying sensory stimulation: Functional brain mapping with magnetic resonance imaging. *Proc Natl Acad Sci*, 89:5951-5955.

Oillic S, Lemoine E, Gros JB, Kondjoyan A **(2011)** Kinetic analysis of cooking losses from beef and other animal muscles in a water bath- Effect of sample dimensions and prior freezing and ageing. *Meat Sci*, 88:338-346.

Ouwerkerk R, Blelch KB, Cillen JS, Pomper MG, Bottomley PA **(2003)** Tissue sodium concentration in human brain tumors as measured with ^{23}Na Mr imaging. *Radiology*, 227:529-537.

Palka K, Daun H **(1999)** Changes in texture, cooking losses and myofibrillar structure of bovine M.semitendinous during heating. *Meat Sci*, 51:237-243.

Pan Z, Singh RP, Rumsey TR **(2000)** Predective modeling of contact-heating process for cooking a hamburger patty. *J Food Eng*, 46:9-19.

Posse S, Aue WP **(1990)** Susceptibility artifacts in spin-echo and gradient-echo imaging. *J Magn Reson*, 88:473-492.

Potter JD **(1999)** Colorectal cancer: molecules and populations. *J Natio cancer Institute*, 91(11):916-932.

Rahman MS **(1995)** Food properties handbook. CRC Press, Boca Raton (Florida, USA), chapter 5, 301-302.

Rakesh V, Seo Y, Datta AK, McCarthy KL, McCarthy MJ **(2010)** Heat transfer during microwave combination heating: computational modeling and MRI experiments. *AIChE J*, 56:2468-2478.

Rao MA, Lund DB **(1986)** Kinectics of thermal softening of food-A review. *J Food Process*, 10:311-329.

Reichenbach JR, Venkatesan R, Yablonskiy DA, Thompson MR, Lai S, Haacke EM **(1997)** Theory and application of static field inhomogeneity effects in gradient echo imaging. *J Magn Reson Imaging*, 7:266-279.

Renou JP, Foucat L, Bonny JM **(2003)** Magnetic resonance imaging studies of water interactions in meat. *Food Chem*, 82:35-39.

Rinaldi M, Chiavaro E, Massini R **(2012)** Real-time estimation of slowest heating point temperature and residual cooking time by coupling multipoint temperature measurement and mathematical modelling: application to meat cooking automation. *Food Control*, 22:412-418.

Rosenberg MJ, McCarthy MJ, Kauten R **(1991)** Magnetic resonance imaging of cheese structure. *Food Struc*, 10:185-192.

Schäfer A, Wharton S, Gowland P, Bowtell R **(2009)** Using magnetic field simulation to study susceptibility-related phase contrast in gradient echo MRI. *NeuroImage*, 48:126-137.

Shaarani SM, Nott KP, Hall LD **(2006)** Combination of NMR and MRI quantification of structure and structure changes for convection cooking of fresh chiken meat. *Meat Sci*, 72:398-403.

Shackelford SD, Wheeler TL, Meade MK, Reagan JO, Byrnes BL, Koohmaraie M **(2001)** Consumer impressions of tender select beef. *J Anim Sci*, 79:2605-2614.

Shapiro EM, Borthakur A, Gougoutas A, Reddy R **(2002)** ^{23}Na MRI accurately measures fixed charge density in articular cartilage. *Magn Reson Med*, 47:284-291.

Shilton N, Mallikarjunan P, Sheridan P **(2002)** Modeling of heat transfer and evaporative mass losses during the cooking of beef patties using far-infrared radiation. *J Food Eng*, 55:217-222.

Shimokomaki M, Eisden DF, Bailey AJ **(1972)** Meat tenderness: age related changes in bovine intramuscular collagen. *J Food Sci*, 37:892-896.

Silva TJP, Orcutt MW, Forrest JC, Bracker CE, Judge MD **(1993)** Effect of heating rate on shorting, ultrastructure and fracture behaviour of prerigor beef muscle. *Meat Sci*, 33:1-24.

Stabursvik E, Martens H **(1980)** Thermal-denaturation of proteins in post-rigor muscle-tissue as studied by differential scanning calorimetry. *J Sci Food Agric*, 31:1034-1042.

Stollberger R, Wach P **(1996)** Imaging of the active B_1 field in vivo. *Magn Reson Med*, 35:246-251.

Thomas B, Somasundaram S, Thamburaj K, Kesavadas C, Gupta AK, Bodhey NK, Kapilamoorthy TR **(2008)** Clinical applications of susceptibility weighted MR imaging of the brain-a pictorial review. *Neuroradiology*, 50:105-116.

Thulborn KR, Gindin TS, Davis D, Erb P **(1999)** Comprehensive MR imaging protocol for stroke management: tissue sodium concentration as a measure of tissue viability in nonhuman primate studies and clinical studies. *Radiology*, 213:156-166.

Tornberg E, Andersson A, Göransson A, Von Seth G **(1993)** Water and fat distribution in pork in relation to sensory propreties. *Proc. Pork quality: Genetics and metabolic factores*, Eds. Poulanne E, Demeyer DJ, CAB International, pp:239.

Tornberg E **(1996)** Biophysical aspects of meat tenderness. *Meat Sci*, 43:175:191.

Tornberg E, Andersson K, Josell A **(1997)** The rheological properties of whole and minced meat during cooking as related to sensoty and structural characteristics. *In Proceedings 1st International Symposium on Food Rheology and Structure*, Zurich 16-20 March.

Tornberg E **(2005)** Effects of heat on meat proteins-Implications on structure and quality of meat products. *Meat Sci*, 70:493-508.

Twieg DB **(1983)** The k-trajectory formulation of the NMR imaging process with applications in analysis and synthesis of imaging methods. *Med Phys*, 10:610-621.

Van der Linden A, Verhoye M, Pörtner HO, Bock C **(2004)** The strengths of *in vivo* magnetic resonance imaging (MRI) to study environmental adaptational physiology in fish. *Magn Reson Mat Phys Bio Med*, 17:236-248.

Veliyulin E, Aursand IG **(2007)** ^{1}H and ^{23}Na MRI studies of atlantic salmon *(salmo salar)* and atlantic cod *(gadus morhua)* fillet pieces salted in different brine concentrations. *J Sci Food Agric*, 87:2676-2683.

Veliyulin E, Egelandsdal B, Marica F, Balcom BJ **(2009)** Quantitative ^{23}Na magnetic resonance imaging of model foods. *J Agric Food Chem*, 57:4091-4095.

Vestergaard C, Risum J, Adler-Nissen J **(2005)** ^{32}Na-MRI quantification of sodium and water mobility in pork during brine curing. *Meat Sci*, 69:663-672.

Wagner M, Quellec S, Trystram G, Lucas T **(2008a)** MRI evaluation of local expansion in bread crumb during baking. *J Cereal Sci*, 48:213-223.

Wagner M, Loubat M, Sommier A, Le Ray D, Collewet G, Broyart B, Quintard H, Davenel A, Trystram G, Lucas T **(2008b)** MRI study of bread baking: experimental device and MRI signal analysis. *Int J Food Sci Tech*, 43:1129-1139.

Wattanachant S, Benjakul S, Ledward DA **(2005)** Effect of heat treatment on changes in texture, structure and properties of Tai indigenous chicken muscle. *Food Chem*, 93:337-348.

Wehrli FW **(2007)** Structural and functional assessment of trabecluar and cortical bone by micro magnetic resonance imaging. *J Magn Reson Imaging* 25:390-409.

Wobber V, Hare B, Wrangham R **(2008)** Great apes prefer cooked food. *J Hum Evol*, 55:340-348.

Wright DJ, Leach IB, Wilding P **(1977)** Differential scanning calorimetric studies of muscle and its constitients. *J Sci Food Agric*, 28:557-564.

Yan ZY, McCarthy MJ, Klemann L, Otterburn MS, Finley J **(1996)** NMR application in complex food systems. *Magn Reson Imaging*, 14:979-981.

Ye X, Ruan R, Chen P, Doona C, Taub IA (2003) MRI temperature mapping and determination of liquid-particulate heat transfer coefficient in an Ohmically heated food system. Food Eng Phys Prop, 68:1341-1346.

Yushmanov VE, Yanovski B, Kharlamov A, LaVerde G, Boada FE, Jones SC **(2009)** Sodium mapping in focal cerebral ischemia in the rat by quantitative ^{23}Na MRI. *J Magn Reson Imaging*, 29:962-966.

Annexe : Résumés des communications dans des congrès

MRI assessment of deformation and water loss during meat heating

M. Bouhrara, J.L Damez, S. Clerjon, A. Benmoussa, S. Portanguen, C. Chevarin, A. Kondjoyan and J.M Bonny

Abstract — **The understanding and control of structural and physical changes in meat during cooking is essential for both meat industries and consumers. Magnetic resonance imaging (MRI) offers a non-invasive method for the local and dynamic characterisation of certain properties and structures of a sample. The aim of this work was to demonstrate the feasibility of using MRI *in situ* during the cooking of meat, and in particular imaging of the connective tissue to monitor deformation in the range 20-75 °C. The associated moisture loss was also estimated. Simulations of the temperature time course during cooking were carried out to relate deformation to sample temperature. The results showed that shrinkage began at 42 °C and accelerated from 54 °C. Migration of water from inside the fibres towards the interfascicular space appeared from 40°C and increased from 52 °C. These findings are consistent with those obtained by other, destructive and (or) non-localised methods. They will be used to determine deformation fields.**

UR370 Qualité des Produits Animaux, INRA, F-63122 Saint Genès Champanelle.
Phone: +33-4- 73-62-41-58. Fax: +33-4-73-62-40-89
E-mail: mustapha.bouhrara@clermont.inra.fr

Key words: MRI, heating, deformation, moisture loss.

INTRODUCTION

Knowledge of the structural changes that take place during treatment such as cooking is essential to enable meat industries to control the sensorial, nutritional and technical qualities of meat products. The cooking of meat causes a loss of approximately 20-40% of its mass, due to the expulsion of fluid (water and micronutrients) from the meat [1]. For the consumer, this moisture loss adversely affects quality, both sensorial (loss of tenderness and juiciness) and nutritional.

Several biophysical methods can be used to characterise the structure of meat [2]. During cooking, they can be used in particular to monitor the denaturing and precipitation of myosin [1, 3, 4, 5], the denaturing and shrinking of collagen [6] and the denaturing of other sarcoplasmic and myofibrillar proteins [7]. The mechanisms governing moisture loss have mainly been studied in raw meat [8, 9, 10], and less frequently in meat being heated [11, 12, 13].

The multi-exponential analysis of T_2 relaxation curves of water obtained by low-field nuclear magnetic resonance (NMR) showed a water loss in the main population [14]. Amplitude variations in the most mobile population were also observed, but were more difficult to interpret without information on the localisation of that population. The only imaging study [11] conducted during meat cooking found that this moisture loss was associated with a decrease in water mobility during cooking. The spatial information only demonstrated differences between the core and the exterior of the sample, without giving any insight into the deformation or the mobility of the different water compartments

Our aim was to use MRI to study the impact of temperature on the deformation of the connective tissue and the resulting water transfer. MRI is a non-invasive imaging method, and so is well-suited to continuous monitoring during heating. In addition, susceptibility-weighted MRI shows the connective tissue of the meat [15, 16] which can provide an array of internal markers. The acquisition of a series of images during heating, and their *a posteriori* analysis, allows deformation fields to be determined. Lastly, the statistical parametric mapping of ^{1}H nuclei allows water content and mobility to be locally quantified. This approach requires further methodological development (i) to acquire images at a fast enough rate to closely follow the changes in the meat during the heat treatment, and (ii) to ensure the feasibility of measurement in an evoluting system.

The aim of the work described here was to demonstrate the feasibility of MRI during cooking, in particular imaging of the connective tissue. The acquisition of several images during the heat process allowed the deformation of the connective tissue to be followed in the temperature range 20-75 °C. Simulations of the meat temperature time course during cooking related the sample temperature, the deformation of the connective tissue and the resulting water transfer.

MATERIALS AND METHODS

Sample

The muscle sample used was the elastin-rich biceps femoris (BF) of a Charolais heifer (age 4 years). Before use it was matured for 7 days, then vacuum-packed and stored at –20°C. It was thawed in air at 20°C and a cylinder of diameter 5 cm and length 6 cm long was cut from it with the muscle fibres parallel to the cylinder axis. This cylinder

was then again vacuum-packed to prevent direct contact with the circulating heating water.

Description of the heating device

The sample holder (4, Fig.1) was fitted inside a heat-insulating Teflon® tube (5, Fig.1). This was in turn placed at the centre of the radiofrequency transmitter/receiver coil (6, Fig.1) itself placed inside the imager (7, Fig.1).

The sample was heated in its holder by water flowing in a circuit (3, Fig.1) fed by a pump (13 l/min) (2, Fig.1). The water was heated in a holding tank (1, Fig.1) by a temperature-regulated electric heating element. Heating by a liquid is preferable to heating by a gas because the heat exchange is more even. Among the possible liquids (which include oils) water was chosen for its simplicity in use, in particular when cleaning and draining the circuit.

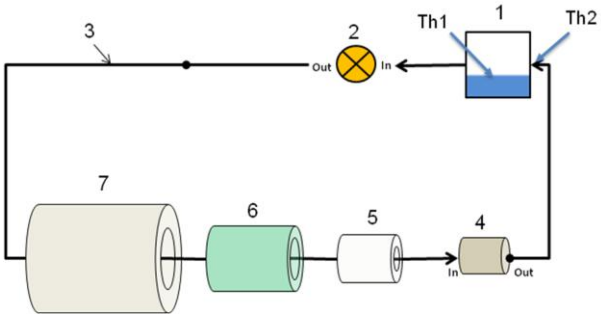

Fig.1. Diagram of set-up. (1) Holding tank and heating element for circulating water. (2) Pump. (3) 10 mm diameter silicone tubing. (4) Non-magnetic sample holder. (5) Non-magnetic Teflon® heat insulation. (6) ^{1}H NMR antenna. (7) High-field NMR imager.

The adiabaticity of the heating system was checked by placing two thermocouples (Th1 and Th2) at each end of the circuit (tank Th1 and return flow Th2). The temperature was the same at the two measurement points, with a constant temperature rise of 0.88 °C/min.

High-field MRI

Image acquisition was performed using a Biospec horizontal 4.7 tesla MRI system (Bruker Gmbh, Ettlingen, Germany), of diameter 26 cm, fitted with a BGA-26 rapid gradient system (maximum amplitude 50 mTm^{-1}, rise time 260 µs). The principal axis of the muscle fibres in the sample was parallel to the principal direction of the static magnetic field B_0.

The images were acquired continuously through a steady-state free precession sequence (SSFP or FLASH) that was weighted for magnetic susceptibility (T_E = 15 ms, T_R = 2000 ms). Using the difference in magnetic susceptibility between elastin and muscle fibres [15, 16], the images show the elastin-rich connective tissue (hyposignal). This sequence had bipolar gradients (delay between the two gradients Δ = 5.52 ms, duration of each gradient δ = 5.2 ms) which canceled out the signal from the mobile protons of the heating water. The removal of this signal eliminated the artefacts of movement, which degrade the image, and allows reducing the field of view (FOV), thereby increasing the temporal resolution for a given spatial resolution.

One acquisition consisted of a series of 18 contiguous radial sections. All the sections were obtained with a FOV of 64 × 64 mm², a matrix of 256 × 256 pixels and a thickness of 2 mm. The volume of the resulting voxel was 0.5 × 0.5 × 2 mm^3. The temporal resolution was 4 min 16 s. An acquisition was carried out at each temperature stage (every 10 °C) and during each temperature rise between successive stages.

Simulation of temperature

The temperature kinetics in the meat during cooking were calculated with a simple heat transfer model using the Comsol Multiphysics 3.4 software (COMSOL AB, Sweden 2007). Preliminary three-dimensional simulations showed that exchanges at the ends of the meat cylinder in contact with the polycarbonate support did not influence the temperature values in the central section of the cylinder.

Two-dimensional simulations by conduction were therefore carried out stepwise in this section; each step corresponded to a shrinkage of less than 5% of the surface bounded by the interface between the muscle and the exuded water from MRI images. Between two steps the simulated temperature field was projected onto the new contracted meat surface, the rest of the domain being occupied by the volume of water exuded.

The exchanges by water convection at the plastic bag surface were described by Newton's law, the heat transfer coefficient being calculated from the velocity of the circulating fluid and the Churchill-Bernstein relation [17]. The thermophysical properties of the products (plastic bag, meat, exsudate) were those used classically in the literature. Simplifying hypotheses were applied: (i) the volume of the plastic bag was assumed to be constant, and the volume of the exsudate formed during cooking was assumed to be equal to the decrease in volume of the contracted meat, and (ii) the heat transfer in the bag was assumed to be purely conductive. The temperature at the surface of the plastic bag was that measured experimentally in the circulating water.

RESULTS AND DISCUSSION

Feasibility of connective tissue imaging

The resonance frequency of the antenna/sample set and the impedance of the resonating cavity at this frequency changed with the temperature. These two drifts caused a signal loss of ~10% between 20 °C and 75 °C. The additional signal loss of

~40% observed between the two images obtained at 20 °C and 75 °C (Fig.2) was essentially due to the changes in the intrinsic NMR parameters of the muscle, in particular T_2 and the proton density, which decreased respectively by 25% and 30%.

The signal loss due to resonant cavity drift was minor compared with the losses due to changes in the sample. It was therefore not strictly necessary to adjust the antenna/sample settings manually. Also, the signal loss observed was tolerable as the final temperature (75 °C) displayed an acceptable signal-to-noise ratio (SNR ~ 21).

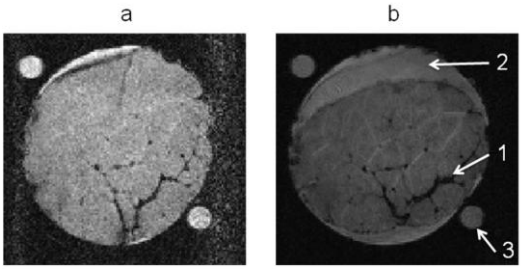

Fig.2. Susceptibility-weighted MRI images of a core section for the same grey scale (a) at 20 °C, (b) at 75 °C. 1: connective tissue, 2: fluid exsuded from muscle, 3: reference tube.

Monitoring of connective tissue deformations

Fig.3 shows deformation images obtained at the core of the sample as a function of the heating water temperature (Fig.3.a), and images of corresponding temperature gradients obtained by simulation (Fig.3.b). The plots (Fig.3.c) represent the time course of the surface of the core section of the muscle calculated from NMR images, the evolution of the temperature of heating water and the evolution of the mean temperature of the muscle obtained by simulation using shape information provided by NMR images.

Fig.3.a shows four representative images out of a series of 18 images recorded at different temperatures. The deformation time course plot (Fig.3.c) shows two inflection points, the first at 73 min, corresponding to the start of the sample deformation at the mean muscle temperature of 42 °C (heating water temperature 50 °C), and the second at 96 min, highlighting an acceleration of the deformation at a mean muscle temperature of 55 °C (heating water temperature 62 °C). Between 20 °C and 75 °C, the surface area of the muscle core section decreased by 22%.

The deformation images (Fig.3.a) reveal a network of exsuded water channels among the fibre bundles resulting from migration of intracellular water [10, 20]. This water was characterised by a higher T_2 value (more mobile water), which gave a hypersignal on the weighted image T_2*. This effect was seen from the mean muscle temperature of 40 °C (heating water temperature 47 °C). Like the connective tissue, these channels can serve as internal markers to determine deformation fields.

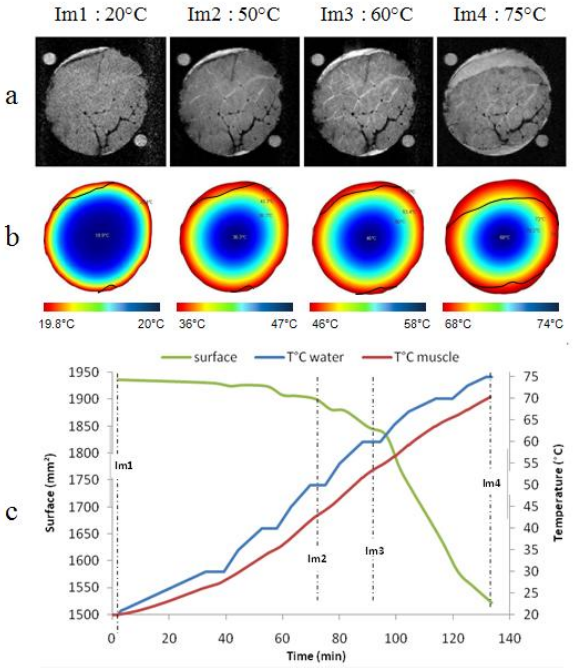

Fig.3. (a) NMR deformation images of a core section at different temperatures of the heating water, (b) images simulating corresponding temperature gradients, (c) time course plots of the surface area of the muscle core section, the temperature of the heating water and the mean muscle temperature.

The results of this study are consistent with those reported in the literature, in particular: (i) start of the deformation observed at 42 °C, corresponding to the beginning of myosin denaturation [1, 3, 4, 5] with a slow transverse contraction of the myofibres [18], and (ii) acceleration of deformation at 55 °C, corresponding to shrinkage and denaturation of collagen with expulsion of meat juice [1, 6, 7, 19].

The appearance of channels of migrating water among the fibre bundles (Fig.3.a) began from 40 °C. The initial denaturation of myosin causes a small loss of water from myofibres. This water migrates into the inter-myofibre space [10, 20]. The effect was more obvious from 52 °C, probably due to the contraction of the connective tissue, which expels water first into the interfascicular space and then out of the meat.

CONCLUSION

This work demonstrates the feasibility of connective tissue imaging during cooking using an MRI-compatible heating system with high adiabaticity. This imaging allowed, for the first time, the monitoring of meat deformation during cooking between 20 °C and 75 °C. Our observations are consistent with literature data for the temperatures of structural protein denaturation, collagen contraction and water loss.

Future work is planned to improve the temporal resolution of the method using rapid image encoding (e.g. echo planar imaging), determine deformation fields and quantify local water content.

ACKNOWLEDGEMENTS

This work was funded by the EU project ProSafeBeef (www.prosafebeef.eu/asp/).

REFERENCES

[1] Bertram, H. C., Engelsen, S. B., Busk, H., Karlsson, A. H., & Andersen, H. J. (2004). Water properties during cooking of pork studied by low field NMR relaxation: effects of curing and the RN-gene. Meat Science, 66, 437–446.

[2] Damez, J. L., & Clerjon, S. (2008). Meat quality assessment using biophysical methods related to meat structure. Meat Science 80, 132–149.

[3] Martens, H., & Vold, E. (1976). DSC studies of muscle protein denaturation. In Proceedings of the 22nd European meeting of meat research workers, Malmo, Sweden (p. J 9.3).

[4] Micklinder, E., Peshlov, B., Purslow, P. P., & Engelsen, S. B. (2002). NMR-cooking monitoring the changes in meat during cooking by low-field H-NMR. Trends in Food Science & Technology, 13, 341-346.

[5] Martens, H., Stabursvik, E., & Martens, M. (1978). Texture and colour changes in meat during cooking related to thermal denaturation of muscle proteins. Journal of Texture Studies, 13, 291-309.

[6] Stabursvik, E., & Martens, H. (1980). Thermal denaturation of proteins in post rigor muscle tissue as studied by differential scanning calorimetry. Journal of Science Food and Agriculture, 31, 1034–1042.

[7] Wright, D. J., Leach, I. B., & Wilding, P. (1977). Differential scanning calorimetric studies of muscle and its constituents. Journal of Science Food and Agriculture, 28, 557.

[8] Bertram, H. C., Dønstrup, S., Karlsson, A. H., & Andersen, H. J. (2002). Continuous distribution analysis of T2 relaxation in meat: an approach in the determination of water-holding capacity. Meat Science, 60, 279–285.

[9] Renou, J. P., Foucat, L., & Bonny, J. M. (2003). Magnetic resonance imaging studies of water interactions in meat. Food Chemistry, 82, 35-39.

[10] Bertram, H. C., Whittaker, A. K., Andersen, A. J., & Karlsson, A. H. (2004). Visualization of drip channels in meat using NMR microimaging. Meat Science, 68, 667–670.

[11] Shaarani, S. Md., Nott, K. P., & Hall, L. D. (2006). Combination of NMR and MRI quantitation of moisture and structure changes for convection cooking of fresh chicken meat. Meat Science, 72, 398–403.

[12] Wählby, U., Skjöldebrand, C. (2001). NIR-measurements of moisture changes in foods. Journal of Food Engineering, 47, 303-312.

[13] Van der Sman, R.G.M. (2007). Moisture transport during cooking of meat: An analysis based on Flory–Rehner theory. Meat Science, 76, 730–738.

[14] Tornberg, E. (2005). Effects of heat on meat proteins: Implications on structure and quality of meat products. Meat Science, 70, 493-508.

[15] Bonny, J. M., Laurent, W., Labas, R.., Taylor, R.., Berge, P., & Renou, J. P. (2001). Magnetic resonance imaging of connective tissue: a non-destructive method for characterizing muscle structure. Journal of the Science of Food and Agriculture, 81, 337-341.

[16] Bonny, J. M. (2007). Magnetic resonance imaging of meat: Towards the non-destructive determination of extracellular matrix composition and distribution. GIT laboratory Journal, 11, 30-31.

[17] Churchill, S.W., & Bernstein, M. (1977). A Correlating Equation for Forced Convection from Gases and Liquids to a Circular Cylinder in Cross Flow. J. Heat Transfer, 99, 300-306.

[18] Bendall, J. R., & Restall, D. J. (1983). The cooking of single myofibres, small myofibre bundles and muscle strips from beef *M. Psoas* and *M. Sternomandibularis* muscles at varying heating rates and temperatures. Meat Science, 8, 93-117.

[19] Palka, K., & Daun, H. (1999). Changes in texture, cooking losses, and myofibrillar structure of bovine M-semitendinosus during heating. Meat Science, 51, 237-243.

[20] Bonny, J.M., & Renou, J.P. (2002). Water diffusion features as indicators of muscle structure ex vivo. Magnetic Resonance Imaging 20, 395-400.

Water expellation during meat heating assessed by MRI

M. Bouhrara, J.L Damez, S. Clerjon, C. Chevarin, A. Benmoussa, and J.M Bonny

UR370 QuaPA, INRA, F-63122 Saint-Genès-Champanelle, France

The heat treatment of meat upon cooking causes myowater expellation that contains water and micronutrients. A better understanding of how this process occurs is then required to control sensorial, nutritional and technical qualities. Heating induces several microstructural changes and in particular muscle shrinkage due to the contraction of collagen fibres stored in the connective tissue (CT). Until now, techniques used to outline these phenomena were mainly invasive and non-localized. Magnetic resonance imaging (MRI) being a non destructive technique highlighting contrast between CT and muscle fibres is able to follow *in situ* the deformation of CT framework during meat heating. Moreover, mapping water content by MRI allows studying the coupling between shrinkage and water migration.

Here, MRI acquisition of a beef muscle sample was performed *in situ* at high field (4.7 T) using a home-made MRI-compatible heating system. The sample was three-dimensionally scanned at 18 increasing temperature steps in the range 20-75°C. An original MRI method of acquisition was developed to remove artefacts due to circulating heating water and to highlight CT, and more recently to increase the temporal resolution (4 min 16 s) without losing spatial resolution (0.5 x 0.5 x 2 mm^3). Besides, temperature distribution inside the meat sample was simulated using COMSOL Multiphysics software.

Our first results using the slowest MRI technique show a network of channels between the fibre bundles filled by migrating intracellular water which appears from 40° C. It is explained by the initial denaturation of structural proteins (myosin) inducing the release of water from cells (myofibres) into the extracellular space. The water expellation is more obvious from 52° C, probably due to the contraction of CT beginning around 42°C, which expels water first into the inter bundle space and then out of the meat. Our non-invasive results are consistent with literature data for the key temperatures of structural protein denaturation and collagen contraction, showing *in situ* and for the first time the water expellation process during meat heating.

Suivi par IRM de l'expulsion de l'eau du muscle pendant le chauffage

M. Bouhrara, J.L Damez, S. Clerjon, C. Chevarin, A. Benmoussa, and J.M Bonny.

UR370 QuaPA, INRA, F-63122 Saint-Genès-Champanelle, France

Introduction

Le traitement thermique du muscle lors de la cuisson cause l'expulsion de jus composé d'eau et de micronutriments. Une meilleure connaissance de ce processus est nécessaire afin de maitriser les qualités sensorielles, nutritionnelles et technologiques de la viande. Le chauffage induit plusieurs changements structuraux et en particulier le rétrécissement du muscle dû aux contractions des fibres de collagène contenues dans le tissu conjonctif (TC). Jusqu'à présent, les techniques utilisées pour décrire ces phénomènes sont essentiellement invasives, destructives et/ou non localisées. L'imagerie par résonance magnétique (IRM) est une technique non destructive et non invasive, permettant de mettre en évidence le contraste entre le TC et les fibres musculaires [1]. Elle est capable de suivre *in situ* les déformations du réseau conjonctif au cours de procédés thermiques. De plus, la cartographie par IRM de la teneur en eau permet d'étudier les liens entre les déformations et la migration de l'eau.

Ici, l'acquisition des images RMN d'un échantillon de muscle de bœuf est réalisée *in situ* à haut champ (4,7 T) en utilisant un système de chauffage amagnétique développé au laboratoire. Dans la gamme 20-75 °C, une vingtaine d'images tridimensionnelles de l'échantillon sont acquises pendant la montée en température. Une méthode d'acquisition originale a été développée permettant d'éliminer les artefacts dus à la circulation de l'eau chauffante, mettre en évidence le TC, et augmenter la résolution temporelle (4min16s) sans perdre la résolution spatiale (0,25 x 0,25 x 2 mm^3). Par ailleurs, la distribution de la température à l'intérieur de l'échantillon est simulée avec le logiciel *COMSOL Multiphysics*. Cette simulation a été validée à partir de mesures effectuées dans l'échantillon à l'aide de 12 thermocouples.

Résultats

Les résultats de cette étude par IRM montrent que le début de la déformation est observé à 42°C, ceci correspond au commencement de la contraction du TC et de la dénaturation de la myosine [2] ; l'accélération de la déformation à 54°C correspond à la contraction et à la dénaturation du collagène avec expulsion du jus de la viande [2,3]. L'apparition de canaux

d’eau migrée entre les faisceaux de fibres commence à partir de 40 °C, la dénaturation initiale de la myosine entrainant une petite perte d’eau des myofibres. Cette eau migre pour s’installer dans l’espace inter-myofibres [4]. Cette accumulation apparait plus nettement à partir de 52°C, probablement due à la contraction du conjonctif qui entraine une expulsion d’eau d’abord vers l’espace inter fasciculaire puis vers l’extérieur de la viande.

Conclusion

Cette étude a permis de montrer la faisabilité de l’imagerie du TC au cours de la cuisson, grâce à un système de chauffage compatible IRM. Les résultats obtenus avec cette méthode non invasive et non destructive sont en cohérence avec les données de la littérature pour les températures principales de la dénaturation des protéines de structure et de la contraction du collagène, montrant *in situ* et pour la première fois le processus d'expellation de l'eau de la viande ainsi que ses déformation pendant le chauffage de 20 à 75 °C.

Ce travail bénéficie d’un financement Européen du 6ème PCRD ProSafeBeef et d’une bourse MENRT.

[1] J. M., Bonny et al., *Journal of the Science of Food and Agriculture* 2001, **Vol. 81**, 337-341.
[2] H. C., Bertram et al., *Meat Science* 2004, **Vol. 66**, 437-446.
[3] K., Palka et al., *Meat Science* 1999, **Vol. 51**, 237-243.
[4] H. C., Bertram et al., *Meat Science* 2004, **Vol. 68**, 667-670.

In situ MR imaging of food during continuous heating

Mustapha BOUHRARA, Sylvie CLERJON, Jean-Louis DAMEZ, Abdlatif BENMOUSSA, Cyril CHEVARIN and Jean-Marie BONNY

UR370 QuaPA, INRA, F-63122 Saint-Genès-Champanelle, France

MR imaging can overcome the limitations of destructive methods for the *in situ* monitoring of structural changes and mass transfer in foods during heat treatment. For this application, a nonmagnetic adiabatic heating system is necessary. Moreover, a continuous control over the measuring conditions is needed to prevent the signal-to-noise ratio (SNR) worsening with rising temperature. A nonmagnetic experimental device was designed based on circulating water heated linearly from 20 to 75 °C. The tank containing the meat sample and the circulating water was heat-insulated from the transmitter-receiver antenna by a PTFE® tube. During the experiment the SNR loss of ~40% due to concomitant variations in the intrinsic NMR parameters of the muscle outweighed the ~15% loss caused by the extrinsic experimental variations. To obtain sufficient contrast in the muscle and monitor its deformation at 4.7 T, the imaging sequence made use of the difference in magnetic susceptibility between the network of conjunctive tissue and the muscle fibres. This sequence featured bipolar gradients to cancel the signal from the mobile protons in the circulating hot water. Velocity mapping by MRI showed that the distribution of mean velocities in the heating water was uneven in the tank, which explains the persistence of minor artifacts in the low velocity areas. In addition, numerical temperature simulations showed that the heat exchange varied little at the surfaces of the sample over the range of velocities measured. These conditions therefore ensured homogeneous and reproducible heating of samples. An acceleration strategy based on the BRISK method (1) was developed to achieve a time resolution of 1’45’’, a mean SNR of ~40 and a voxel size of $0.25 \times 0.25 \times 2$ mm^3. In these conditions, structural changes and juice transfer in slowly cooking meat samples can be monitored in an original and robust way.

1. Doyle M., Walsh E.G., Blackwell G.G., Pohost G.M., Magn Reson Med, *BRISK: A Rapid Cardiac Imaging Technique*, 33, 163-170 (1995)

Development of dynamic MRI at high field for *in situ* analysis of muscle during heating

M. Bouhrara, S. Clerjon, J.L. Damez, C. Chevarin, A. Benmoussa, and J.M. Bonny

UR370 QuaPA, INRA, F-63122 Saint-Genès-Champanelle, France

An original experimental system was developed for *in situ* monitoring of the deformation of connective tissue and induced water losses during the heating of meats. The heating was carried out by circulating water flowing around the sample in a non-magnetic, adiabatic device designed by us.

A MRI sequence was developed to make use of the susceptibility difference between connective tissue and muscle fibres. Bipolar gradients were added in this sequence to cancel the signal from the circulating/mobile protons of the heating water.

During experimentation, an SNR loss of ~40% due to concomitant variations of intrinsic NMR parameters outweighed the loss of ~15% caused by extrinsic experimental variations (thermal noise, frequency and impedance detuning of the RF coil). A speeding-up strategy based on partial filling of *k*-space was developed to achieve a time resolution of 1'45" and an average SNR of ~40 for a voxel volume of $0.25 \times 0.25 \times 2$ mm^3. Also, the temperature inside the sample was mapped by simulation using COMSOL software. This process was validated using invasive measurements by several temperature sensors.

Susceptibility-weighted MRI coupled with temperature mapping showed that deformation starts at 42 °C. It corresponds to the beginning of myosin denaturation and a transversal, slow contraction of myofibres. The acceleration of deformation at 54 °C is due to contraction and denaturation of collagen with expulsion of meat juice. Water channels appear in between the fascicles of muscle fibres from 40 °C and clearly accumulate from 52 °C. The next step in this work will be to quantify deformation fields and water content locally and so model the relationship between structural changes, mass transfer and temperature.

A fast and accurate method for active B_1 field mapping

M. Bouhrara and J.M. Bonny

UR370 QuaPA, INRA, F-63122 Saint-Genès-Champanelle, France

Spatial inhomogeneity of the active B_1 field (B_1^+) biases MRI-quantified nuclei density. B_1^+ in the studied sample therefore has to be estimated as a prerequisite to accurate density mapping. The reference technique for estimating B_1^+ is the double angle method (DAM)[1], based on the acquisition of two images obtained with different prescribed tip angles (α and $k\alpha$, respectively), all other signal-affecting parameters kept constant. However, changing the second prescribed tip angle by the k factor modifies the profile of the selective pulse(s), which is a major source of bias[2], especially when large angles are prescribed.

Using phantoms at 4.7 T and for large range of B_1^+ values, we analyzed discrepancies between experimental signals and the theoretical signals derived from an analytical model integrating different pulse shapes. We found that Gaussian pulse led to significant deviations between experimental and analytical values, especially for larger B_1^+ values. Deviations were more pronounced for spin-echo sequences as the excitation and refocusing steps cumulated errors. Interestingly, a good correspondence was observed by replacing Gaussian (and other popular linear-phase pulses) with SLR pulses[3]. We also checked that our model fitted well when segmented echo-planar encoding was introduced in order to speed up the temporal resolution of the DAM. Lastly, we demonstrated that the sensitivity of DAM to B_1^+ variations increased with parameter k, while measurement dynamics decreased. Furthermore, computing the level of noise propagating from the two images to the B_1^+ map revealed an optimal choice for the prescribed tip angle α for any k value, with $k = 2$ corresponding to the global *optimum*.

1. Insko E.K. and Bolinger L., *Journal of Magnetic Resonance A* 103, 82–85 (1993)
2. Wang J., Mao W., Qui M., Smith M.B. and Constable R.T., *Magnetic Resonance in Medicine* 56, 463–468 (2006)
3. Pauly J., Le Roux P., Nishimura D. and Macovski A., *IEEE Transactions on Medical Imaging* 10, 53–65 (1991)